



HAL
open science

A 6 Ma record of palaeodenudation in the central Himalayas from in situ cosmogenic ^{10}Be in the Surai section

Julien Charreau, Jerome Lave, Christian France-Lanord, Nicolas Puchol, P.H. Blard, Raphaël Pik, Ananta Prasad Gajurel, Maurice Arnold, Georges Aumaitre, D.L. Bourles, et al.

► **To cite this version:**

Julien Charreau, Jerome Lave, Christian France-Lanord, Nicolas Puchol, P.H. Blard, et al.. A 6 Ma record of palaeodenudation in the central Himalayas from in situ cosmogenic ^{10}Be in the Surai section. Basin Research, 2021, 33 (2), pp.1218-1239. 10.1111/bre.12511 . hal-03047117

HAL Id: hal-03047117

<https://hal.science/hal-03047117v1>

Submitted on 16 Dec 2020

HAL is a multi-disciplinary open access archive for the deposit and dissemination of scientific research documents, whether they are published or not. The documents may come from teaching and research institutions in France or abroad, or from public or private research centers.

L'archive ouverte pluridisciplinaire **HAL**, est destinée au dépôt et à la diffusion de documents scientifiques de niveau recherche, publiés ou non, émanant des établissements d'enseignement et de recherche français ou étrangers, des laboratoires publics ou privés.



**A 6 Ma record of palaeodenudation in the central Himalayas
from in situ cosmogenic ^{10}Be in the Surai section**

Journal:	<i>Basin Research</i>
Manuscript ID	BRE-032-2020.R1
Manuscript Type:	Original Article
Date Submitted by the Author:	n/a
Complete List of Authors:	Charreau, Julien; Université de Lorraine-CNRS, CRPG UMR 7358 Lavé, Jérôme; Université de Lorraine-CNRS, CRPG UMR 7358 France-Lanord, Christian; Université de Lorraine-CNRS, CRPG UMR 7358 Puchol, Nicolas; Université de Lorraine-CNRS, CRPG UMR 7358 Blard, Pierre-Henri; Université de Lorraine-CNRS, CRPG UMR 7358 Pik, Raphael; Université de Lorraine-CNRS, CRPG UMR 7358 Gajurel, Ananta Prasad ; Tribhuvan University, Department of Geology ASTER Team, ASTER Team; Aix-Marseille Université, CEREGE-CNRS-IRD- Collège de France-INRAE
Keywords:	sediment flux, tectonic geomorphology, foreland basins

SCHOLARONE™
Manuscripts

A 6 Ma record of palaeodenudation in the central Himalayas from in situ cosmogenic ^{10}Be in the Surai section

Julien Charreau^{1*}, Jérôme Lavé¹, Christian France-Lanord¹, Nicolas Puchol¹, Pierre-Henri Blard¹, Raphaël Pik¹, Ananta Prasad Gajurel² and ASTER Team^{3,+}

1. CRPG, UMR7358, Université de Lorraine - CNRS, 15 rue Notre-Dame des pauvres, 54500 Vandoeuvre-lès-Nancy, France
 2. Department of Geology, Tribhuvan University, Kathmandu, Nepal
 3. Aix-Marseille Université, CNRS-IRD-Collège de France-INRAE, UM 34 CEREGE, Technopôle de l'Environnement Arbois-Méditerranée, BP80, 13545 Aix-en-Provence, France
- + Maurice Arnold, Georges Aumaître, Didier L Boulès, Karim Keddadouche.

*corresponding author: julien.charreau@univ-lorraine.fr

Key word: Himalaya, cosmogenic ^{10}Be , palaeodenudation rates, late Neogene

Abstract

To better constrain late Neogene denudation of the Himalayas, we analysed in situ ^{10}Be concentrations in 17 Neogene sediment **samples** of the Surai section (central Nepal) and two modern sediment **samples** of the Rapti River. We first refined the depositional ages of the Surai section from 36 new paleomagnetic analyses, five $^{26}\text{Al}/^{10}\text{Be}$ burial ages, **and, based on the Dynamic Time Warping algorithm, 10^4 automatically calculated likely magnetostratigraphic correlations.** We also traced changing sediment sources using major element and Sr-Nd isotopic data, finding at 4-3 Ma a switch from a large, trans-Himalayan river to a river draining **only the Lesser Himalaya and** Siwalik piedmont, increasing the contribution of recycled sediments at that time. ^{10}Be concentrations in Neogene sediments range from (1.00 ± 0.36) to $(5.22 \pm 0.98) \times 10^3$ at g^{-1} and decrease with stratigraphic age. Based on a flood plain transport model, our refined age model, and assuming a drainage change at 4-3 Ma, we reconstructed ^{10}Be concentrations at the time of deposition. Assuming cosmogenic production rates similar to those of the modern basins, we calculated palaeodenudation rates of 0.9 ± 0.5 to 3.9 ± 2.7 mm a^{-1} from ~ 6 to ~ 3 Ma in the palaeo-Karnali basin and 0.6 ± 0.2 to 1.6 ± 0.8 mm a^{-1} since ~ 3 Ma in the palaeo-Rapti basin. Given the uncertainties and similar modern values of ~ 2 mm a^{-1} , the palaeo-Karnali denudation rates may have been steady at $\sim 1.7 \pm 0.3$ mm a^{-1} for the last ~ 6 Ma. **A transient acceleration of the denudation in the palaeo-Rapti basin of ~ 1.5 mm a^{-1} since ~ 1.5 Ma was likely due to the reworking of older, ^{10}Be -depleted Siwalik sediments in the foreland. If true, this steadiness** of the denudation rates may suggest that Quaternary glaciations did not largely affect Himalayan denudation.

39 1. Introduction

40 The denudation history of the Himalayas, the largest and highest mountain range in the world, remains
41 controversial, precluding a strong understanding of how this large mountain range grew. Sediment budget from
42 basins surrounding the Himalayas are difficult to reconstruct because the depositional areas are very large,
43 including the Ganga basin and the Indus and Bengal fans. Moreover, it is not straightforward to accurately assess
44 both the complex geometry and chronology of sediment infilling in these locations. Consequently, published
45 Cenozoic Himalayan sedimentary budgets have yielded inconsistent constrains (e.g. Burbank et al., 1993; Clift,
46 2006; Métivier et al., 1999). For example, according to Métivier et al. (1999) the average accumulation rates curve
47 for Asian sedimentary basins increased quickly in an exponential manner from $0.5 \times 10^6 \text{ km}^3 \text{ Ma}^{-1}$ in the Oligocene
48 to their maximum values $>1.5 \times 10^6 \text{ km}^3 \text{ Ma}^{-1}$ in the Quaternary. Clift (2006) reported an increase in sedimentation
49 rate from <20 to $\sim 100\text{--}120 \times 10^3 \text{ km}^3 \text{ Ma}^{-1}$ from 50 to ~ 15 Ma, then a drop between ~ 15 and ~ 10 Ma followed by a
50 new acceleration until the Quaternary where sedimentation rates reached precedent early Miocene values.

51 Similarly, thermochronological studies have brought contrasted constraints on the late Cenozoic evolution
52 of Himalayan denudation. The interpretation of the in situ bedrock thermochronological ages (Herman et al., 2013;
53 Huntington et al., 2006) suggest that the denudation rates along the Himalayan arc increased by a factor of 1 to 4
54 during the Quaternary, which some ascribe to an increased climatic, not tectonic, forcing. However, the denudation
55 history is spatially variable across the range, and some regions, e.g., Bhutan, are characterized by lower denudation
56 rates during the last 6–8 Ma (Adams et al., 2015; Thiede and Ehlers, 2013). Similarly, thermochronological
57 analyses of detrital grains in molasse sediments deposited at the Himalayan front suggest either quite stable basin-
58 averaged denudation rates since the mid-Miocene in central Nepal (Bernet et al., 2006; Harrison et al., 1993; Szulc
59 et al., 2006; van der Beek et al., 2006) or a rapid acceleration of the denudation around 5 Ma in the eastern
60 Himalayan syntaxis (Lang et al., 2016). Notably, however, this thermochronological technique averages
61 denudation rates over timescales of a few million years, possibly smoothing and offsetting rapid changes related,
62 for example, to climate.

63 An alternative method to reconstruct denudation histories of a mountain range is to reconstruct basin
64 average paleodenudation rates from the measurement of in situ cosmogenic nuclides (e.g., ^{10}Be) in ancient (>1
65 Ma) river sediments (Charreau et al., 2011; Puchol et al., 2017). Cosmogenic nuclide concentrations in river sands
66 average the concentrations in all surficial rocks outcropping in the drainage basin (e.g. Brown et al., 1995). When
67 measured in ancient sediments, cosmogenic nuclides average the palaeodenudation rates of the drainage basin at
68 the time of deposition (Charreau et al., 2011; Puchol et al., 2017; Refsnider, 2010; Schaller et al., 2002). This
69 approach is advantageous as it averages denudation rates over short characteristic timescales, typically <5 ka for
70 denudation rates larger than 0.1 mm a^{-1} .

71 Here, to reconstruct past Himalayan denudation rates, we analysed in situ ^{10}Be concentrations in Neogene
72 sediments sampled from the Surai section (Fig. 1), a well-documented stratigraphic section in the piedmont
73 covering the last 6 Ma. The section has been dated by magnetostratigraphy (Appel et al., 1991; Ojha et al., 2009;
74 Rosler et al., 1997) and biostratigraphy (Corvinus and Rimal, 2001). Moreover, during recent decades, it has been
75 extensively studied through geochemical (Huyghe et al., 2001; Szulc et al., 2006), mineralogical (Szulc et al.,
76 2006), and thermochronological studies (Bernet et al., 2006; Szulc et al., 2006; van der Beek et al., 2006). These
77 data are key to tracing changes in sediment provenance, which are needed to estimate the cosmogenic production
78 rates during the past and hence to reconstructing palaeodenudation rates from measured ^{10}Be concentrations.

79

80 2. Geological Setting

81 2.1 Geology of the Himalayas

82 The geology of the Himalayan arc in Nepal is traditionally divided into five main units from north to
83 south: the **Thetyan** Sedimentary Series (TSS), the Higher Himalaya Crystalline **unit** (HHC), the Lesser Himalaya
84 **unit** (LH), the Siwalik folded molasse, and the foreland basin of the Ganga plain (Fig. 1). These units are separated
85 by four major faults (Gansser, 1964): from north to south, the Southern Tibetan Detachment (STD), the Main
86 Central Thrust (MCT), the Main Boundary Thrust (MBT), and the Main Frontal Thrust (MFT). Along the Southern
87 Tibetan plateau, the TSS comprises Mesozoic and Palaeozoic marine sediments and medium- to low-grade
88 metamorphic rocks. The HHC comprises high-grade crystalline metamorphic units. Both formations are intruded
89 by Miocene leucogranites and form the highest relief of the Nepalese Himalaya. To the south, the HHC units
90 overthrust the LH at the MCT level and occur as two major klippen in western Nepal. The LH series comprises
91 low-grade Precambrian detrital continental meta-sediments and Cretaceous to Eocene marine sediments; it
92 represents an intermediate midland relief between the higher relief of the HHC to the north and the Siwalik Hills
93 to the south, the first significant relief at the foot of the Himalayas (Figs. 1 and 2a).

94

95 2.2 The Siwalik Hills

96 The Siwalik Hills, bounded to the north by the MBT and to the south by the MFT (Figs. 1, **2a** and 2b),
97 comprise successive fold and thrust belts oriented WNW-ESE along the Himalayas (Auden, 1935). The Siwalik
98 Hills do not exceed 1,000 m elevation and comprise a thick (>5 km) pile of Neogene molasse produced by several
99 million years of intense denudation in the Himalayas (DeCelles et al., 1998; Hérail and Mascle, 1980).

100 **How the sediments are currently deposited in the modern Ganga plain** provides useful information to
101 understand the palaeoenvironmental setting in which the Siwalik sediments formed (e.g. Sinha et al., 2005). At
102 the very front of the Himalayas, in the Ganga plain, sediments are deposited on a series of large alluvial megafans
103 (10^4 – 10^5 km²) associated with trans-Himalayan rivers that drain **the Himalayas from the lowland piedmont to the**
104 **high elevated regions (Fig. 1)** (DeCelles et al., 1998; Gupta, 1997). These megafans alternate with smaller interfans
105 associated with smaller rivers originating in the **Lesser Himalaya** (Fig. 1) (DeCelles et al., 1998; Gupta, 1997;
106 Wells and Dorr, 1977). Although the facies and origins of the Siwalik sediments vary considerably along the strike
107 of the >2,000-km-long range, these molasse, mainly of continental origin, are usually stratigraphically divided into
108 three litho-stratigraphic units (DeCelles et al., 1998; Dhital et al., 1995) **namely** the Lower, the Middle and the
109 Upper Siwaliks and showing an upward coarsening related to the progressive southward migration of the
110 Himalayan thrust wedge and depositional facies (Dubille and Lavé, 2015; Lyon-Caen and Molnar, 1985).

111

112 2.3 The Surai section

113 The Surai section is in the southern part of western-central Nepal, ~5 km to the southeast of the town
114 Bhalubang (Figs. 2a, b). In this area, Siwalik sediments are folded into a ~750-m-high, >100-km-long ridge
115 developed on the hanging wall of the MFT, the so-called Dundwa ridge, which is progressively propagating to the
116 west. A piggy-back basin has developed to the north of the Dundwa ridge, in which the West Rapti River (not to
117 be confused with the East Rapti River, a tributary of the Narayani River) deviates to the West (Figs. 1 and 2). The
118 Surai Khola, which drains the most southern segment of the Siwaliks into the Ganga plain (Fig. 2b), has deeply

119 incised the uplifting Dundwa ridge. Construction of the 19-km-long RH01 road between Chanauta and Bhalubang
120 between 1983 and 1986 exposed a nearly continuous >5,000-m-thick section of outcrops of Siwalik sediments
121 dipping to the north at 60–70° (Fig. 2d). This section, the ‘Surai section’, has enabled dense palaeomagnetic
122 sampling for magnetostratigraphic analyses, which have roughly constrained the depositional ages of the Lower
123 and Middle Siwaliks groups to ~14–10 Ma and 10–4 Ma, respectively (Appel et al., 1991; Corvinus and Rimal,
124 2001; Ojha et al., 2009; Rosler et al., 1997; Rosler and Appel, 1998). However, some ambiguities and uncertainties
125 persist for the upper, coarser part of the section that is less amenable to palaeomagnetic sampling. The depositional
126 ages of the top of the section are hence more loosely constrained between 4 and 1.5 Ma.

127 Building on this chronology, the Surai section has been intensively examined by palaeontological
128 (Corvinus and Rimal, 2001), sedimentological (DeCelles et al., 1998; Dhital et al., 1995; Nakayama and Ulak,
129 1999), sediment provenance (DeCelles et al., 1998; Szulc et al., 2006), geochemical (Huyghe et al., 2001; Lupker
130 et al., 2012b; Szulc et al., 2006), and thermochronological studies (Bernet et al., 2006; Szulc et al., 2006; van der
131 Beek et al., 2006). The section consists mainly of **fluvial** sediments that gradually coarsen upward, and includes
132 the Upper, Middle, and Lower Siwaliks groups (Fig. 2), which have been subdivided from bottom to top into the
133 Bankas, Chor Khola, Surai Khola, Dobatta, and Dan Khola local formations (Corvinus and Rimal, 2001; Dhital et
134 al., 1995; Nakayama and Ulak, 1999). Sedimentological facies associations reveal that the depositional
135 environmental changed from a small meandering river channel to a larger braided river channel around 10–6 Ma
136 (DeCelles et al., 1998; Nakayama and Ulak, 1999). Upsection, the river remained braided, but evolved from a
137 sand- to a gravel-dominated system in the middle of the Dhan Khola formation (Fig. 4) (Nakayama and Ulak,
138 1999). Most palaeocurrents measured along the section suggest **that the river flowed** toward the south (DeCelles
139 et al., 1998; Szulc et al., 2006), led DeCelles et al. (1998) to conclude that the sediment source was persistently to
140 the north; they excluded the possibility of syntectonic sedimentation by local rivers draining the uplifting Dundwa
141 ridge itself. However, palaeocurrent directions in the Upper Siwaliks group exhibit more scatter than down section
142 (DeCelles et al., 1998), suggesting the possible contribution of local tributaries. **Based on provenance data,**
143 DeCelles et al. (1998) further suggested that the river that deposited the upper and middle Surai section was similar
144 to present trans-Himalayan rivers. It is, however, difficult from the sedimentological record alone to discriminate
145 between a large river draining the internal part of the range and smaller interfan rivers draining only the **Lesser**
146 **Himalaya**.

147 The mineralogical, isotopic, and/or geochemical compositions of the sediments in the Surai section reveal
148 further details of their source rocks. Several tracers suggest that the exhumation of the LH began ~12 Ma and has
149 remained a significant source of sediment in the area (DeCelles et al., 1998; Huyghe et al., 2001; Szulc et al.,
150 2006). High-grade metamorphic minerals present in the section suggest that the palaeo-Rapti River has likely also
151 continuously eroded HHC rocks (Szulc et al., 2006), although the exact source remains ambiguous due to the
152 presence of the HHC klippe thrust over the midland and LH (Fig. 2). Therefore, these petrologic data only constrain
153 that the palaeo-drainage basin has always reached, at least, the HHC klippe (Fig. 2). Importantly, it remains
154 uncertain whether the river drained the entire Himalayas or only the **Lesser Himalaya**.

155

156 **3. Methods and sampling**

157 *3.1 General approach*

158 To document palaeodenudation rates in the Surai section, we measured the bulk ^{10}Be concentrations (at
 159 g^{-1} , see section 3.2) of Siwalik sediments exposed along the Surai section (N_{total}). The basin-averaged denudation
 160 rate $\bar{\epsilon}$ is calculated from N_{total} by solving the equation (e.g. Charreau et al., 2011; Puchol et al., 2017):

$$161 \quad N_{\text{total}} = e^{-\lambda t} \left[\sum_{j=1,3} \frac{\bar{P}_j}{3\bar{\epsilon}\rho_r A_j} + N_{\text{fp}} \right] + N_{\text{recent}}(1)$$

162 where \bar{P}_j is the overall palaeoproduction rate of ^{10}Be averaged over the drainage basin at the time of erosion, which
 163 accounts for all cosmogenic production mechanisms (spallation, ‘n’, and slow and fast muons, ‘ μs ’ and ‘ μf ’,
 164 respectively, indicated by $j = 1-3$), ρ_r is the density of the denuded rocks (taken as 2.7 g cm^{-3}), λ the radioactive
 165 decay constant, A_j the characteristic attenuation lengths of the cosmogenic production mechanisms ($A_n = 160 \text{ g}$
 166 cm^{-2} , $A_{\mu\text{s}} = 1,500 \text{ g cm}^{-2}$, and $A_{\mu\text{f}} = 4,320 \text{ g cm}^{-2}$) (Braucher et al., 2011), and t the time at which the sediments
 167 were buried (i.e., the depositional age). N_{fp} and N_{recent} are the number of ^{10}Be atoms (per g of quartz) accumulated
 168 by the sediments during their transport and final deposition in the Ganga plain (i.e., until buried deep enough to
 169 be fully shielded from cosmic rays) and during their most recent exposure in outcrop, respectively.

170 Several corrections and assumptions are required (Charreau et al., 2011; Puchol et al., 2017) to derive
 171 palaeodenudation rates from the measured ^{10}Be concentrations along the Surai section. First, we assumed N_{recent}
 172 to be negligible because of the recent road cut (Fig. 2) and the high erosion rates expected in the Siwalik hills
 173 (Hurtrez et al., 1999; Lavé and Avouac, 2000). Then, solving equation (1) requires precise knowledge of the
 174 depositional ages t , especially to correct the measured concentrations for radioactive decay. To this aim, we refined
 175 the depositional ages of the Surai section, especially in the upper part of the section, using new palaeomagnetic
 176 analyses, stochastic magnetostratigraphic correlations (Lallier et al., 2013), and $^{26}\text{Al}/^{10}\text{Be}$ cosmogenic burial dating
 177 (e.g., Granger and Muzikar, 2001; see section 3.3). We also estimated the contribution of N_{fp} during sediment
 178 transfer in the foreland plain and after its definitive burial in the plain, i.e. after its burial below the depth of
 179 potential sediment remobilisation induced by the migration of the channel into its floodplain (section 3.4). The
 180 cosmogenic palaeoproduction rates P at the time of deposition are mainly controlled by the distribution of
 181 elevations in the drainage basin. Therefore, we reconstructed in detail the sediment sources and their evolution
 182 through time using geochemical records, including new major and trace element and Sr-Nd isotopic analyses
 183 (section 3.5).

184 The cosmogenic production rates were estimated using the Basinga GIS Tool (Charreau et al., 2019) (Sup.
 185 Info.) and the topography of modern drainage basins expected to be like the past drainage basins. Indeed, H and
 186 O isotopic analyses suggest that the topography of the northern Himalayas has remained similar since the early
 187 Miocene (Gébelin et al., 2013). Sediment provenance analyses also suggest that the drainage systems of several
 188 Himalayan rivers (Yamuna, Ganga, Tinau, Karnali) have remained steady during the late Cenozoic (Mandal et al.,
 189 2019; Szulc et al., 2006). Our calculation excludes corrections for snow and glacial shielding (see Supplementary
 190 Material for justifications) meaning that the derived denudation rates must be considered as maximum values. The
 191 uncertainties on paleo-denudation rates were calculated using a Monte-Carlo simulation similar to Puchol et al.
 192 (2017). This approach explores conservatively the range of all the input parameters (Table A) to provides an
 193 efficient and accurate determination of the uncertainty attached to the calculated paleo-denudation rates.

194

195 *3.2 Cosmogenic ^{10}Be analyses for palaeodenudation rates*

196 Seventeen samples of typically medium to coarse sandstone were collected from the Surai section for
197 ^{10}Be analyses (Fig. 2c). Sampling locations were selected **at maximum at the bottom of 10-20m high cliffs** to
198 minimize possible **post burial** recent exposures (Fig. 2c and d). **We collected samples at maximum at the base of**
199 **paleo-channel to ensure rapid burial and avoid ^{10}Be accumulation. However, Puchol et al. (2017) show that the**
200 **^{10}Be concentrations are independent of the sedimentary facies and the vertical position within each**
201 **sedimentary unit.** To document present denudation rates, we also sampled two river-bank deposits in the present-
202 day West Rapti River: Rap-Cos1 was collected upstream of the Siwaliks (~5 km north of the MBT, Fig. 2a) and
203 Rap-Cos2 was sampled north of the Dundwa ridge, just north of the Siling thrust at the Bahlubang bridge (Fig. 2a
204 and b). Because we suspected high denudation rates ($>1\text{ mm a}^{-1}$), and therefore very low initial ^{10}Be concentrations
205 in the sampled sediments, we sampled unusually large masses of sand (sometimes $>5\text{ kg}$) to ensure enough pure
206 quartz to provide detectable amounts of ^{10}Be . The sample treatment and ^{10}Be analysis procedures are detailed in
207 the supplementary material.

208

209 *3.3 Age model: magnetostratigraphy, stochastic correlations, and cosmogenic burial ages*

210 We collected 36 new samples for palaeomagnetic analyses (Figs. 2 and 3) in the upper conglomeratic part
211 of the section. Because most of the layers were either too coarse for palaeomagnetic analysis or not amenable to
212 drilling, we sampled only the finer silty to sandy horizons by hand by inserting quartz cylinders. We established
213 the magnetic polarity sequence of the Surai section by incorporating our results (see the Supplementary
214 information for more technical details) into the 436 samples analysed and interpreted by Appel et al. (1991).
215 Magnetic intervals were identified as at least two successive horizons with the same polarity. This revised column
216 (see Supplementary information for the depth of the polarity intervals) was then correlated to the reference scale
217 of Ogg (2012) to establish the depositional ages of the section. To minimize ambiguities and uncertainties related
218 to these correlations, we used a numerical method based on the dynamic time warping (DTW) algorithm
219 (<https://www.ring-team.org/software/downloads>) (Lallier et al., 2013) and automatically calculated 10,000
220 reasonably likely correlations. In this approach, the correlations are computed to minimize the local variation of
221 the accumulation rate **and ranked based on the calculation of a cost.**

222 To estimate $^{26}\text{Al}/^{10}\text{Be}$ cosmogenic burial ages in the upper part of the section, (e.g., Granger and Muzikar,
223 2001), five of the ^{10}Be samples were also analysed for ^{26}Al , and we measured both ^{10}Be and ^{26}Al in three other
224 quartzite pebbles (Table 1). The corresponding burial ages were then calculated from the measured ^{10}Be and ^{26}Al
225 concentrations and the mean elevation of the present drainage basin using the Matlab® code of Blard et al. (2019).

226

227 *3.4 ^{10}Be accumulation in the flood plain*

228 Charreau et al. (2011) and Puchol et al. (2017), based on on the sedimentological analysis of the foreland
229 sediments (Charreau et al., 2009), assumed that sediments in the Tianshan foreland are nearly continuously and
230 progressively buried at a rate equal to the long-term ($>100\text{-ka}$) mean deposition rate, and therefore that ^{10}Be
231 accumulation during transport is minimal. This implies grain transport without interaction with the plain, and
232 deposition of thin, regular sediment layers. **However, rivers draining through the Ganga plain are much larger,**
233 **deeper and active than in the northern Tian Shan piedmont. They display rapid channel migration or avulsion**
234 **(Sinha, 2009; Sinha et al., 2005), whether they are braided in their upper reach or meandering in their lower reach.**
235 **In the case of the modern Karnali river for example, observations on satellite images over the last two decades**

236 indicate an average lateral migration of its channel of $\sim 70\text{m/a}$ all along its course in the Ganga plain. A direct
237 consequence of this lateral migration is bank erosion on one side and bank deposition on the other side. Sediment
238 transfer through the floodplain is therefore better characterized by successive phases of (1) brief periods of
239 transport, (2) temporary deposition in the floodplain, (3) floodplain and bank erosion followed by a new phase of
240 transport. Through bank erosion and deposition, sediments are constantly exchanged between the active channel
241 and the floodplain. For the Himalayan setting we therefore need to account for this sediment reworking and
242 exchange to estimate the floodplain contribution (N_{fp}) and ^{10}Be accumulation during sediment transfer and final
243 burial.

244 Lauer and Willenbring (2010) proposed a simplified steady-state mass-balance model accounting more
245 realistically for cosmogenic nuclide accumulation during sediment transfer within a foreland basin. In this model,
246 already applied to the Ganga plain by Lupker et al. (2012b), floodplain sediments are regularly reworked by
247 channel migration across the fan surface (considered as rectangular), and final sediment burial occurs through the
248 base of the channel, i.e., when sediments are buried deeper than the mean channel reworking depth. Although this
249 model represents a strong simplification of river dynamics, we use it but deprived of lateral supply (generally
250 negligible along proximal parts of the Himalayan river fans) to predict the first-order evolution of ^{10}Be
251 accumulation during floodplain transfer (see Supplementary information). More importantly, we hypothesize that
252 this model, calibrated through observations on modern Karnali or Rapti rivers, can be applied to describe plain
253 dynamic in the past. Such assumption is primarily based on the fact that external forcing like subsidence rates or
254 incoming Himalayan sediment flux have remained roughly stable since 6Ma as described further in the text
255 (section 4). It is also supported by sedimentologic description of the middle Siwalik facies along the Surai Khola
256 section: this formation that presents thick, cross-bedded, multi-stored sandstones was presumably laid down by
257 wide, braided river systems, and the presence of erosive bases attests for continuous reworking during the erosional
258 and aggradational cycles due to stream migration (Corvinus and Rimal, 2001).

259

260 *3.5 Tracing sediment sources: major element and Sr and Nd isotopic analyses*

261 The three main Himalayan units are distinguishable by their unique ϵNd and $^{87}\text{Sr}/^{86}\text{Sr}$ ratios characteristics
262 and can be tracked back in sediments (Deniel et al., 1987; France-Lanord et al., 1993; Morin, 2015; Parrish and
263 Hodges, 1996; Robinson et al., 2001). Moreover, major element data allow the characterization of sediment sorting
264 (for example, Al/Si and Fe/Si ratios are closely related to grain size; Lupker et al., 2011), and apparent weathering
265 intensity (i.e., K/Al and Na/Si ratios, because Na and K are mobile elements potentially affected by weathering;
266 Lupker et al., 2012b). Such approaches provide information critical to identifying reworking in weathered
267 sediments or potential changes in sediment sources (e.g., Mandal et al., 2019).

268 We refined the existing Surai section record (Huyghe et al., 2001; Robinson et al., 2001; Szulc et al.,
269 2006), especially in the upper part of the section where sampling has been less dense. We analysed the major
270 element compositions of 14 new samples of silts and fine sandstones (SU-PM2 to 38), adding to the 35 samples
271 already analysed by Lupker et al. (2012b) (samples 94-04 to 94-60 in their Table 2). We also analysed present
272 Rapti River sands collected at the outlet of the LH (Rap-Cos1) and 200 km downstream, at the front of the MFT
273 (Nag9, Fig. 2a).

274

275 **4. Results and interpretations**

276 *4.1 Age model from magnetostratigraphic data and $^{26}\text{Al}/^{10}\text{Be}$ burial ages*

277 We found a consistent demagnetization pattern in 31 of our 36 samples (Figure 3a–c) (see supplementary
278 information for more technical details) with unambiguous and robust polarities despite low magnetic signal.
279 Among the 31 analysed samples, 19 can be interpreted as having primary magnetizations direction and 12 had
280 remanence trajectories spread out about great circles (Fig. 3d) that never reached stable endpoints but had clear
281 polarities. These 31 samples were considered to construct the magnetostratigraphic column (Fig. 4f). The resulting
282 magnetostratigraphic column based on these new data and 436 previously analysed samples (Appel et al., 1991,
283 with stratigraphic depths from Rosler et al., 1997) is presented in Figure 4 and compared to the previous columns
284 of Appel et al. (1991), Rosler et al. (1997), and Ojha et al. (1999). It includes 24 and 23 normal and reversed
285 polarity intervals, respectively. To correlate this polarity column to the reference scale, the reverse interval r5,
286 which relied on only two samples of the same polarity, was arbitrarily omitted during the calculations (see
287 supplementary material for justification). Figure 4f shows the density plot compiling the 10,000 possible
288 correlations to the reference scale calculated using the DTW algorithm (Lallier et al., 2013). All found correlations
289 date the Surai section to between ~13–14 Ma and ~1–2 Ma (chrons C5A to C1), broadly similar to the previous
290 calculations that considered all polarity intervals. However, our new accumulation rates are, on average, more
291 steady and likely more realistic.

292 ^{26}Al analyses were successful for only 7 of the 10 samples analysed, returning associated burial ages
293 ranging from 2.4 ± 1.4 to 0.6 ± 0.8 Ma (Table 1). The ^{26}Al contents of the three remaining samples were below
294 the detection limit ($< \sim 5 \times 10^3$ at g^{-1}), two of which (Cos8 and Cos16) correspond to the oldest sediments of the
295 record. The burial ages are burdened by large error bars that can reach 100% because of high analytical
296 uncertainties on both ^{10}Be and ^{26}Al concentrations and do not allow to constrain the burial ages better than 0.8Ma.
297 Though they do not provide data critical to better constraining the depositional ages in the upper part of the Surai
298 section, these burial ages remain, at first order, consistent with the proposed magnetostratigraphic correlations
299 (Fig. 4). Unfortunately, given the uncertainties attached to both these burial ages and their respective depositional
300 ages, it is impossible by comparing the two set of ages (Fig. 4h) to identify neither sediments recycling nor recent
301 re-exposure.

302

303 *4.2 Major element and Sr-Nd isotopic compositions: evidence of a drainage change at 3–4 Ma?*

304 The complete geochemical results measured along the Surai section, combining our new analyses with
305 previously published data (Huyghe et al., 2001; Lupker et al., 2012b; Robinson et al., 2001; Szulc et al., 2006) are
306 listed in Supplementary Table D. The main data are presented in age logs (Fig. 5) and in Na/Si vs. Al/Si and Sr vs.
307 ϵNd plots (Fig. 6) with data from modern river sediments for comparison.

308 The Sr and Nd isotopic compositions of the silicate fractions are relatively close to the HHC and TSS
309 endmembers of Morin (2015): $^{87}\text{Sr}/^{86}\text{Sr}$ ratios range from 0.724 to 0.795 and ϵNd values from –19.2 to –14.7 (Fig.
310 6b). Neither isotopic composition displays any temporal variation (Fig. 5). The two modern Rapti River sediments
311 plot in the middle of the Surai section sample array. These data suggest that the palaeodrainage basin of the Surai
312 section has been dominated by erosion of the High Himalaya (HHC and TSS), with secondary contributions (0–
313 30%) from the LH.

314 Siwalik sediments in the Surai section have Al/Si ratios ranging between 0.03 and 0.34. With a few
315 exceptions, sediments older than ~3.5 Ma show Al/Si > 0.1, whereas several samples from the upper part of the

316 section (i.e., younger than ~3.5 Ma) present Al/Si < 0.1, markedly below those of bed sediments or sandy banks
317 of modern Himalayan front rivers, including the rivers draining the Siwaliks (Figs. 5 and 6, Supplementary Table
318 D). These results suggest a higher degree of sediment sorting than observed in modern main Himalayan rivers and
319 floodplain banks. Yet, as the Himalayan range has encroached on the foreland basin, one may expect the length of
320 transport to decrease toward the top of the section (Fig. 7), and hence the depositional area to be more proximal,
321 resulting in decreased sorting. Consistently, to reach such low Al/Si values (<0.1) in the samples younger than ca.
322 3.5 Ma may require multiple episodes of erosion/transport of sediments that had already been sorted, potentially
323 indicating the recycling of older Siwalik sediments already transported into the depositional plain.

324 Sediments of the Surai section have Na/Si ratios ranging from 0.001 to 0.035 that tend to decrease with
325 decreasing depositional age, reaching values below 0.005 in the upper part of the section (i.e., younger than ~3–4
326 Ma). Na/Si ratios in the Surai section are far lower than those of the Ganga in Bangladesh (0.3–0.4), implying that
327 weathering reactions affecting plagioclase were intense in the Surai section sandstones either at the time of
328 deposition (Lupker et al., 2012b) and/or during recent exhumation of the Siwalik folds (France-Lanord et al.,
329 2003). Na concentrations in the Surai section are also markedly depleted compared to those in modern main
330 Himalayan river sediments, which have Na/Si ratios ranging between 0.035 and 0.055 (Figs. 5 and 6,
331 Supplementary Table D). Only the Karnali River is characterized by lower Na/Si ratios between 0.020 and 0.035
332 that are comparable to those of the lower (>3–4 Ma) part of the Surai section, which has been attributed to a
333 significant contribution from erosion of the Siwaliks (Lupker et al., 2012b). In contrast, the Na/Si ratios of
334 sediments younger than ~3–4 Ma are significantly lower than those observed in Siwalik rivers, suggesting a higher
335 degree of weathering for the upper conglomeratic part of the section. The increased weathering intensity in the
336 upper part of the section is further supported by the higher degree of carbonate dissolution indicated by the lower
337 CaO concentrations observed in sediments younger than 4 Ma (mean = 5.4 wt%, σ = 6.3) compared to older
338 sediments (mean = 11.6 wt%, σ = 8.3; Supplementary Table D). This evolution (i.e., increased plagioclase
339 weathering and carbonate dissolution upsection) is counter-intuitive, as one would expect the amplitude of
340 weathering to decrease as deposition nears the Himalayan front and the residence time in the Ganga plain surface
341 decreases. The most intense sediment weathering, as expressed by very low Na/Si values, therefore requires
342 additional weathering. Such a process could occur in-situ during sediments exhumation toward the surface and
343 could be favoured by the coarser grain size and hence the higher permeability found at the top of the section.
344 However, first, if such process occurs, we would expect low Na/Si values at other stratigraphic level of the section
345 where the grain size is also locally coarse (Fig. 4). Second, the sampled sediments were fresh as recently excavated
346 by the construction of the road. Third, the grain size of the samples is similar throughout the section and fourth,
347 the low Al/Si values found at the top request additional sorting and transport that can not be made in-situ.
348 Alternatively, additional weathering can be met for Siwalik sediments derived from already altered materials, for
349 example by recycling of older Siwalik sediments. In such a case, sediments younger than ~3–4 Ma might represent
350 sediments affected by two successive weathering cycles during the Himalayan orogeny.

351 Although Sr-Nd isotopic tracers reveal only that the palaeodrainage basin of the Surai section remained
352 essentially steady, our and previous major element data indicate both (1) a strong increase in plagioclase
353 weathering (leading to Na/Si ratios nearing zero) and (2) the appearance of well sorted sand since 3–4 Ma. Among
354 the sediments exported by the modern river system in Nepal (Fig. 6a), only rivers that dominantly drain the
355 Siwaliks carry sediments comparably well sorted (low Al/Si) and Na-depleted as those in the Surai section (Fig.

356 6b, Supplementary Table D). The geochemical characteristics of sediments in the Surai section are therefore
357 consistent with an increasing proportion of sediment derived from recycling of the Siwaliks, not directly eroded
358 from the High Himalaya. We note that such recycling is not incompatible with the stability of the Sr-Nd isotopic
359 dataset, as recycling does not impact the original source signal (Lupker et al., 2012b; Morin, 2015).

360 Despite very high denudation rates ($>1 \text{ mm a}^{-1}$ Lavé and Avouac, 2000) the small areal contribution of
361 the Siwalik Hills to the drainage basins of most trans-Himalayan rivers prevents sediments in these large drainage
362 basins from becoming significantly depleted in Na (or Al) upon addition of Siwalik-derived material (Fig. 6). For
363 recycled, more mature Siwalik sediments to affect a marked change in the major element signal, as observed in
364 the upper part of the Surai section, the relative sediment flux from terrains north of the MBT must be strongly
365 reduced. We therefore interpret the major compositional change observed in the Surai section at $\sim 3\text{--}4 \text{ Ma}$ (Fig. 5)
366 as a shift of the contributing drainage basin from a trans-Himalayan basin towards one draining the **Lesser**
367 **Himalaya** (Fig. 7), characterized by reduced sediment flux due to a smaller basin area north of the MBT and greatly
368 reduced erosion rates in the **Lesser Himalaya** compared to the High Himalayan regions (Godard et al., 2014). This
369 process does not require a reorganization of the river network across the mountain range **in the Karnali region** but
370 can simply arise from steady facies migration in the Ganga plain during the growth and southward migration of
371 the Himalayan range. As the locus of sedimentation associated with the Surai section progressively migrated
372 towards the Himalayan front, the proportion of recycled Siwalik sediment could have suddenly increased upon
373 crossing a boundary between two alluvial fans associated with a trans-Himalayan and a medium-sized drainage
374 basin (Fig. 7).

375

376 *4.3 Measured cosmogenic concentrations, corrections, and palaeoconcentrations*

377 The complete results of our cosmogenic analyses are presented in Table 1 (raw data are provided in
378 Supplementary Tables E). The measured ^{10}Be concentrations are on average relatively low and range between
379 (1.00 ± 0.36) to $(5.22 \pm 0.98) \times 10^3$ at g^{-1} . They decrease with increasing depositional age, as expected *a priori*
380 from radioactive decay (Table 1). The **relative** uncertainties on these concentrations, which mainly arise from
381 accelerator mass spectrometer counting statistics, are higher in the oldest strata, in which the measured
382 concentrations are lower.

383 The modelled ^{10}Be contributions during transport in the Ganga plain are reported in Supplementary Table
384 C. They range from (1.2 ± 0.2) to $(1.6 \pm 0.3) \times 10^3$ at g^{-1} and from (1.3 ± 0.2) to $(2.4 \pm 0.7) \times 10^3$ at g^{-1} considering
385 the Karnali and Rapti fans, respectively. Although these values were calculated based on modern rivers, they may
386 also represent the ^{10}Be contribution at the time of deposition. These contributions represent 4 to 20% of the total
387 measured cosmogenic concentrations after correction for radioactive decay, irrespective of the fan model (Karnali
388 vs. Rapti).

389 After correcting for radioactive decay and floodplain exposure, the ^{10}Be palaeoconcentrations of
390 sediments leaving the Himalayan range **that are** directly related to its denudation, range between (4.9 ± 3.6) and
391 $(29.8 \pm 9.8) \times 10^5$ at g^{-1} (Table 1). The correction for floodplain exposure was applied consistent with a change of
392 the contributing basin area due to facies migration at 4-3 Ma (see section 4.2): the floodplain corrections for
393 sediments deposited before and after 4-3 Ma were based on the modern Karnali and Rapti Rivers, respectively.

394

395 *4.4 Palaeodenudation rates*

396 Again, consistent with a change of the contributing basin area due to facies migration at 4–3 Ma, we
397 assumed that the topography of the drainage basin was similar to that of the present-day Rapti catchment during
398 3–0 Ma. The basin-averaged ^{10}Be cosmogenic surface production rates during this period were therefore estimated
399 to be 10.95, 0.02, and 0.05 at $\text{g}^{-1} \text{a}^{-1}$ for spallation and slow and fast muogenic processes, respectively. During 6–
400 3 Ma, we considered that the catchment area was draining the entire Himalayas and estimated cosmogenic
401 production rates of 39.59, 0.04, and 0.06 at $\text{g}^{-1} \text{a}^{-1}$ for spallation and slow and fast muogenic processes,
402 respectively.

403 Between 6 and 3.5 Ma, denudation rates were relatively steady at around $1.7 \pm 0.3 \text{ mm a}^{-1}$ in the palaeo-
404 Karnali basin (Table 1 and Fig. 8) (except for one sample that returned a rate of $\sim 3.9 \text{ mm a}^{-1}$, but which was
405 affected by a large uncertainty of $\pm 2.7 \text{ mm a}^{-1}$). Palaeodenudation rates associated with a Rapti-type drainage basin
406 during 3–0 Ma were lower, ranging from 0.6 ± 0.2 to $1.6 \pm 1.1 \text{ mm a}^{-1}$, but denudation rates markedly increased
407 during 1.5–0.5 Ma (Table 1 and Fig. 8). These values are higher than the modern denudation rates of 0.36 ± 0.03
408 and $0.33 \pm 0.03 \text{ mm a}^{-1}$ that we determined for present-day Rapti sediments upstream of the MBT, i.e., without
409 any contribution from the actively uplifted and exhumed frontal fold. Only three samples (Cos14, 19, and 21;
410 Table 1) returned palaeodenudation rates consistent (within uncertainties) with this modern rate.

411

412 5. Discussion

413 5.1 Robustness of the reconstructed ^{10}Be palaeoconcentrations and derived palaeodenudation rates

414 ^{10}Be accumulation during sediment transport was likely of second order compared to that during
415 denudation of the source rocks. Our sediment transport model, though simplified and strongly based on present-
416 day basin characteristics, suggests that ^{10}Be concentrations increased by less than 10 and 15% of the concentrations
417 in modern Rapti and Karnali sediments, respectively, during transport. We therefore extrapolate such moderate
418 contributions during transport to the older deposits (though we note that this is dependent on our choice of model).
419 This contrasts, however, with Charreau et al.'s (2011) approach to estimate floodplain exposure by the steady
420 sedimentation of thin sediment sheets at the long term subsidence rate ($\sim 0.5 \text{ mm/a}$), which predicted contributions
421 during accumulation of $\sim 7.3 \times 10^3$ at g^{-1} , or 40–600% of the total measured concentrations. These would make
422 the correction for accumulation higher than the measured concentration and demonstrate that the approach of
423 Charreau et al. (2011) to calculate the contribution of ^{10}Be accumulation in the floodplain is not appropriate for
424 the case of the Himalayan foreland.

425 In the lower part of the section (up to 2,500 m stratigraphic depth, reverse interval r9), our
426 magnetostratigraphic correlations agree relatively well with previous correlations. The depositional ages and hence
427 the derived ^{10}Be palaeoconcentrations in this lower part of the section are robust and reliable. Upsection,
428 correlation of the n5–n9 sequence remains problematic but our new sampling documents the existence of several
429 reversals and protracted periods of reversed polarities, suggesting that sediment deposition did not stop around 3
430 Ma (normal reference chron C2An), but lasted another several hundreds of thousands of years, probably even more
431 up to the base of Matuyama chron (C1) around 0.7 Ma. Despite those uncertainties, the difference, for a given
432 stratigraphic level, between the minimum and maximum ages found from all the 10000 correlations never exceeds
433 $\sim 1 \text{ Ma}$ (Fig. 4). Hence and to the first order, our denudation rates and their temporal evolution are similar even
434 when considering extreme age models (Supplementary Fig. B).

435 Our interpretation that the contributing drainage basin shifted at ~4–3 Ma is consistent with detrital apatite
436 fission-track (AFT; van der Beek et al., 2006) and Ar-Ar ages (Szulc et al., 2006) that show a ~2 Ma increase in
437 lag time (based here on our revised ages) after ~4–3 Ma (Fig. 9). Such an increased depositional lag time is evident
438 even if we consider the magnetostratigraphic correlation that gives the oldest depositional ages in the upper part
439 of the section (i.e., dating the top at ~2 Ma; Fig. 4). This increased lag time may reflect either (1) decreased
440 exhumation rates across the drainage basins or (2) the reworking of older detrital grains. Indeed, the AFT age at
441 the top of the section is older than those lower in the section (Supplementary Fig. C; van der Beek et al., 2006); as
442 this is unrealistic in such an orogenic setting, it suggests the reworking of older grains. **However, some cautions**
443 **are needed because the increase in thermochronological lag-time is supported by only one AFT sample and is not**
444 **seen in the ZFT data.** But, similarly, provenance analyses of the Mohand-Rao sections (northwest India) evidence
445 the recycling of Siwalik sediments, there starting at ~5.5 Ma (Mandal et al., 2019). We therefore continue our
446 discussion under the assumption that the contributing drainage basin migrated across distinct zones of fan
447 deposition at 3–4 Ma and subsequently recycled older Siwalik sediments.

448 The impact of such sediment recycling on our derived denudation rates must be evaluated before
449 discussing the palaeo-denudation rates. The ^{10}Be concentrations measured at the outlet of the palaeo-Rapti basin
450 reflect the mixing of ^{10}Be -enriched sediments from the **Lesser Himalaya** with ^{10}Be -depleted sediments from the
451 rapidly exhuming frontal Siwaliks folds. However, the initial concentrations in Siwalik sediments before
452 exhumation **may not** be null, **and could be** inherited from the original Mio-Pliocene erosion of the Himalayan
453 **ranges** and vary according to the exhumation level. **Most original ^{10}Be in the older Lower and Middle Siwaliks**
454 **sediments has already radioactively decayed.** The incorporation of such depleted sediments could lower the
455 **concentration measured in the river.** Siwalik sediments eroded and shed to the river between the two modern
456 **samples (RapCos 1 and 2) are mainly Middle to Lower Siwalik.** Yet, the ^{10}Be concentrations measured in the two
457 **samples are not significantly different likely because the addition in RapCos1 represents less than 10% of the**
458 **drainage area of Rap-Cos2, and secondly, because this drained Siwalik part is not the most active one in terms of**
459 **tectonic uplift and therefore probably in terms of erosion (Lavé and Avouac, 2000).** Alternatively, in the younger
460 **Upper Siwaliks sediments the initial and inherited ^{10}Be concentrations has not yet radioactively decayed and**
461 **remain elevated.** During the past, the erosion of the most frontal and rapidly uplifting structures may have produced
462 **a significant volume of such younger enriched sediments equivalent to the Upper Siwalik and biased the**
463 **cosmogenic signal.** To explore **further** potential variations of denudation in the palaeo-Rapti basin, we therefore
464 built a simple model of frontal fold erosion and sediment mixing with a **LH**-draining river such as the Rapti River
465 (see Supplementary materials for more details). We calculated, as a function of the time since fold initiation
466 (assumed at 3 Ma), the evolution of the ^{10}Be concentration expected from the denudation of the Siwalik Hills only
467 (N_{Siv}) and the final concentration after mixing of recycled Siwalik sediments with sediments shed from the
468 upstream midland basin above the MBT (N_{out}). **Consistent with modern ^{10}Be concentrations measured in the Rapti**
469 **basin upstream of the Siwaliks at the MBT, we assumed that the upstream sediments shed from the Rapti basin**
470 **during Siwaliks reworking have a steady ^{10}Be concentration of $(\sim 20 \pm 2) \times 10^3$ at g^{-1} .** We hence assume a steady
471 **denudation rates ~ 0.3 mm/a across the Rapti basin upstream of the Siwaliks at the MBT.** The mean ^{10}Be
472 **concentration of the reworked Siwalik sediments can be inferred from the concentration measured in 7–3 Ma**
473 **sediments in the Surai section, corrected for radioactive decay and transport in the floodplain $(\sim 17 \pm 6) \times 10^3$ at**
474 **g^{-1} .**

475 The model results are shown in **Figure 10** and compared to the ^{10}Be palaeoconcentrations measured in
476 0–3 Ma sediments of the Surai section. Within errors, the measured palaeoconcentrations are consistent with the
477 modelled N_{out} values. The model also indicates that the ^{10}Be concentrations may vary by a factor of >2 between
478 the early and later stages of frontal fold development due to the exhumation of Siwalik sediments with variable
479 ^{10}Be inheritances. Although the model results are strongly dependent on various parameters (e.g., the relative areas
480 of the Midland and Siwalik parts of the catchment, and the erosion rate of the Midland), the model yields two
481 important insights. First, the variations of ^{10}Be palaeoconcentrations measured in Surai sediments younger than
482 ~ 3.5 Ma may reflect frontal fold activity, or even steady fold accretion, and not necessarily a change of erosion
483 rate in the contributing drainage basin. Second, the low ^{10}Be concentrations measured in the upper Surai section,
484 which are up to 5 times lower than present-day concentrations in Rapti River sediments above the MDT, can
485 indeed be explained by mixing with ^{10}Be -depleted material shed from rapidly exhumed Siwalik sandstone in the
486 hanging wall of the MFT. Therefore, we propose that recycling of Na- and ^{10}Be -depleted materials through
487 denudation of the Siwalik belt has strongly impacted the chemistry and ^{10}Be concentrations of the sands exported
488 by frontal- or midland-draining rivers and their associated fan deposits; additional measurements (major elements,
489 ^{10}Be , ϵ_{Nd}) of recent Rapti River sediments up- and downstream of the MFT fold should be performed to fully
490 ascertain our assessment. To reconstruct palaeodenudation rates from in situ cosmogenic ^{10}Be analyses of foreland
491 sediments, it is therefore critical to trace potentially recycled sediments. In the Himalayas, although Sr-Nd isotopes
492 have been widely used to study sediment provenance, our results and **those of Mandal et al. (2019)** suggest that
493 these geochemical proxies are insensitive to sediment recycling, which is better identified by simpler major and
494 trace element analyses, notably Al/Si and Na/Si, which are linked to weathering and sorting processes, respectively
495 (Lupker et al., 2012b, 2011).

496

497 *5.2 Implications for the late Cenozoic evolution of denudation rates in the central Himalayas*

498 The palaeodenudation rates associated with the Karnali-type basin from ~ 6 to 3 Ma are close to the
499 modern denudation values measured along the Karnali downstream of the Siwaliks (Fig. 8; Lupker et al., 2012a).
500 Though denudation rates since 3.5 Ma for a Karnali-type basin are missing from our record, this similarity might
501 suggest that average denudation rates in the Karnali basin **may** have remained steady at around $\sim 1.7 \pm 0.3 \text{ mm a}^{-1}$
502 since ~ 6 Ma. For the period 3–0 Ma and sediments associated with smaller basins like the Rapti, direct comparison
503 of ^{10}Be palaeodenudation rates and observed modern denudation rates is complicated by the recycling of Siwalik
504 sediments. If we accept that the low ^{10}Be concentrations measured in the upper Surai section (<3 Ma) are related
505 to the recycling of older, ^{10}Be -depleted Siwalik sediments, then our denudation rates should be considered
506 maximum values. Although it is almost impossible to reconstruct the true palaeodenudation rates in the basin
507 upstream of the Siwaliks, our simple sediment mixing model suggests that denudation rates similar to modern rates
508 yield theoretical ^{10}Be concentrations consistent with those measured downstream of the Siwaliks. **Consequently,**
509 **a steady denudation at around $\sim 0.3 \text{ mm a}^{-1}$ since 3 Ma in the palaeo-Rapti basin, together with recycling in the**
510 **Siwalik, could produce the ^{10}Be concentrations that we observe in the Surai section.** Although this conclusion is
511 tentative given the over-simplifications in our recycling model, the range of expected ^{10}Be palaeo- (≥ 0.3 and \ll
512 1.6 mm a^{-1}) and modern Rapti basin denudation rates ($\sim 0.3 \text{ mm a}^{-1}$, as measured above the MDT; Figs. 1, 2, and
513 8) are consistent with denudation rates of $0.1\text{--}0.5 \text{ mm a}^{-1}$ reported in other midland drainage basins of central

514 Nepal (Godard et al., 2014; Scherler et al., 2014). These ^{10}Be data thus suggest that (1) denudation rates are higher
515 in the HHC than in the LH and (2) denudation **may have** remained steady since ~ 6 Ma, at least in the Karnali basin.

516 As no in situ thermochronologically derived denudation rates are available for sites nearer the Karnali
517 and Rapti basins, we compare our ^{10}Be denudation rates to in situ thermochronological data for the Sutlej region
518 (western India, near the Nepal border) and for central Nepal (i.e., at the longitude of Kathmandu). Denudation
519 rates in those areas range between ~ 0.5 and 3 mm a^{-1} (Bojar et al., 2005; Herman et al., 2010; Patel and Carter,
520 2009; Thiede and Ehlers, 2013). Consistent with our findings, thermochronologically derived denudation rates
521 tend to be lower in the LH ($0.3\text{--}0.5 \text{ mm a}^{-1}$) than in the HHC, where rates can reach up to $\sim 3 \text{ mm a}^{-1}$ (e.g., Herman
522 et al., 2010; Thiede and Ehlers, 2013). High denudation rates in the HHC have also been reported from in situ
523 thermochronological data in other regions across the Himalayas (Blythe et al., 2007; Herman et al., 2010;
524 Huntington et al., 2006; Thiede and Ehlers, 2013), and petrological and mineralogical analyses, sediment flux
525 monitoring (Garzanti et al., 2007), and fluvial incision rates (e.g., Lavé and Avouac, 2001) further suggest that the
526 LH denude at lower rates than the HHC. This discrepancy between the LH and HHC is likely due to crustal wedge
527 deformation and **duplexing** along the Main Himalayan Thrust, which orographically triggers monsoonal
528 precipitation, enhancing denudation in the HHC (Herman et al., 2010; Thiede and Ehlers, 2013).

529 To further examine the temporal evolution of our ^{10}Be denudation rates, we compared with denudation
530 histories derived from thermochronological analyses of detrital grains. In the Karnali section, assuming a
531 geothermal gradient of $20 \text{ }^\circ\text{C}$, Bernet et al. (2006) and van der Beek et al. (2006) reported exhumation rates of
532 $\sim 1\text{--}2 \text{ mm a}^{-1}$. In the Surai section, if we consider only the period before the recycling of Siwalik sediments ($>3\text{--}4$
533 Ma), likely also associated with the Karnali basin, revised zircon fission track (ZFT) and Ar-Ar lag times are **on**
534 average ~ 4 and ~ 6 Ma, respectively, whereas AFT ages are similar to depositional ages (Bernet et al., 2006; Szulc
535 et al., 2006; van der Beek et al., 2006) (Supplementary Fig. C). **Van der Beek et al. (2006) assumed** a geothermal
536 gradient of $\sim 20 \text{ }^\circ\text{C}$ and ZFT and Ar-Ar closure temperatures of $240 \text{ }^\circ\text{C}$ and $350 \text{ }^\circ\text{C}$, respectively. **This would yield**
537 respective denudation rates of ~ 3 and $\sim 2.9 \text{ mm a}^{-1}$, markedly higher than ^{10}Be -derived denudation rates for the
538 Karnali and Surai sections. Two effects may explain this discrepancy. First, interpretation and population
539 modelling of detrital age distributions are not straightforward and may suffer from several biases (Naylor et al.,
540 2015; Sundell and Saylor, 2017). Indeed, recent slow denudation rates may be **unrepresented** to detrital analyses
541 because the rocks may have not yet reached the surface (Naylor et al., 2015; Willenbring and Jerolmack, 2016),
542 yielding overestimated denudation rates during the last few million years. Moreover, as detrital denudation rates
543 are derived by comparing only the youngest peak to depositional ages, such denudation rates are maximum values
544 that may preferentially sample the most eroding regions within a basin and, hence, may not truly average
545 denudation throughout the basin.

546 Second, detrital thermochronological ages and denudation rates depend on the local geotherm, which may
547 reach $100 \text{ }^\circ\text{C/km}$ in regions of rapid tectonic exhumation (Braun, 2005). Although high geothermal gradients (>50
548 $^\circ\text{C/km}$) were observed in the Namche Barwa region (Craw et al., 2005), this region presents extreme tectonic
549 exhumation rates and thus may not be a good analogue of the Karnali basin. Geothermal gradients of $20\text{--}50 \text{ }^\circ\text{C/km}$
550 have also been reported in central Nepal (Bollinger et al., 2006), but correspond to the LH where denudation is
551 relatively slow ($<1 \text{ mm a}^{-1}$). Therefore, a more realistic value of the average geothermal gradient for the entire
552 Karnali basin is likely $\sim 50 \text{ }^\circ\text{C/km}$, which would yield detrital thermochronological denudation rates of $0.6\text{--}1.2$
553 mm a^{-1} in the Karnali and Surai sections. These values are more consistent with our ^{10}Be -derived rates for a

554 Karnali-type drainage basin. However, these thermochronological denudation rates remain crude estimates. To
555 provide more accurate values a careful reassessment of the detrital thermochronological data is needed including
556 for example Monte Carlo simulations of the age population based on more realistic and spatially variable
557 geothermal gradients (e.g. Brewer et al., 2003).

558 Importantly, Lenard et al. (2020) suggest, from ^{10}Be analyses of the sediments of the Bay of Bengal
559 seabed, a steady denudation across the Himalayas since 6Ma. In the Karnali section, depositional lag times
560 determined from ZFT and AFT ages remain remarkably steady from ~ 14 to ~ 3 Ma and from ~ 7 to ~ 3 Ma,
561 respectively (Bernet et al., 2006; van der Beek et al., 2006). In the Surai section, if we exclude the youngest part
562 of the section where recycling likely occurred (<3 – 4 Ma), lag times determined from AFT, ZFT, and Ar-Ar ages
563 are also relatively steady (Supplementary Fig. C). Even if we cannot fully exclude variable denudation rates in the
564 Karnali basin because we lack direct records since ~ 3 Ma, both ^{10}Be data and previous detrital
565 thermochronological data are at least consistent with steady palaeodenudation rates in the region since
566 the late Miocene. All together, these results suggest a limited impact of Quaternary climatic oscillations on
567 denudation rates in the Himalaya (Lénard et al., 2020) as is the case in the Tianshan range (Puchol et al., 2017) or
568 in the southern California (Oskin et al., 2017). In that sense, they seem to contradict thermochronological data
569 results that document an accelerated Quaternary denudation rates over large mountain ranges (Herman et al.,
570 2013).

571

572 6. Conclusions

573 The Surai section in the central Siwaliks is well suited to reconstruct palaeodenudation rates from in situ
574 cosmogenic ^{10}Be analyses. ^{10}Be concentrations measured in 19 samples were transformed to palaeoconcentrations
575 based on several corrections and to palaeodenudation rates by assuming that cosmogenic palaeoproduction rates
576 were similar to those of the modern drainage basins and a shift from a trans-Himalayan to a midland-draining basin
577 at 4–3 Ma as suggested by major and trace element data. Consequently, we propose that denudation rates in the
578 palaeo-Karnali basin may have been steady around ~ 1.7 mm a^{-1} from ~ 6 to ~ 3 Ma. These denudation rates are
579 similar to modern values observed downstream of the Siwaliks, suggesting steady denudation rates across the
580 Karnali basin since ~ 6 Ma. Our data suggest that denudation rates may have accelerated from ~ 0.4 – 1.1 mm a^{-1}
581 during ~ 3 – 1.5 Ma to ~ 1.5 mm a^{-1} since ~ 1.5 Ma in the palaeo-Rapti basin. However, based on a sediment-mixing
582 model, we argue that this is likely only an apparent acceleration due to the reworking of older Siwalik sediments
583 depleted in ^{10}Be . Consequently, denudation in the Rapti basin upstream of the MBT may have also remained steady
584 at ~ 0.3 mm a^{-1} since ~ 3 Ma. These ^{10}Be -derived denudation rates are consistent with those derived from detrital
585 and in situ thermochronological data. They also suggest varied denudation rates across the range that are likely
586 controlled by deformation of the structural wedge and orographic effects. Our results argue against accelerated
587 Quaternary denudation rates inferred from inversion of 1D thermochronological data, and instead suggest a limited
588 impact of Quaternary climatic oscillations on Himalayan denudation rates. However, testing the impact of
589 glaciations on Himalayan denudation at this scale requires cosmogenic data directly recording denudation during
590 3–0 Ma, which is complicated in the Surai section by basin reorganisation 4–3 Ma ago. Nevertheless, our study
591 demonstrates that it is possible to reconstruct palaeodenudation rates from the in situ ^{10}Be concentrations of buried
592 Siwalik sediments, as long as sediment sources and recycling are traced via several geochemical proxies.

593

594 **Acknowledgements**

595 This study was funded by the ANR CALIMERO. This is CRPG contribution n° 2738. The authors have no conflict
596 of interest to declare. The data that support the study are available in the tables of the main manuscript or in the
597 supplementary information. **We are grateful for the detailed evaluation and reviews provided by T.**
598 **Schildgen G. Burch Fisher, M. Oskin and D. Scherler. Their comments and suggestions permitted to**
599 **improve the manuscript and clarify some issues.**

600

601 **Bibliography**

- 602 Adams, B.A., Hodges, K. V, Whipple, K.X., Ehlers, T.A., Soest, M.C., Wartho, J., 2015. Constraints on the
603 tectonic and landscape evolution of the Bhutan Himalaya from thermochronometry. *Tectonics* 1329–1347.
604 <https://doi.org/10.1002/2015TC003853>.Received
- 605 Appel, E., Rosler, W., Corvinus, G., Munchen, O., 1991. Magnetostratigraphy of the Miocene-Pleistocene Surai
606 Khola Siwaliks in West Nepal 191–198.
- 607 Auden, J.B., 1935. Traverses in the Himalaya. *Rec. Geol. Surv. India* 69, 123–167.
- 608 Bernet, M., van der Beek, P., Pik, R., Huyghe, P., Mugnier, J.-L., Labrin, E., Szulc, A., 2006. Miocene to Recent
609 exhumation of the central Himalaya determined from combined detrital zircon fission-track and U/Pb
610 analysis of Siwalik sediments, western Nepal. *Basin Res.* 18, 393–412. <https://doi.org/10.1111/j.1365-2117.2006.00303.x>
- 612 Blard, P.-H., Lupker, M., Rousseau, M., Tesson, J., 2019. Two MATLAB programs for computing paleo-
613 elevations and burial ages from paired-cosmogenic nuclides. *MethodsX* 6, 1547–1556.
- 614 Blythe, A.E., Burbank, D.W., Carter, A., Schmidt, K., Putkonen, J., 2007. Plio-Quaternary exhumation history of
615 the central Nepalese Himalaya: 1. Apatite and zircon fission track and apatite [U-Th]/He analyses.
616 *Tectonics* 26. <https://doi.org/10.1029/2006tc001990>
- 617 Bojar, A.V., Fritz, H., Nicolescu, S., Bregar, M., Gupta, R.P., 2005. Timing and mechanisms of Central
618 Himalayan exhumation: Discriminating between tectonic and erosion processes. *Terra Nov.* 17, 427–433.
619 <https://doi.org/10.1111/j.1365-3121.2005.00629.x>
- 620 Bollinger, L., Henry, P., Avouac, J.P., 2006. Mountain building in the Nepal Himalaya : Thermal and kinematic
621 model. *Earth Planet. Sci. Lett.* 244, 58–71. <https://doi.org/10.1016/j.epsl.2006.01.045>
- 622 Braucher, R., Merchel, S., Borgomano, J., Bourlès, D.L., 2011. Production of cosmogenic radionuclides at great
623 depth : A multi element approach. *Earth Planet. Sci. Lett.* <https://doi.org/10.1016/j.epsl.2011.06.036>
- 624 Braun, J., 2005. Quantitative Constraints on the Rate of Landform Thermochronology. *Rev. Mineral.*
625 *Geochemistry* 58, 351–374. <https://doi.org/10.2138/rmg.2005.58.13>
- 626 Brewer, I.D., Burbank, D.W., Hodges, K. V, 2003. Modelling detrital cooling-age populations : insights from
627 two Himalayan catchments. *Basin Res.* 15, 305–320.
- 628 Brown, E.T., Stallard, R.F., Larsen, M.C., Raisbeck, G.M., Yiou, F., 1995. Denudation rates determined from
629 the accumulation of in situ produced ¹⁰Be in the Luquillo experimental forest, Puerto-Rico. *Earth Planet.*
630 *Sci. Lett.* 129, 193–202.
- 631 Burbank, D.W., Derry, L.A., France-Lanord, C., 1993. Reduced Himalayan sediment production 8 Myr ago
632 despite an intensified monsoon. *Nature* 364, 48–50.

- 633 Charreau, J., Blard, P.-H., Zumaque, J., Martin, L.C.P., Delobel, T., Szafran, L., 2019. Basinga: A cell-by-cell
634 GIS toolbox for computing basin average scaling factors, cosmogenic production rates and denudation
635 rates. *Earth Surf. Process. Landforms* 44, 2349–2365.
- 636 Charreau, J., Blard, P.H., Puchol, N., Avouac, J.P., Lallier-Vergès, E., Bourlès, D., Braucher, R., Gallaud, A.,
637 Finkel, R., Jolivet, M., Chen, Y., Roy, P., 2011. Paleo-erosion rates in Central Asia since 9Ma: A transient
638 increase at the onset of Quaternary glaciations? *Earth Planet. Sci. Lett.* 304, 85–92.
639 <https://doi.org/10.1016/j.epsl.2011.01.018>
- 640 Charreau, J., Chen, Y., Gilder, S., Barrier, L., Dominguez, S., Augier, R., Sen, S., Avouac, J.-P., Gallaud, A.,
641 Graveleau, F., Wang, Q., 2009. Neogene uplift of the Tian Shan Mountains observed in the magnetic
642 record of the Jingou River section (northwest China). *Tectonics* 28, 1–22.
643 <https://doi.org/10.1029/2007TC002137>
- 644 Clift, P.D., 2006. Controls on the erosion of Cenozoic Asia and the flux of clastic sediment to the ocean. *Earth*
645 *Planet. Sci. Lett.* 241, 571–580.
- 646 Corvinus, G., Rimal, L.N., 2001. Biostratigraphy and geology of the Neogene Siwalik Group of the Surai Khola
647 and Rato Khola areas in Nepal. *Palaeogeogr. Palaeoclimatol. Palaeoecol.* 165, 251–279.
- 648 Craw, D., Koons, P.O., Zeitler, P.K., Kidd, W.S.F., 2005. Fluid evolution and thermal structure in the rapidly
649 exhuming gneiss complex of Namche Barwa – Gyala Peri , eastern Himalayan syntaxis. *J. Metamorph.*
650 *Geol.* 23, 829–845. <https://doi.org/10.1111/j.1525-1314.2005.00612.x>
- 651 DeCelles, P.G., Gehrels, G.E., Quade, J., Ojha, T.P., Kapp, P.A., Upreti, B.N., 1998. Neogene foreland basin
652 deposits, erosional unroofing, and the kinematic history of the Himalayan fold-thrust belt, western Nepal.
653 *Geol. Soc. Am. Bull.* 2–21.
- 654 Deniel, C., Vidal, P., Fernandez, A., Le Fort, P., Peucat, J.J., 1987. Isotopic study of the Manaslu granite
655 (Himalaya, Nepal): inferences on the age and source of Himalayan leucogranites. *Contrib. to Mineral.*
656 *Petrol.* 96, 78–92. <https://doi.org/10.1007/BF00375529>
- 657 Dhital, M.R., Gajurel, A.P., Pathak, D., Paudel, L.P., Kizaki, K., 1995. Geology and structure of the Siwaliks
658 and Lesser Himalaya in the Surai Khola–Bardanda area, Mid Western Nepal. *Bull. Dept. Geol. Tribhuvan*
659 *Univ.* 4, 1–70.
- 660 Dubille, M., Lavé, J., 2015. Rapid grain size coarsening at sandstone/conglomerate transition: Similar expression
661 in Himalayan modern rivers and Pliocene molasse deposits. *Basin Res.* 27, 26–42.
662 <https://doi.org/10.1111/bre.12071>
- 663 France-Lanord, C., Derry, L., Michard, A., 1993. Evolution of the Himalaya since Miocene time: isotopic and
664 sedimentological evidence from the Bengal Fan. *Geol. Soc. London, Spec. Publ.* 74, 603–621.
665 <https://doi.org/10.1144/GSL.SP.1993.074.01.40>
- 666 France-Lanord, C., Evans, M., Hurtrez, J.E., Riotte, J., 2003. Annual dissolved fluxes from Central Nepal rivers:
667 Budget of chemical erosion in the Himalayas. *Comptes Rendus - Geosci.* 335, 1131–1140.
668 <https://doi.org/10.1016/j.crte.2003.09.014>
- 669 Gansser, A., 1964. *Geology of the Himalayas*, Wiley. ed.
- 670 Garzanti, E., Vezzoli, G., Andò, S., Lavé, J., Attal, M., France-lanord, C., Decelles, P., 2007. Quantifying sand
671 provenance and erosion (Marsyandi River , Nepal Himalaya) 258, 500–515.
672 <https://doi.org/10.1016/j.epsl.2007.04.010>

- 673 Gautam, P., Rosler, W., 1999. Depositional chronology and fabric of Siwalik group sediments in Central Nepal
674 from magnetostratigraphy and magnetic anisotropy. *J. As* 17, 659–682.
- 675 Gébelin, A., Mulch, A., Teyssier, C., Jessup, M.J., Law, R.D., Brunel, M., 2013. The Miocene elevation of
676 Mount Everest. *Geology* 41, 799–802. <https://doi.org/10.1130/G34331.1>
- 677 Godard, V., Bourles, D.L., Spinabella, F., Burbank, D.W., Bookhagen, B., Fisher, G.B., Moulin, A., Leanni, L.,
678 2014. Dominance of tectonics over climate in Himalayan denudation. *Geology* 42, 243–246.
679 <https://doi.org/10.1130/G35342.1>
- 680 Granger, D.E., Muzikar, P.F., 2001. Dating sediment burial with in situ-produced cosmogenic nuclides: theory,
681 techniques, and limitations. *Earth Planet. Sci. Lett.* 188, 269–281.
- 682 Gupta, S., 1997. Himalayan drainage patterns and the origin of fluvial megafans in the Ganges foreland basin.
683 *Geology* 25, 11–15.
- 684 Harrison, T.M., Copeland, P., Hall, S.A., Quade, J., Scott, B., Ojha, P., Kidd, W.S.F., 1993. Isotopic
685 Preservation of Himalaya/Tibetan Uplift, Denudation and Climatic Histories of two Molasse Deposits. *J.*
686 *Geol.* 101, 157–175.
- 687 Hérail, G., Mascle, G., 1980. Les Siwaliks du Népal central : Structure et géomorphologie d'un piémont en
688 cours de déformation (The central nepalese siwaliks : structure and geomorphology of an upheaveling
689 piedmont). *Bull. Assoc. Geogr. Fr.* 471, 259–267.
- 690 Herman, F., Copeland, P., Avouac, J.P., Bollinger, L., Mahéo, G., Fort, P. Le, Rai, S., Foster, D., Pêcher, A.,
691 Stüwe, K., Henry, P., 2010. Exhumation , crustal deformation , and thermal structure of the Nepal
692 Himalaya derived from the inversion of thermochronological and thermobarometric data and modeling of
693 the topography. *J. Geophys. Res.* 115, 1–38. <https://doi.org/10.1029/2008JB006126>
- 694 Herman, F., Seward, D., Valla, P.G., Carter, A., Kohn, B., Willett, S.D., Ehlers, T.A., 2013. Worldwide
695 acceleration of mountain erosion under a cooling climate. *Nature* 504, 423–426.
696 <https://doi.org/10.1038/nature12877>
- 697 Huntington, K.W., Blythe, A.E., Hodges, K. V, 2006. Climate change and Late Pliocene acceleration of erosion
698 in the Himalaya. *Earth Planet. Sci. Lett.* 252, 107–118. <https://doi.org/10.1016/j.epsl.2006.09.031>
- 699 Hurtrez, J.-E., Lucazeau, F., Lavé, J., Avouac, J.-P., 1999. Investigation of the relationships between basin
700 morphology, tectonic uplift, and denudation from the study of an active fold belt in the Siwalik Hills,
701 central Nepal. *J. Geophys. Res.* 104, 12779. <https://doi.org/10.1029/1998JB900098>
- 702 Huyghe, P., Galy, A., Mugnier, J.M., France-Lanord, C., 2001. Propagation of the thrust system and erosion in
703 the Lesser Himalaya : Geochemical and sedimentological evidence. *Geology* 1007–1010.
- 704 Lallier, F., Antoine, C., Charreau, J., Caumon, G., Ruiu, J., 2013. Management of ambiguities in
705 magnetostratigraphic correlation. *Earth Planet. Sci. Lett.* 371–372, 26–36.
706 <https://doi.org/10.1016/j.epsl.2013.04.019>
- 707 Lang, K.A., Huntington, K.W., Burmester, R., Housen, B., 2016. Rapid exhumation of the eastern Himalayan
708 syntaxis since the late Miocene. *Geol. Soc. Am. Bull.* 1–20. <https://doi.org/10.1130/B31419.1>
- 709 Lauer, J.W., Willenbring, J., 2010. Steady state reach - scale theory for radioactive tracer concentration in a
710 simple channel / floodplain system 115, 1–21. <https://doi.org/10.1029/2009JF001480>
- 711 Lavé, J., Avouac, J.P., 2001. Fluvial incision and tectonic uplift across the Himalayas of central Nepal. *J.*
712 *Geophys. Res.* 106, 26561. <https://doi.org/10.1029/2001JB000359>

- 713 Lavé, J., Avouac, J.P., 2000. Active folding of fluvial terraces across the Siwaliks Hills, Himalayas of central
714 Nepal. *J. Geophys. Res.* 105, 5735. <https://doi.org/10.1029/1999JB900292>
- 715 Lénard, S., Lavé, J., France-Lanord, C., Aumaître, G., Bourlès, D., Keddadouche, K., 2020. Steady erosion rates
716 in the Himalayas through late Cenozoic climatic changes. *Nat. Geosci.* 13, 448–452.
- 717 Lupker, M., Blard, P.-H., Lavé, J., France-Lanord, C., Leanni, L., Puchol, N., Charreau, J., Bourlès, D., 2012a.
718 ¹⁰Be-derived Himalayan denudation rates and sediment budgets in the Ganga basin. *Earth Planet. Sci.*
719 *Lett.* 333–334, 146–156. <https://doi.org/10.1016/j.epsl.2012.04.020>
- 720 Lupker, M., France-lanord, C., Galy, V., Gajurel, A.P., Guilmette, C., 2012b. Predominant floodplain over
721 mountain weathering of Himalayan sediments (Ganga basin). *Geochemica Cosmochim. Acta* 84, 410–432.
722 <https://doi.org/10.1016/j.gca.2012.02.001>
- 723 Lupker, M., Lanord, C.F., Lavé, J., Bouchez, J., Galy, V., Métivier, F., Gaillardet, J., Lartiges, B., Mugnier, J.L.,
724 2011. A Rouse - based method to integrate the chemical composition of river sediments : Application to
725 the Ganga basin 116, 1–24. <https://doi.org/10.1029/2010JF001947>
- 726 Lyon-Caen, H., Molnar, P., 1985. Gravity anomalies, flexure of the Indian plate and the structure, support and
727 evolution of the Himalaya and Ganga basin. *Tectonics* 4, 513–538.
- 728 Mandal, S.K., Scherler, D., Romer, R.L., Burg, J.P., Guillong, M., Schleicher, A.M., 2019. Multiproxy Isotopic
729 and Geochemical Analysis of the Siwalik Sediments in NW India: Implication for the Late Cenozoic
730 Tectonic Evolution of the Himalaya. *Tectonics* 38, 120–143. <https://doi.org/10.1029/2018TC005200>
- 731 Métivier, F., Gaudemer, Y., Tapponnier, P., Klein, M., 1999. Mass accumulation rates in Asia during the
732 Cenozoic. *Geophys. J. Int.* 137, 280–318.
- 733 Morin, G., 2015. L'érosion et l'altération en Himalaya et leur évolution depuis le tardi-pleistocène: analyse des
734 processus d'érosion à partir de rivière actuelles et passées au Népal Central, PhD thesis, université de
735 Lorraine.
- 736 Nakayama, K., Ulak, P.D., 1999. Evolution of fluvial style in the Siwalik Group in the foothills of the Nepal
737 Himalaya. *Sediment. Geol.* 125, 205–224.
- 738 Naylor, M., Sinclair, H.D., Bernet, M., van der Beek, P., Kirstein, L.A., 2015. Bias in detrital fission track grain-
739 age populations: Implications for reconstructing changing erosion rates. *Earth Planet. Sci. Lett.* 422, 94–
740 104. <https://doi.org/10.1016/j.epsl.2015.04.020>
- 741 Ogg, J.G., 2012. Geomagnetic Polarity Time Scale, in: Gradstein, F.M. (Ed.), *The Geological Time Scale*.
- 742 Ojha, T.P., Butler, R.F., Decelles, P.G., Quade, J., 2009. Magnetic polarity stratigraphy of the Neogene foreland
743 basin deposits of Nepal 61–90. <https://doi.org/10.1111/j.1365-2117.2008.00374.x>
- 744 Oskin, M., Longinotti, N., Peryam, T., Dorsey, R., DeBoer, C., Housen, B.A., Blisniuk, K., 2017. Steady
745 ¹⁰Be-derived paleoerosion rates across the Plio-Pleistocene climate transition, Fish Creek-Vallecito basin,
746 California. *J. Geophys. Res. Earth Surf.* 122, 1653–1677.
- 747 Parrish, R.R., Hodges, K., 1996. Isotopic constraints on the age and provenance of the Lesser and Greater
748 Himalayan sequence, Nepalese Himalaya. *Geol. Soc. Am. Bull.* 108, 904–911.
- 749 Patel, R.C., Carter, A., 2009. Exhumation history of the higher Himalayan Crystalline along Dhauliganga-
750 Goriganga river valleys, NW India: New constraints from fission track analysis. *Tectonics* 28, 1–14.
751 <https://doi.org/10.1029/2008TC002373>
- 752 Puchol, N., Charreau, J., Blard, P., Lavé, J., Dominguez, S., Pik, R., Saint-carlier, D., ASTER Team, 2017.

- 753 Limited impact of Quaternary glaciations on denudation rates in central Asia. *Geol. Soc. Am. Bull.* 129,
754 479–499.
- 755 Refsnider, K.A., 2010. Dramatic increase in late Cenozoic alpine erosion rates recorded by cave sediment in the
756 southern Rocky Mountains. *Earth Planet. Sci. Lett.* 297, 505–511.
- 757 Robinson, D.M., Decelles, P.G., Patchett, P.J., Garzione, C.N., 2001. The kinematic evolution of the Nepalese
758 Himalaya interpreted from Nd isotopes. *Earth Planet. Sci. Lett.* 192, 507–521.
- 759 Rosler, W., Appel, E., 1998. Fidelity and time resolution of the magnetostratigraphic record in Siwalik
760 sediments: high-resolution study of a complete polarity transition and evidence for cryptochrons in a
761 Miocene fluvial section. *Geophys. J. Int.* 135, 861–875.
- 762 Rosler, W., Metzler, W., Appel, E., 1997. Neogene magnetic polarity stratigraphy of some fluvial Siwalik
763 sections, Nepal. *Geophys. J. Int.* 130, 89–111.
- 764 Schaller, M., von Blanckenburg, F., Veldkamp, A., Tebbens, L.A., Hovius, N., Kubik, P.W., 2002. A 30 000 yr
765 record of erosion rates from cosmogenic ^{10}Be in Middle European river terraces. *Earth Planet. Sci. Lett.*
766 204, 307–320.
- 767 Scherler, D., Bookhagen, B., Strecker, M.R., 2014. Tectonic control on ^{10}Be -derived erosion rates in the
768 Garhwal Himalaya, India. *J. Geophys. Res. Earth Surf.* 119, 83–105.
769 <https://doi.org/10.1002/2013JF002955>
- 770 Sinha, R., 2009. The great avulsion of Kosi on 18 August 2008. *Curr. Sci.* 97, 429–433.
- 771 Sinha, R., Jain, V., Babu, G.P., Ghosh, S., 2005. Geomorphic characterization and diversity of the fluvial
772 systems of the Gangetic Plains. *Geomorphology* 70, 207–225.
773 <https://doi.org/10.1016/j.geomorph.2005.02.006>
- 774 Sundell, K.E., Saylor, J.E., 2017. Unmixing detrital geochronology age distributions. *Geochemistry, Geophys.*
775 *Geosystems* 18, 2872–2886. <https://doi.org/10.1002/2016GC006774>.
- 776 Szulc, A.G., Najman, Y., Sinclair, H.D., Pringle, M., Bickle, M., Chapman, H., 2006. Tectonic evolution of the
777 Himalaya constrained by detrital $^{40}\text{Ar}/^{39}\text{Ar}$, Sm, Nd and petrographic data from the Siwalik foreland
778 basin succession, SW Nepal. *Basin Res.* 18, 375–391. <https://doi.org/10.1111/j.1365-2117.2006.00307.x>
- 779 Thiede, R.C., Ehlers, T.A., 2013. Large spatial and temporal variations in Himalayan denudation. *Earth Planet.*
780 *Sci. Lett.* 371–372, 278–293. <https://doi.org/10.1016/j.epsl.2013.03.004>
- 781 van der Beek, P., Robert, X., Mugnier, J., Bernet, M., Huyghe, P., Labrin, E., 2006. Late Miocene–Recent
782 exhumation of the central Himalaya and recycling in the foreland basin assessed by apatite fission-track
783 thermochronology of Siwalik sediments, Nepal. *Basin Res.* 18, 413–434. <https://doi.org/10.1111/j.1365-2117.2006.00305.x>
- 784
- 785 Wells, N.A., Dorr, J.A., 1977. Shifting of the Kosi River, northern India. *Geology* 15, 204–207.
- 786 Willenbring, J.K., Jerolmack, D.J., 2016. The null hypothesis: Globally steady rates of erosion, weathering
787 fluxes and shelf sediment accumulation during Late Cenozoic mountain uplift and glaciation. *Terra Nov.*
788 28, 11–18. <https://doi.org/10.1111/ter.12185>
- 789
- 790
- 791

792 **Figure captions**

793 **Fig. 1:** Geological map of the central Himalayas. Brown and yellow stars indicate samples collected and analysed
794 by Lupker et al. (2012a).

795

796 **Fig. 2:** Geology of the Rapti River basin and the Surai section in the Siwalik Hills. (a) Geological map of the Rapti
797 river basin; (b) geological map of the Surai region; (c) palaeomagnetic and cosmogenic sampling locations; and
798 (d) geological cross section across the Siwalik Hills showing the projected location of the Surai section. The photo
799 in (d) shows a typical outcrop (and associated shielding) sampled for cosmogenic analyses along the RH01 road.

800

801 **Fig. 3:** Representative Zijdeveld (1967) diagrams of our new palaeomagnetic samples. Samples showed (a)
802 normal polarities (b) reverse polarities, (c) unstable remanent directions, or (d) remanent directions that defined
803 great-circle paths, but nonetheless provided an unambiguous polarity. The 19 stable remanent directions and 12
804 great-circle samples used to refine the magnetostratigraphic column of the upper Surai section are shown in (e)
805 geographic and (f) stratigraphic (tilt-corrected) coordinates.

806

807 **Fig. 4:** Magnetostratigraphic correlation of the Surai section **and cosmogenic burial ages**. (a) Stratigraphic log of
808 the Surai section (after Corvinus and Rimal, 2001); previous magnetostratigraphic columns are after (b) Appel et
809 al. (1991) and (c) Gautam and Rossler (1999) and Rosler (1997); (d) and (e) magnetic declinations and inclinations,
810 respectively (after Gautam and Rosler, 1999), including our new analyses; (f) revised magnetostratigraphic
811 column of the Surai section and its correlation to the reference scale using the DTW algorithm of Lallier et al.
812 (2013), with previous correlations proposed in the literature shown as grey circles; (g) magnetostratigraphic
813 column of Ojha et al. (2009) with Ar-Ar samples of Szulc et al. (2006) indicated by stars. The stratigraphic position
814 of Ojha et al.'s (2009) section was set at the base of the long normal chron located at the bottom of the section.
815 The red line in (f) shows the best-ranked minimum cost correlation that we used to calculate depositional ages **(h)**
816 **Cosmogenic burial ages plot against their depositional ages derived from the minimum cost magnetostratigraphic**
817 **correlation. The uncertainties in depositional ages are calculated using the minimum and the maximum ages**
818 **derived from the 10,000 magnetostratigraphic correlations.**

819

820 **Fig. 5:** Temporal evolution of the geochemical records measured along the Surai section. **The Na/Si and Al/Si**
821 **ratio can be interpreted as proxies for weathering intensity and sorting, respectively (Lupker et al., 2011). The**
822 **⁸⁷Sr/⁸⁶Sr and ε_{Nd} isotopic ratio can be compared to the isotopic composition of the main Himalayan geological unit**
823 **to track back potential changes in rock sources (e.g. France-Lanord et al., 1993). Depositional ages were calculated**
824 **using the best-ranked minimum cost correlation (red line in Fig. 4). Blue and purple stars indicate values measured**
825 **in modern sands of the Rapti River upstream (Rap-Cos1) and downstream (Nag9) of the Siwalik Hills, respectively**
826 **(see Fig. 2 for locations). Yellow and orange stars indicate values measured in modern sand of the Karnali river**
827 **downstream of the Siwalik and at the MBT, respectively (Lupker et al., 2012b).**

828

829 **Fig. 6:** Geochemical evidence of sediment transport in the floodplain. (a) Na/Si versus Al/Si plot for the Surai data
830 and several Himalayan rivers. We interpret that a first cycle of transport ('1') deposited newly weathered sediments
831 and that a second cycle ('2') recycled a large proportion of previously weathered Siwalik sediments. (b) Sr vs. ε_{Nd}

832 plot of the Surai data compared to the values expected for the three main Himalayan units (Deniel et al., 1987;
833 France-Lanord et al., 1993; Morin, 2015; Parrish and Hodges, 1996; Robinson et al., 2001).

834

835 **Fig. 7:** Schematic diagram of the proposed evolution of the drainage area. Red arrows indicate finite displacement
836 across the basin. The yellow star indicates the palaeo- (left and center) and present (right) position of the Surai
837 section.

838

839 **Fig. 8:** Temporal evolution of reconstructed ^{10}Be palaeoconcentrations and derived palaeodenudation rates in the
840 Surai Khola. Palaeoconcentrations (left) are corrected for radioactive decay and exposure in the floodplain (see
841 text). Denudation rates were calculated assuming that the sediments of the Surai section were deposited by a
842 Karnali-type trans-Himalayan river prior to ~ 3.5 Ma (middle), and by a Rapti-type midland-draining river since
843 ~ 3.5 Ma (right). The grey arrows in the right plot indicate recycling of Siwaliks sandstone; the true denudation
844 rates in the Rapti basin upstream of the Siwaliks are necessarily lower than the plotted data. All denudation rates
845 were calculated using ages derived from the minimum-cost magnetostratigraphic correlation (Fig. 4f). The
846 uncertainties on denudation rates were calculated using a Monte-Carlo approach similar to Puchol et al. (2017).
847 Denudation rates calculated based on the minimum and maximum ages from the 10,000 stochastic
848 magnetostratigraphic correlations are shown in Supplementary Fig. B. **Brown, yellow, blue and red stars indicate**
849 **denudation rates derived from the analysis of modern samples collected and analysed by Lupker et al. (2012) or**
850 **in this study (RapCOS1 and 2), respectively.**

851

852 **Fig. 9:** Depositional lag times of detrital AFT (blue circles), ZFT (red circles), and Ar-Ar ages (black dots)
853 measured along the Surai section (Bernet et al., 2006; Szulc et al., 2006; van der Beek et al., 2006). The ZFT data
854 correspond to the moving peak age. The depositional ages were calculated using the minimum-cost correlation
855 (red line in Fig. 4f). The continuous black line is the 1:1 line where the thermochronological ages equal the
856 depositional ages (i.e., a lag time of zero). Dashed lines are the lag-time contours for every 2 Ma.

857

858 **Fig. 10:** The modelled impact of recycling of Siwalik sediments on the observed ^{10}Be cosmogenic concentrations.
859 (a) Schematic diagram explaining the sediment-mixing model used to constrain the impact of reworking. **The**
860 **model calculates the ^{10}Be concentrations downstream of the Siwalik (N_{out}) assuming (1) a steady denudation rates**
861 **of ~ 0.3 mm/a in the basin upstream of the MBT, (2) a denudation of the Siwalik of 0.9 mm/a to balance the uplift**
862 **rates due to tectonics and (3) an inherited ^{10}Be concentration of denuded Siwaliks similar to the concentration**
863 **measured for 6-3 Ma old sediments ($(\sim 17 \pm 6) \times 10^3$ at g^{-1}) (b) Curves of the expected mean ^{10}Be concentrations**
864 **for sediments exported directly from the Siwalik Hills (blue, N_{Siw}) sediments at the outlet of the entire basin (red,**
865 **N_{out}), including reworked Siwalik sediments. We assume that folding, denudation, and sediment reworking in the**
866 **Siwaliks began at ~ 3 Ma. The red circles show the corrected cosmogenic concentrations measured in the upper**
867 **Surai section (3–0 Ma) (see Table 1).**

868

869 Tables

870 **Table 1:** In situ ^{10}Be and ^{26}Al cosmogenic data and associated denudation rates **with their uncertainties given at**
871 **1σ .** Depositional ages were calculated using the minimum-cost correlation (red line, Fig. 4f); the maximum and

872 minimum ages derived from the 10,000 correlations calculated using the DTW algorithm are also indicated. $^{10}\text{Be}_p$
873 are palaeoconcentrations at the time of deposition, i.e., corrected for radioactive decay and transport in the
874 floodplain. d.l.: under detection limit.

875

876 **Table 2:** Palaeomagnetic results. N, normal polarity; R, reverse polarity; Trans., transitional direction; Unst.,
877 unstable demagnetization; GC, great circle. Values in italics are the mean values used for remanent directions that
878 defined great-circle paths, but nonetheless provided an unambiguous polarity.

879

880

881

Tables

Table 1: In situ ^{10}Be and ^{26}Al cosmogenic data and associated denudation rates (ε). Depositional ages were calculated using the minimum-cost correlation (red line, Fig. 4f); the maximum and minimum ages derived from the 10,000 correlations calculated using the DTW algorithm are also indicated. $^{10}\text{Be}_p$ are palaeoconcentrations at the time of deposition, i.e., corrected for radioactive decay and transport in the floodplain.

Sample	Latitude °	Longitude °	Thickness m	Age Ma	Min. Age Ma	Max. Age Ma	^{10}Be $\times 10^3$ at g^{-1}	^{26}Al $\times 10^3$ at g^{-1}	$^{26}\text{Al}/^{10}\text{Be}$ age Ma	$^{10}\text{Be}_p$ $\times 10^3$ at g^{-1}	ε mm a $^{-1}$	Basin
Sandstone												
Cos1	27.7685	82.8378	2461	5.7	5.7	5.7	1.1±0.4			18.4±7	1.5±0.85/0.46	Karnali
Cos2	27.7702	82.8343	2279	5.2	5.2	5.2	2.3±0.6	d.l.		29.8±9.8	0.92±0.48/0.27	Karnali
Cos4	27.7740	82.8355	1920	4.3	4.3	4.3	1±0.5			6.9±4.9	3.89±2.75/1.45	Karnali
Cos8	27.7770	82.8351	1629	3.6	3.5	3.9	3.3±0.4	d.l.		18.6±3.4	1.4±0.48/0.3	Karnali
Cos10	27.7762	82.8189	1606	3.6	3.5	3.8	2.3±0.6			12.4±4.4	2.21±1.12/0.62	Karnali
Cos13	27.7785	82.8067	1313	2.9	2.8	3.4	1.6±0.6			4.9±3.6	1.59±1.11/0.59	Rapti
Cos14	27.7802	82.8057	1146	2.5	2.5	3.3	3.4±0.7			10.3±3.6	0.76±0.36/0.21	Rapti
Cos16	27.7816	82.8041	1106	2.5	2.4	3.3	3±0.4	d.l.		8.6±2.2	0.89±0.34/0.21	Rapti
Cos19	27.7841	82.8021	889	2.2	2.0	3.2	4.8±0.6	15.9±10.9	1.7±1.4	12.6±2.8	0.59±0.21/0.13	Rapti
Cos21	27.7842	82.7999	813	2.1	1.7	3.1	4.8±0.9	16.3±10.6	1.7±1.4	12.3±3.6	0.62±0.26/0.15	Rapti
Cos26	27.7865	82.8002	594	1.7	0.9	2.4	4.6±1	23.8±12.6	0.7±1.3	9±3.5	0.86±0.41/0.23	Rapti
Cos27	27.7876	82.8010	524	1.5	0.9	2.2	3.1±0.6			5.1±2	1.53±0.7/0.4	Rapti
Cos29	27.7884	82.7939	219	1.0	0.5	1.4	4.3±0.6			5.6±1.7	1.36±0.52/0.31	Rapti
Cos32	27.7914	82.7903	0	0.6	0.3	0.9	5.2±1			5.7±2.5	1.37±0.64/0.36	Rapti
Quartzite pebbles												
Cos18	27.7841	82.8021	889	2.2	2.0	3.2	9±0.8	21.6±13.9	2.4±1.4			
Cos20	27.7842	82.7999	813	2.1	1.7	3.1	3.9±0.7	20.6±6.6	0.6±0.8			
Cos25	27.7865	82.8002	594	1.7	0.9	2.4	3.4±0.8	d.l.				
River bed												
RAP-COS 1	27.8386	82.7628					20.2±1.5	69.1±19.4	1.5±0.7		0.36±0.03/0.03	Rapti
RAP-COS 2	27.995	82.8218					21.9±1.6	63±11.7	1.8±0.4		0.33±0.03/0.03	Rapti

Table 2: Palaeomagnetic results. N, normal polarity; R, reverse polarity; Trans., transitional direction; Unst., unstable demagnetization; GC, great circle. Values in italics are the mean values used for remanent directions that defined great-circle paths, but nonetheless provided an unambiguous polarity.

Sample	Lat. (°)	Long. (°)	Thickness (m)	Interpretation	D_g (°)	I_g (°)	D_s (°)	I_s (°)	α_{95} (°)
SU-PM 38	27.7914	82.7903	5 242.4	N	352.9	49.5	-11.7	0.2	6.8
SU-PM 37	27.7889	82.7909	5 056.2	Unst.	-	-	-	-	-
SU-PM 36	27.7889	82.7913	5 041.2	Trans.	232.8	19.1	254.6	25.1	6.5
SU-PM 35	27.7885	82.7934	5 030.3	Trans.	11.4	12.5	15.9	-29.9	6
SU-PM 34	27.7884	82.7939	5 023.2	Unst.	-	-	-	-	-
SU-PM 33	27.7877	82.7952	4 975.7	Trans.	6.6	38	0.9	-8.3	12.2
SU-PM 32	27.7871	82.7949	4 937.7	GC	-	-	-	-	-
SU-PM 30	27.7887	82.8007	4 802.6	GC	-	-	-	-	-
SU-PM 28	27.7876	82.8010	4 718.0	R	140	-80.2	156.1	-30.7	6.5
SU-PM 27	27.7875	82.8006	4 707.0	R	171.3	-53.8	166.7	-4.3	7
SU-PM 26	27.7870	82.7995	4 691.0	GC-R	-	-	<i>178.6</i>	<i>-23.2</i>	<i>4.4</i>
SU-PM 25	27.7869	82.8000	4 674.0	GC-R	-	-	<i>178.6</i>	<i>-23.2</i>	<i>4.4</i>
SU-PM 24	27.7868	82.8002	4 668.0	R	135.5	-65.1	149.5	-16.8	2.3
SU-PM 23	27.7865	82.8002	4 648.0	Trans.	17.1	31	11.8	-11.2	9.1
SU-PM 22	27.7863	82.8010	4 603.0	Unst.	-	-	-	-	-
SU-PM 21	27.7861	82.8013	4 586.0	R	151.3	-64.6	156.2	-14.9	16.7
SU-PM 20	27.7860	82.8012	4 577.0	GC-N			<i>-1</i>	<i>12.2</i>	<i>3.7</i>
SU-PM 19	27.7861	82.8016	4 561.0	N	302.4	57.4	-39.7	12.4	2.4
SU-PM 18	27.7855	82.8019	4 521.0	R	234.7	-75.7	176.9	-34.9	6.5
SU-PM 17	27.7854	82.8017	4 517.0	R	59	-79.8	146.7	-41.2	6.1
SU-PM 16	27.7854	82.8019	4 511.0	GC-R			<i>178.6</i>	<i>-23.2</i>	<i>4.4</i>
SU-PM 15	27.7855	82.8020	4 502.0	R	357.4	-68.7	147.5	-59.8	0.4
SU-PM 14	27.7854	82.8022	4 487.0	Unst.	-	-	-	-	-
SU-PM 13	27.7853	82.8022	4 473.1	R	176.8	-65	167.3	-15.8	4.5
SU-PM 12	27.7850	82.8021	4 450.1	GC-R	-	-	<i>178.6</i>	<i>-23.2</i>	<i>4.4</i>
SU-PM 11a	27.7850	82.8021	4 440.1	R	358.5	-81	155.7	-48.5	12.7
SU-PM 10	27.7842	82.7999	4 429.9	GC-R	-	-	<i>178.6</i>	<i>-23.2</i>	<i>4.4</i>
SU-PM 9	27.7841	82.7998	4 418.4	GC	-	-	-	-	-
SU-PM 8	27.7841	82.7998	4 400.9	N	18.2	57.3	0	12.4	5.3
SU-PM 7	27.7841	82.8000	4 393.7	N	346.8	51.6	-15.8	1.8	8.4
SU-PM 6	27.7841	82.8021	1	Unst.	-	-	-	-	-
SU-PM5	27.7836	82.8039	4310.50	GC	-	-	-	-	-
SU-PM 4	27.7833	82.8040	4267.30	GC-R	-	-	<i>178.6</i>	<i>-23.2</i>	<i>4.4</i>
SU-PM 3	27.7816	82.8041	4246.09	N	84.8	6.6	74.5	15.5	18.9
SU-PM2	27.7812	82.8045	4136.42	GC	-	-	-	-	-
SU-PM1	27.7802	82.8057	4096.48	R	151.1	-59.8	155.5	-10.1	3.7

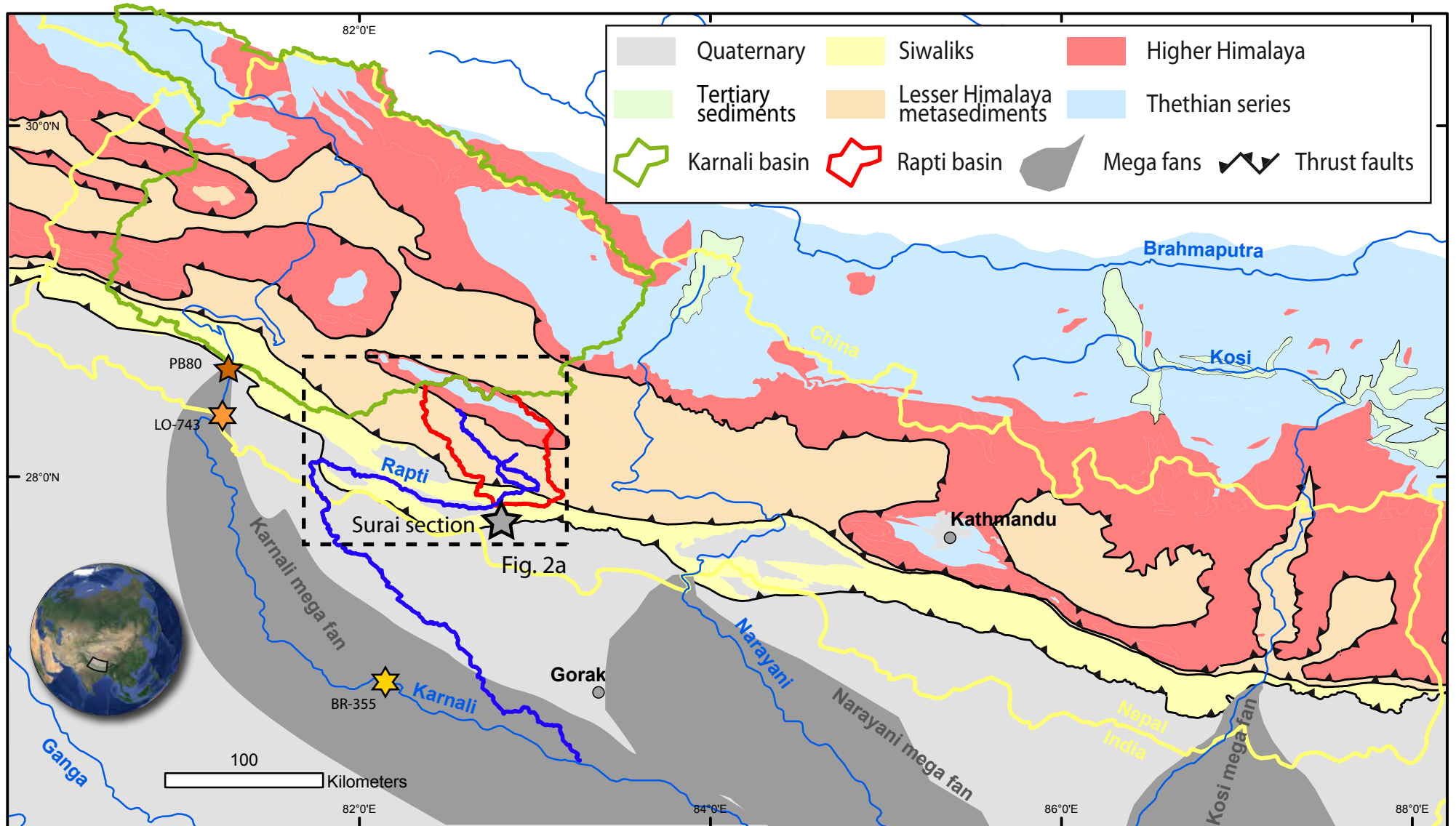


Fig. 1

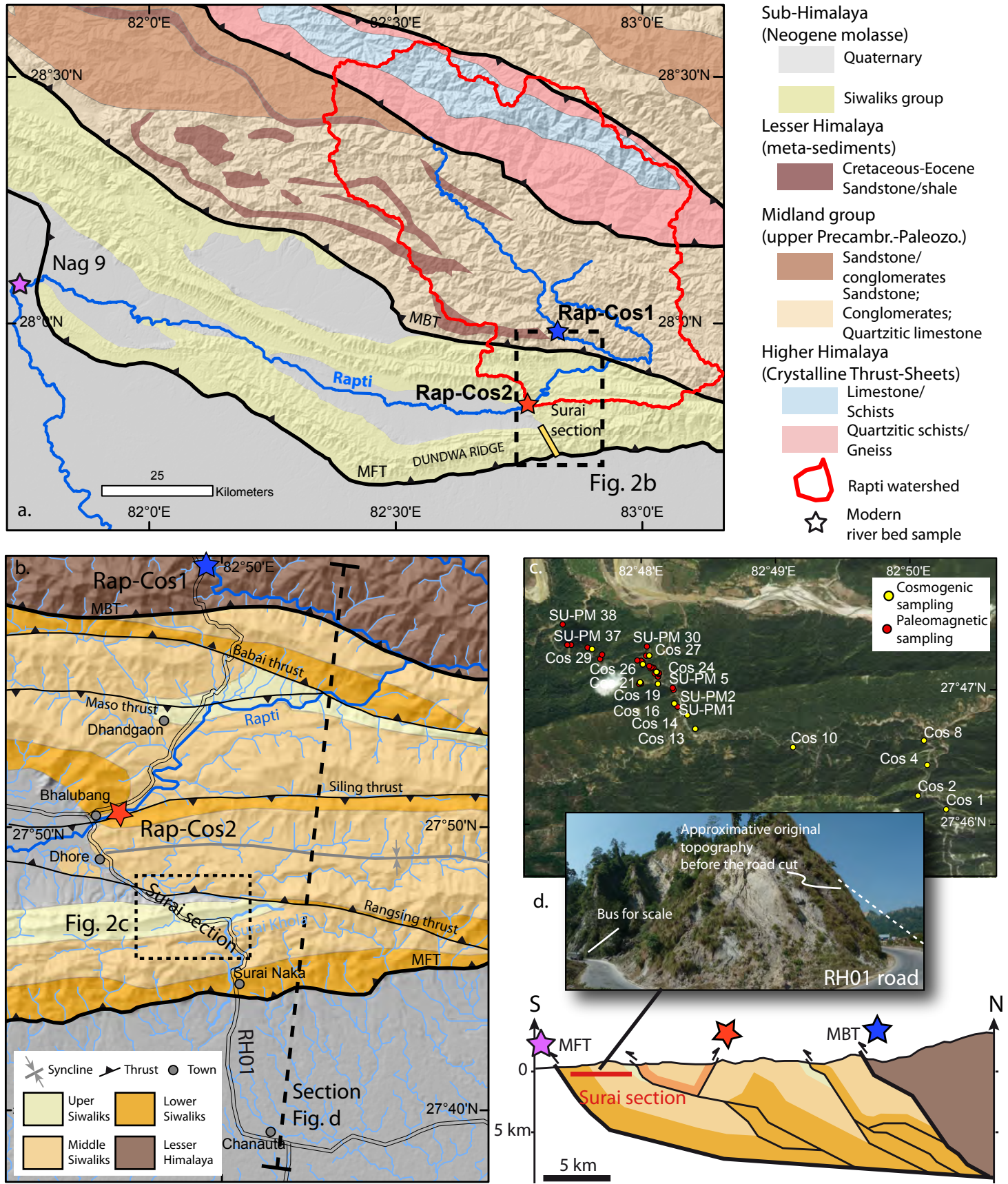


Fig. 2

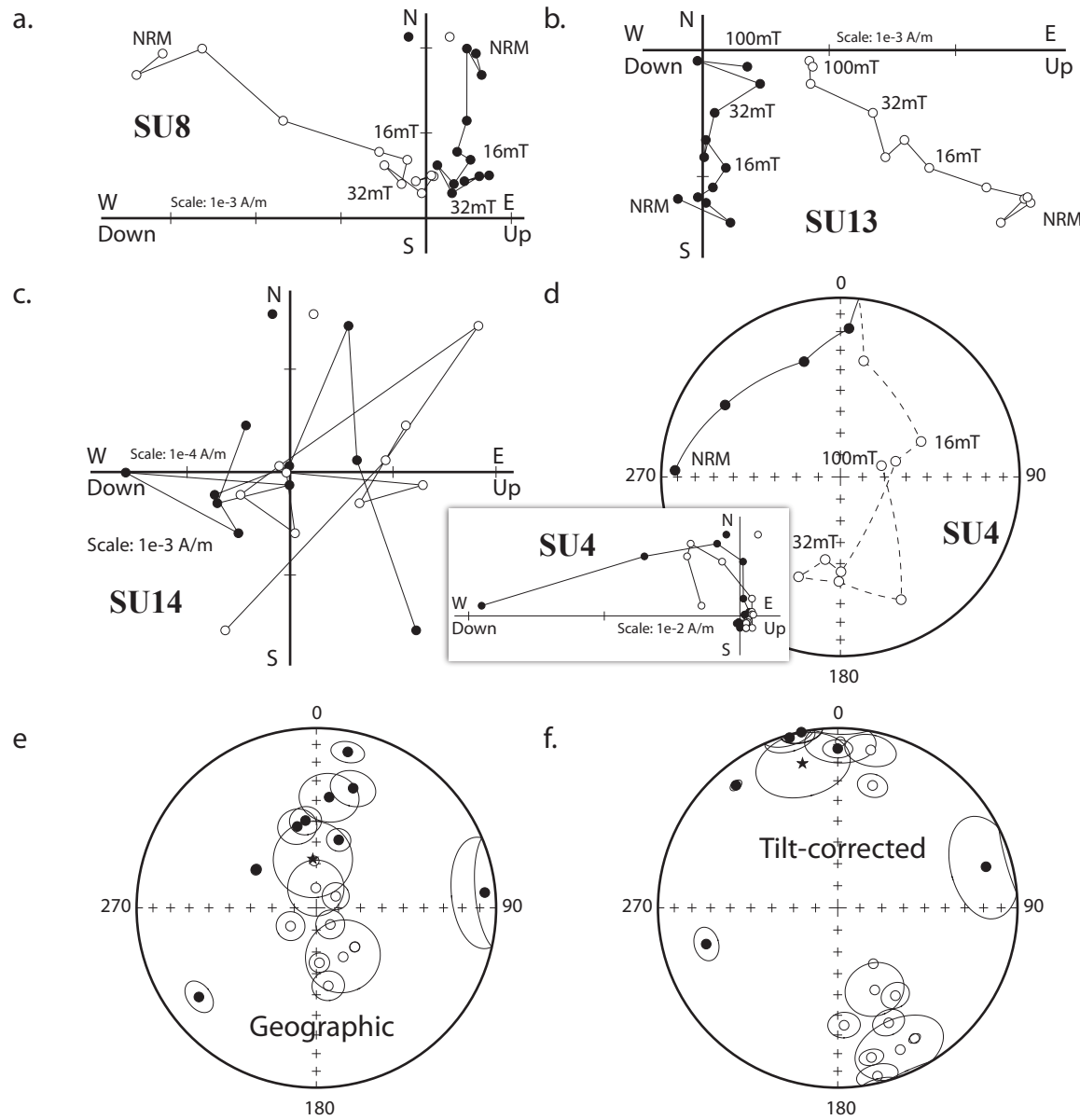


Fig. 3

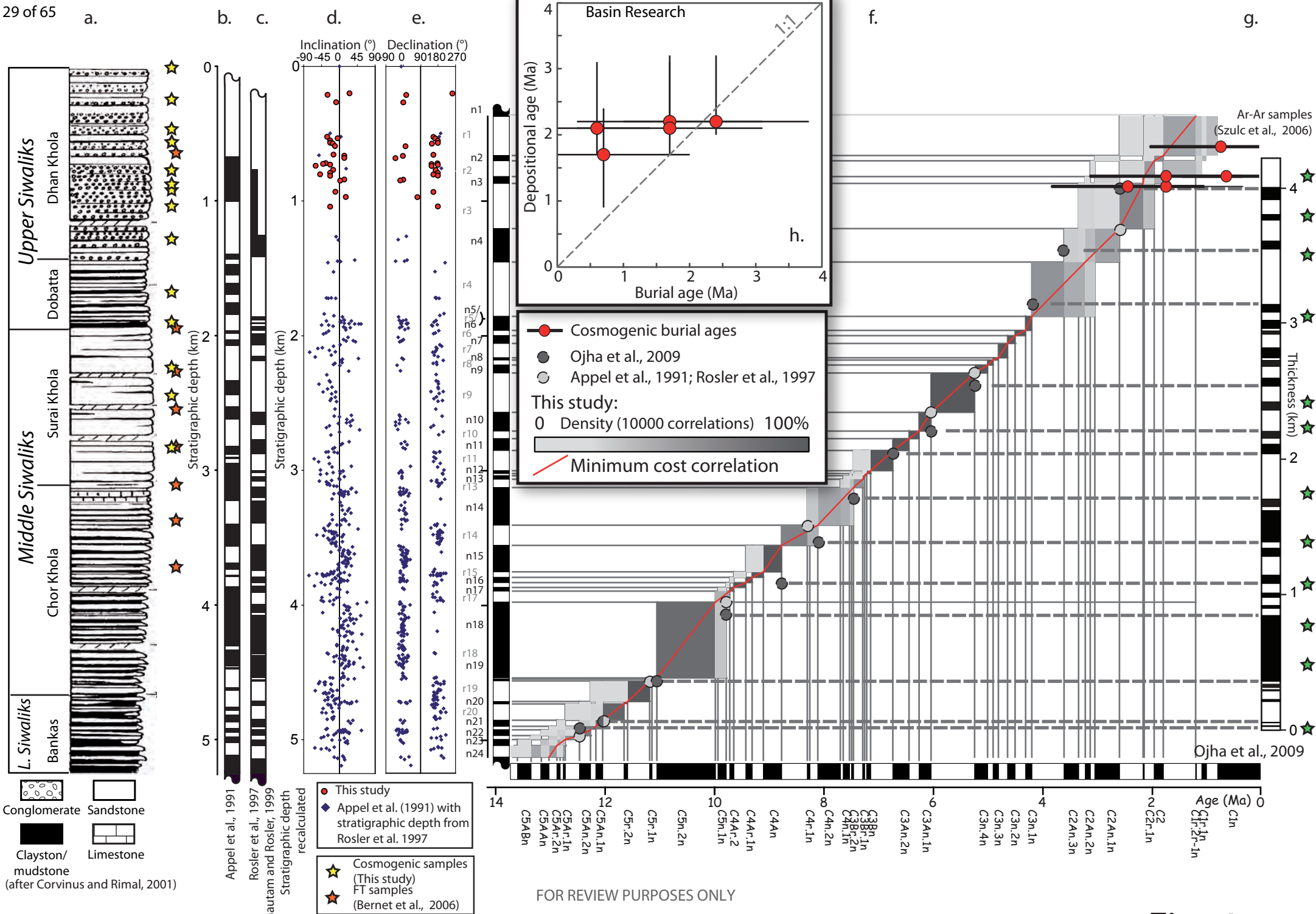


Fig. 4

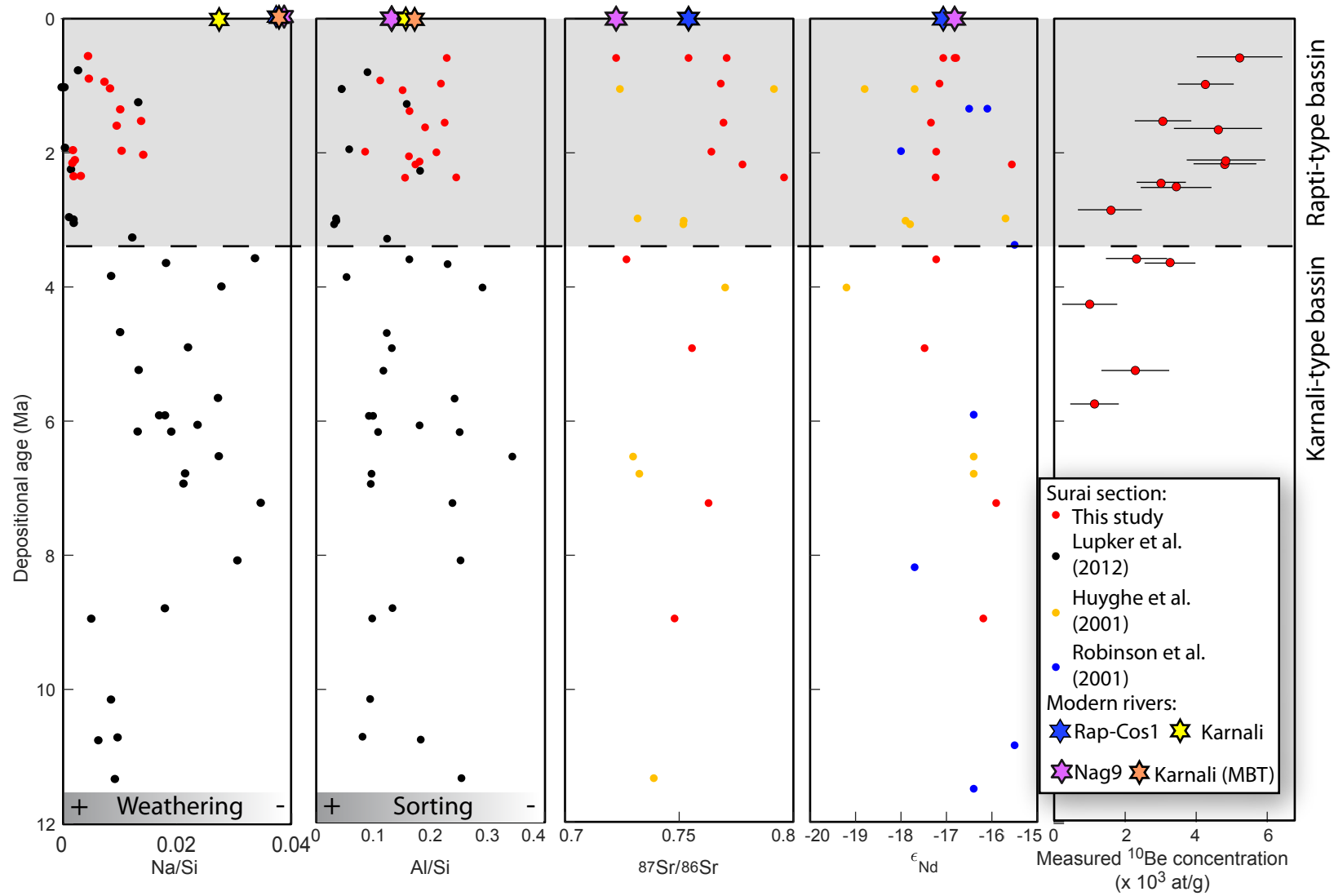


Fig. 5

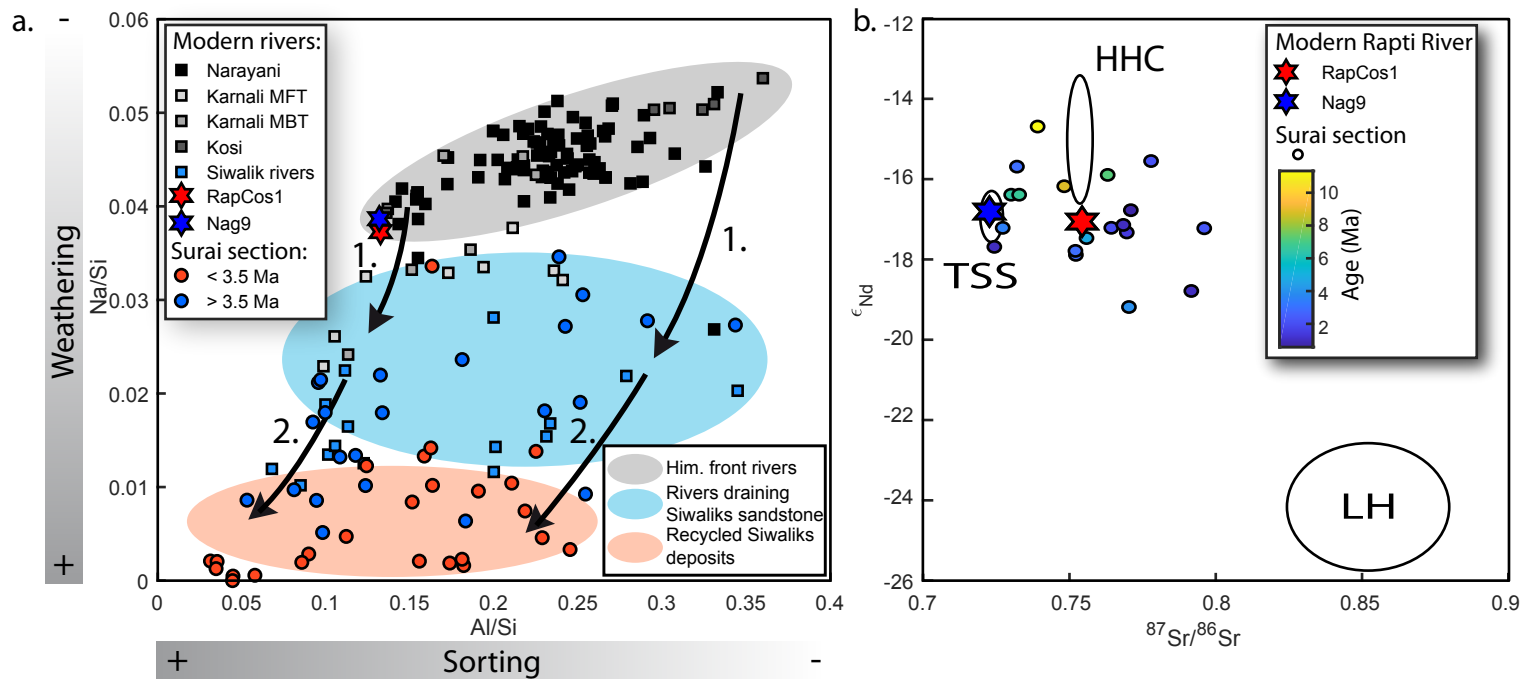
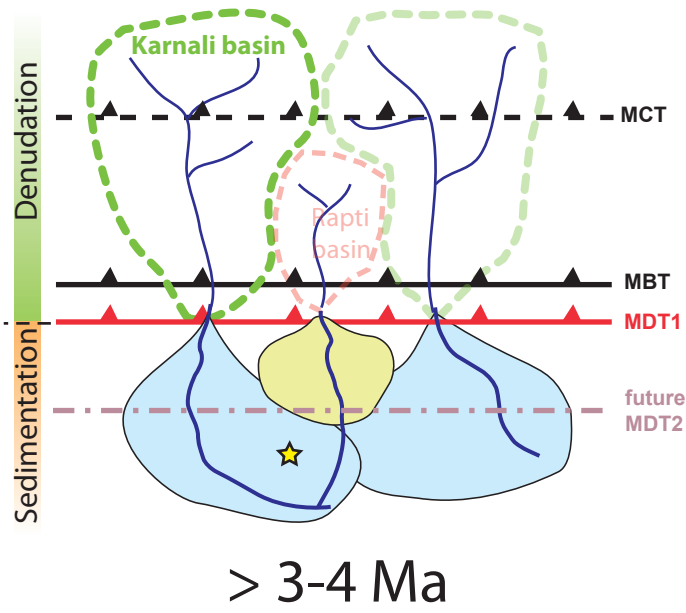
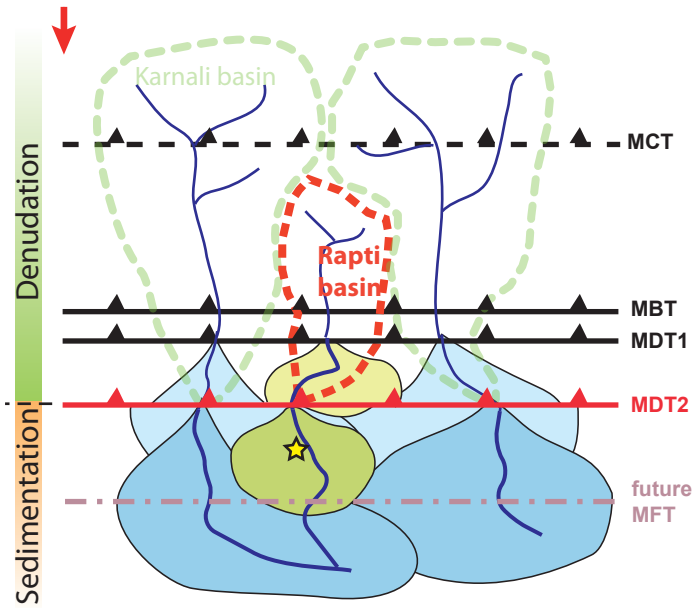


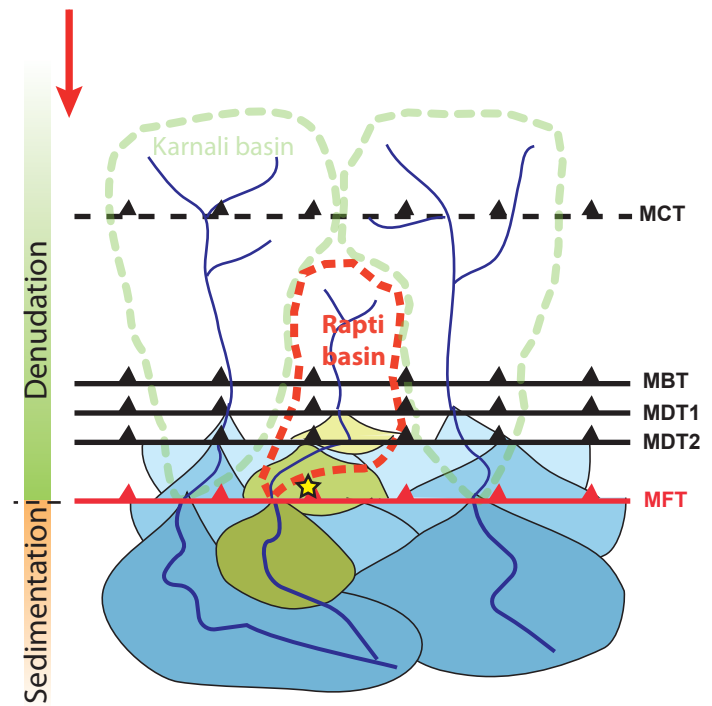
Fig. 6



> 3-4 Ma



1-3 Ma



present

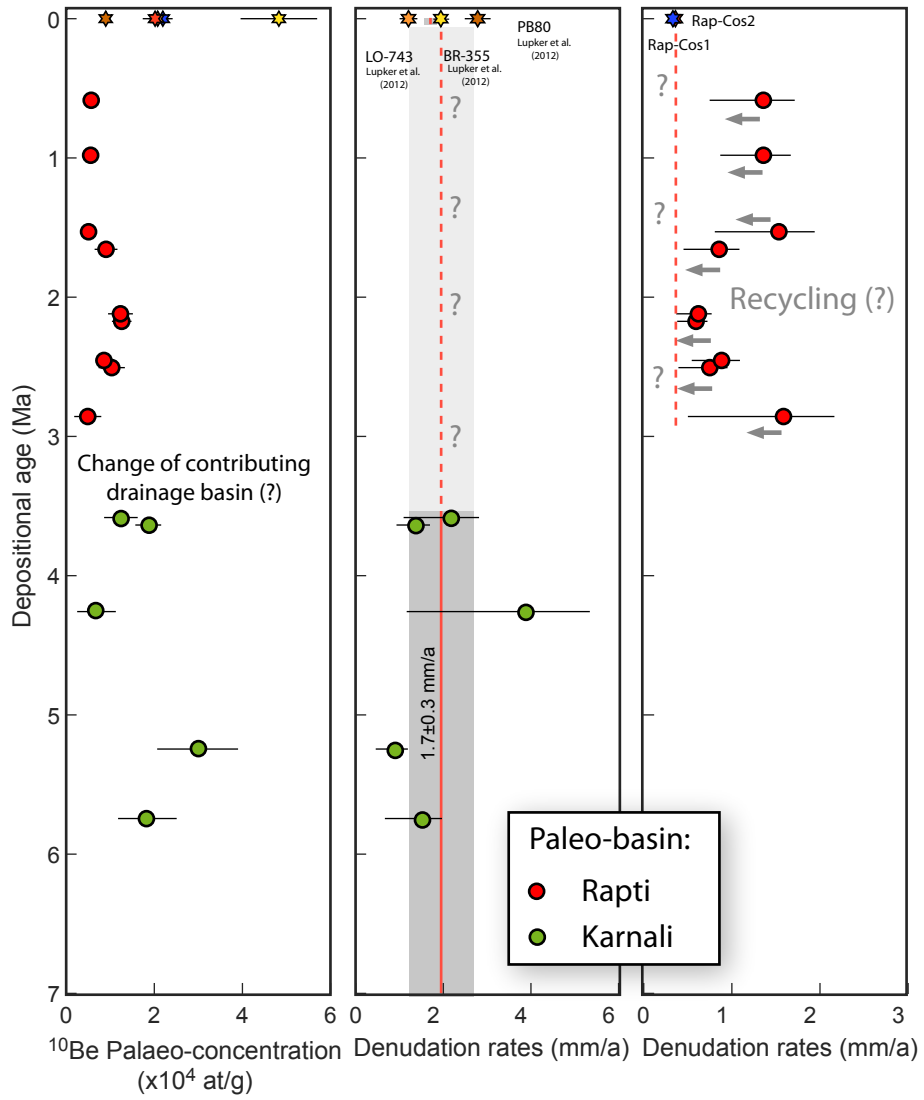


Fig. 8

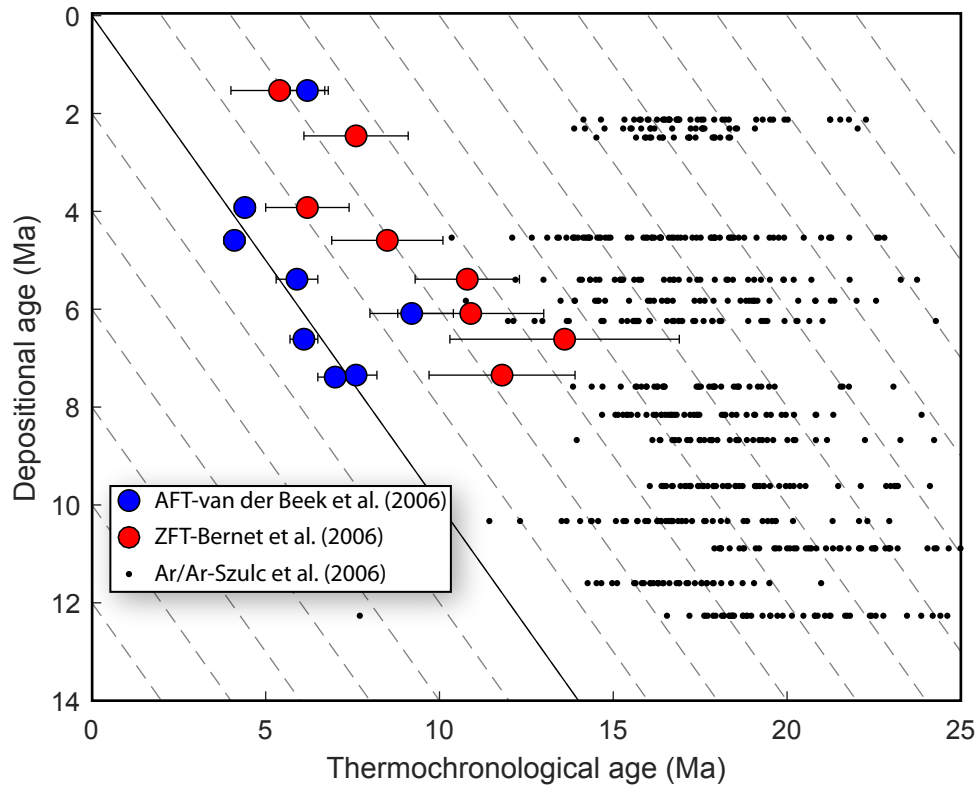


Fig. 9

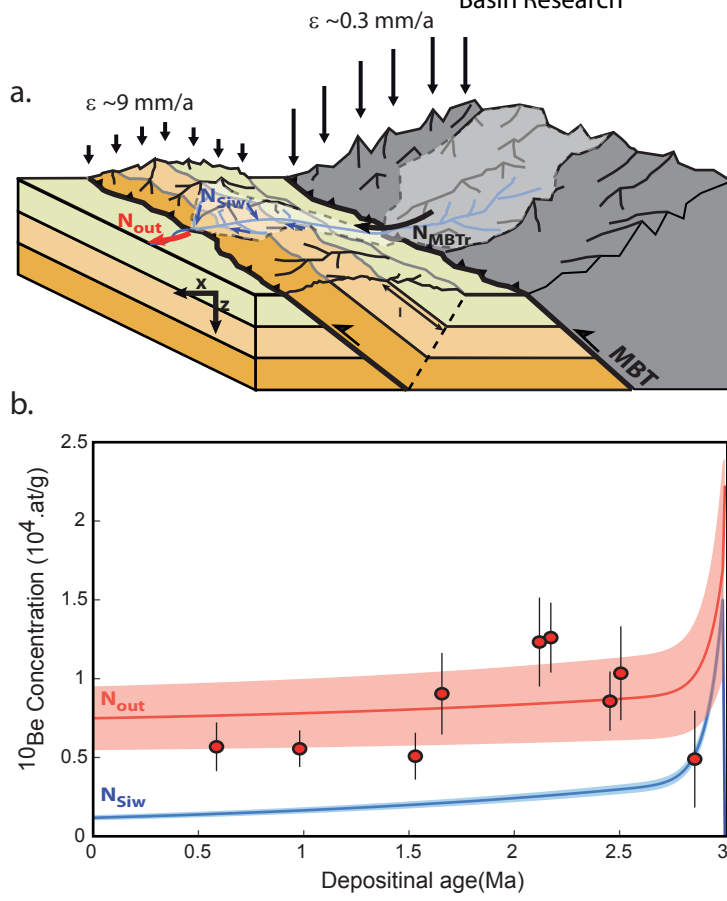


Fig. 10

Supplementary information

“A 6 Ma record of palaeodenudation in the central Himalayas from in situ cosmogenic ^{10}Be in the Surai section”

*Julien Charreau, Jérôme Lavé, Christian France-Lanord, Nicolas Puchol, Pierre-Henri Blard, Raphaël Pik, and
ASTER Team*

Magnetostratigraphic analyses

Sample treatments and results of the demagnetization

Bedding attitude, sun correction, and GPS coordinates were measured at each sampling location. The thickness between two successive sites was directly measured with a tape measure when possible or estimated from the GPS coordinates and elevations. All sampling sites were stratigraphically replaced according to the stratigraphic depths of Rosler et al. (1997), which were recalculated from Appel et al. (1991). To isolate the characteristic and primary magnetic remanence directions, the 36 samples were treated using 10–12 steps of alternating field (AF) demagnetization in the palaeomagnetism laboratory of the Ludwig-Maximilians University of Munich. The remanence at each step was measured using a three-axis DC superconducting quantum interference devices (Squid). From the 36 analysed samples, 19 showed a component that decayed toward the origin and could be isolated (Fig. 3a and b, Table 2). We identified a relatively stable component that usually decayed to the origin under a medium field (10–30 mT), suggesting that the remanent directions were carried by a magnetic phase of relatively low coercivity. Isothermal remanent magnetization (IRM) acquisition and thermal demagnetization of an IRM suggested the presence of hematite, magnetite, and goethite (Appel et al., 1991). As hematite dominated the magnetic remanence in most of the section, magnetite prevails in the upper part (Appel et al., 1991) and is likely the main magnetic carrier in our samples. A second component was sometimes identified under lower fields (<10 mT), and the magnetic directions were often unstable under higher fields (>30 mT). The AF demagnetization was probably unsuccessful in separating the hard magnetic hematite and goethite remanences (Appel et al., 1991), although they represent second order magnetic phases in this upper part of the section.

Among these 19 samples, 10, 5, and 4 were identified as reverse, normal, and transitional directions, respectively (Table 2). Assuming a Fisherian distribution, the overall mean direction in geographic (g) and stratigraphic (s) coordinates (Fig. 3e and f) is $D_g = 348.2^\circ$, $I_g = 57.7^\circ$, $k_g = 22.4$, $a_{95g} = 2.5^\circ$, and $D_s = 356.^\circ$, $I_s = 25.9^\circ$, $k_s = 21.3$, $a_{95s} = 2.5^\circ$, respectively, where D is declination, I is inclination, k is the precision parameter, and a_{95} is the 95% confidence radius. The 5 samples interpreted to have transitional directions had either E-W declination or negative inclination and a declination consistent with normal polarity. The 10 reverse directions are more reliable, having demagnetization diagrams of better quality yielding a mean of $D_g = 154.1^\circ$, $I_g = -79.9^\circ$, $k_g = 16.5$, $a_{95g} = 13.1$, and $D_s = 158.8^\circ$, $I_s = -29.9^\circ$, $k_s = 16.5$, $a_{95s} = 13.1^\circ$. This mean direction is consistent with the mean value of the reverse directions that we found in the lower part of the section ($D_s = 178.6^\circ$, $I_s = -23.2^\circ$, $k_s = 4.9$, $a_{95s} = 4.4^\circ$), strengthening our conclusion that our new data and interpretations are reliable despite the large uncertainties in the magnetic directions and the poor quality of the demagnetization.

Of the remaining samples, 5 showed unstable directions that were useless for establishing the polarity column (Fig. 3c) and 12 had remanence trajectories spread out about great circles (Fig. 3d) that never reached stable endpoints but had clear polarities.

Correlations using all polarity intervals

When all polarity intervals are considered, all 10,000 correlations found using the DTW algorithm and the numerical approach developed by Lallier et al. (2013) date the section to between ~14–13 and ~2–1 Ma (Fig. A). However, in that case, the correlations result in sharply reduced (by a factor of 2–3) accumulation rates above ~2 km stratigraphic depth (Fig. A).

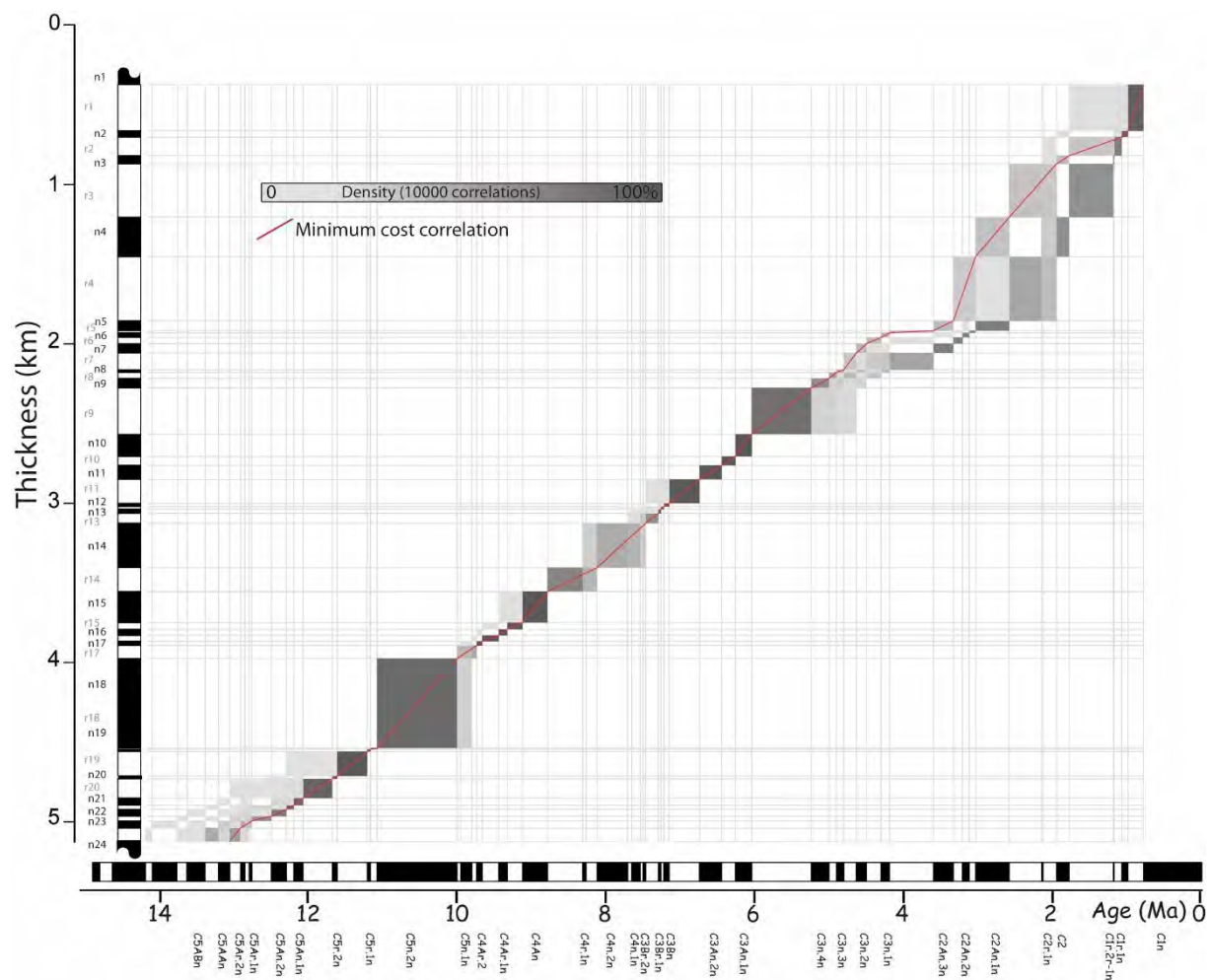


Fig. A: Revised magnetostratigraphic column of the Surai section correlated to the reference scale using the DTW algorithm of Lallier et al. (2013) considering all polarity intervals, including the reverse interval r5 that was omitted in the final magnetostratigraphic correlation (see main text and Fig. 4).

Indeed, the eight reversals identified around 2 km depth (n5 to n9) are sandwiched between two long reverse polarity intervals (r4 and r9) and cannot be easily correlated to a sequence of the reference scale with the same number of reversals. Yet, the automatic method used here assumes that all reference chrons are known; otherwise,

infinite correlations would be found. Therefore, the studied magnetostratigraphic column cannot have more polarity intervals than chrons in the reference scale (Lallier et al., 2013) and the accumulation rate must rapidly vary to account for this high number of reversals between n5 and n9. Because the Neogene has been intensively studied, especially using cyclostratigraphy, we consider the reference scale to be complete during this period (Ogg, 2012). No major unconformity, erosional surfaces, nor strong sedimentary facies changes that could explain such a rapid drop in the accumulation rates have been identified at this depth. Therefore, an alternative solution must be considered. Local faults may yield stratigraphic repetition of the series. Furthermore, in such a fluvial environment, due to channel incision, stratigraphic horizons could have been deposited at greater depths than the previous older level. Both these effects could be hidden by surface slope deposits and/or discontinuous outcrops. If unidentified during field sampling, a given horizon could be sampled several times, yielding an extra polarity interval unknown in the reference scale. Hence, we performed a second test where the reverse interval r5, which relies on only two samples of the same polarity, was arbitrarily omitted during the calculations. This correlation is used in the final magnetostratigraphic column in the main text.

Major and trace elements and Sr/Nd isotopic analyses

Major and trace element concentrations in bulk aliquots of ~100 mg of sediment were analysed after lithium metaborate fusion (Carignan et al., 2001) by inductively coupled plasma atomic emission spectroscopy and inductively coupled plasma mass spectrometry, respectively, at the Service d'Analyses des Roches et des Minéraux (SARM-CRPG, Nancy, France). The Sr and Nd isotopic compositions of 12 new samples (ten palaeosediments along the Surai section and the two river bed samples, Rap-Cos1 and Nag9) were analysed to complete the published dataset (Huyghe et al., 2001; Robinson et al., 2001). Sr and Nd isotopic compositions were analysed at the CRPG on decarbonated fractions of sediment following the technique described in Galy et al. (1999) and Pierson-Wickman et al. (2001).

Cosmogenic analyses and sample treatment

All cosmogenic samples collected for palaeodenudation reconstructions were crushed and sieved to isolate the 200–800 μm fraction. The quartz fraction was first enriched through successive magnetic separations and flotation. To eliminate all other mineral phases, the quartz-enriched fraction underwent successive leachings in a mixture of $4/5 \text{ H}_2\text{SiF}_6 + 1/5 \text{ HCl}$. The pure quartz fraction then underwent three partial dissolutions in concentrated HF, removing 30% of the quartz to eliminate atmospheric ^{10}Be (Brown et al., 1991). The purified quartz fraction was then spiked with 100 μL of a carrier solution with 3,025 ppm ^9Be before being completely dissolved in HF. These house-made carrier solutions were prepared from phenakite minerals and have extremely low $^{10}\text{Be}/^9\text{Be}$ ratios ($<4 \times 10^{-16}$), which is particularly important to accurately analyse old samples with very low ^{10}Be concentrations. Following subsequent purification on chromatographic columns by anion exchange, cation exchange, alkaline precipitations, and oxidation, the purified beryllium and aluminum oxides were analysed at the French national accelerator mass spectrometer facility ASTER (Accelerator for Earth Sciences, Environment and Risks, CEREGE laboratory, Aix en Provence, France). $^{10}\text{Be}/^9\text{Be}$ ratios measured at ASTER are normalized using the SRM 4325 NIST reference material, considering an assigned reference $^{10}\text{Be}/^9\text{Be}$ ratio of $(2.79 \pm 0.03) \times 10^{-11}$. This

standardization is equivalent to 07KNSTD within rounding errors. Total analytical $^{10}\text{Be}/^{26}\text{Al}$ blank ratios were, on average, $(1.5 \pm 0.8) \times 10^{-15}$ for these series (see Table E, below).

For ^{26}Al measurements, in samples that contained insufficient natural ^{27}Al for isotopic dilution to measure ^{26}Al , we added a commercial 1,000 ppm ^{27}Al standard (typically between 700 and 1,000 μL). $^{26}\text{Al}/^{27}\text{Al}$ ratios were calibrated against ASTER's in-house standard SM-Al-11, assuming a $^{26}\text{Al}/^{27}\text{Al}$ value of $(7.40 \pm 0.06) \times 10^{-12}$. Analytical $^{26}\text{Al}/^{27}\text{Al}$ blank ratios were, on average, $(3 \pm 4) \times 10^{-15}$ for these series (see Table D, below). Natural ^{27}Al concentrations were measured by inductively coupled plasma optical emission spectrometry in the dissolved samples (after evaporation and substitution of fluorides by HNO_3) at the Service National d'Analyse des Roches et Minéraux (SARM, CRPG, Nancy, France).

Cosmogenic production rates

We used the Basinga GIS tool and a cell-by-cell approach to compute the average production rates of the modern drainage basins using the Lal-Stone scheme, the ERA40 atmosphere, and the following scaling factors at sea level and high latitude (Charreau et al., 2019): $S_n = 4.11 \pm 0.19$ at $\text{g}^{-1} \text{yr}^{-1}$ (worldwide average value from CREp; Martin et al., 2017), $S_{\text{us}} = 0.011 \pm 0.001$ at $\text{g}^{-1} \text{yr}^{-1}$, and $S_{\text{ur}} = 0.039 \pm 0.004$ at $\text{g}^{-1} \text{yr}^{-1}$ (Braucher et al., 2011). These computed basin-averaged production rates exclude a correction for glacial and snow shielding. In the Himalaya snow shielding affects modern production rates by in average less than 5% (Scherler et al., 2014). Similarly, a correction of the modern glacial extent derived from the GLIMS database (Raup et al., 2007) yield to cosmogenic production rates $\sim 11\%$ lower than the value we used. These corrections are quite low when compared to the other uncertainties associated to the method. However, neglecting the snow and glacial shielding implies that the cosmogenic production rates and, hence, the denudation rates, must be considered as maximum values.

Cosmogenic burial ages

Burial ages t_{burial} were calculated using the Matlab code of Blard et al. (2019), which solves the following equation:

$$\frac{P_1}{N_1} e^{-\lambda_1 \cdot t_{\text{burial}}} - \frac{P_2}{N_2} e^{-\lambda_2 \cdot t_{\text{burial}}} = \frac{\lambda_1 - \lambda_2}{f}$$

where N_1 and N_2 and λ_1 and λ_2 are two radiocative nuclides (here the pair ^{10}Be - ^{26}Al) and their decay constants, respectively. f is the spatial production rate scaling factor and is dimensionless. It is calculated according to the Stone model (Stone, 2000) and using the standard atmosphere. This equation has no analytical solution and is therefore numerically solved to determine t_{burial} . Hence, the code uses a Monte Carlo approach: 5000 random rows are performed assuming ^{10}Be and ^{26}Al follow normal distributions (N_{10}, σ_{10}) and (N_{26}, σ_{26}) , N_{10} and N_{26} (at.g^{-1}) being the measured concentrations in one sample and σ_{10} and σ_{26} (at.g^{-1}) their corresponding one sigma analytical uncertainties (see Table 1 and E).

Model of floodplain transport

We calculate the average floodplain concentration at distance x down the valley axis, $N_{fp}(x)$, from the sediment concentration within the channel, $N_c(x)$, according to (eq. 17 in Lauer & Willenbring, 2010):

$$N_f(x) = \frac{1}{\left(\frac{1}{t_{ex}} + \frac{1}{t_{agg}} + \lambda\right)} \left(\frac{N_c(0)}{t_{prod}} + \left(\frac{1}{t_{ex}} + \frac{1}{t_{agg}}\right) N_c(x) \right) \quad (2)$$

where, N_c and N_f are the ^{10}Be concentrations in sediments in the channel and the top surface of the floodplain, respectively, and t_{agg} , t_{ex} , and t_{prod} are the characteristic timescales of sediment sequestration due to aggradation, lateral exchange, and ^{10}Be production, respectively. These timescales depend on the distance to the range front x , channel depth, sinuosity, migration rate, and mean sediment flux at the range outlet, subsidence rate, the width of the alluvial fan or floodplain, and the fractions of the analysed granulometric classes in the transported and deposited sediments. We add to this model deep (mostly muogenic) ^{10}Be production (following Braucher et al., 2011) once the sediment is buried below the depth of re-erosion, H , of the active channel at bankfull discharge, so that:

$$N_{fp}(x) \cong N_f(x) - N_c(0) + \sum_{j=1,3} \frac{P_j^{fp} A_j}{\sigma \rho_s} e^{-\frac{H \rho_s}{A_j}} \quad (3)$$

where σ is the mean aggradation/subsidence rate in the floodplain, ρ_s the sediment density, and P_j^{fp} the ^{10}Be production rate (including nucleogenic and muogenic contributions) at the floodplain elevation, but neglecting radioactive decay in the initial equation (valid as long as $\frac{\sigma \rho_s}{A_j} \gg \lambda$).

This model produces a mean gain in ^{10}Be concentration in the plain as function of the distance to the mountain front. To apply this correction to our different samples, we must estimate their palaeoposition relative to the mountain front at the time of deposition for x . This was calculated considering the sediment depositional ages and by equating the mountain wedge-front migration rate to the mean facies migration rate of $15 \pm 5 \text{ mm yr}^{-1}$ for the central part of the Indo-Gangetic Plain (Lyon-Caen and Molnar, 1985).

The geomorphic characteristics and parameters describing rivers draining through the Ganga plain and used as input parameters in the model are reported in Supplementary Table A. We considered two end-members: sediment transport and deposition either by a trans-Himalayan river such as the present Karnali River or by a medium-sized river such as the present Rapti River, which only drains the frontal and southern part (or Midlands) of the Himalayan range. The parameters used were derived from published studies (as for sediment flux), measurements made in similar Himalayan rivers (as for grain size fractions, see Supplementary Table A), or from our own measurements (including sedimentation rates derived from our magnetostratigraphic results and lateral channel migration rates based on channel locations determined from over two decades of satellite imagery available on Google Earth). As our objective was only to provide an order-of-magnitude estimate of the ^{10}Be concentrations accumulated during sediment transport in the plain, we made several simplifications. As applied in Lauer and Willenbring (2010) or Lupker et al. (2012), we assumed that model parameters such as the depth and aggradation rate of the active floodplain and the sinuosity and lateral migration rate of the channel are spatially uniform from the mountain front to the plain outlet; downstream sediment fining was also omitted. Finally, to estimate the palaeolocation x , we only considered depositional ages derived from the best-ranked magnetostratigraphic correlation and not the full range of possible depositional ages provided by the DTW correlations.

Model of frontal fold erosion and sediment recycling

The ^{10}Be concentrations measured at the outlet of a drainage basin downstream of the Siwaliks can be calculated as:

$$N_{out} = \frac{r \varepsilon_{MBT_r} N_{MBT_r} + \varepsilon_{Siw} N_{Siw}}{r \varepsilon_{MBT_r} + \varepsilon_{Siw}} \quad (\text{S1})$$

where N_{MBT_r} refers to the mean in situ ^{10}Be cosmogenic concentration measured in sediments (at g^{-1}) downstream of the MBT at the time the Siwalik sediments are reworked and ε_{MBT_r} is the associated denudation rate (mm yr^{-1}) of the same drainage basin. Similarly, N_{Siw} and ε_{Siw} correspond to the mean ^{10}Be concentrations and denudation rates measured in a basin that drains only the Siwalik Hills, respectively. r is the ratio between the area of the drainage basin located upstream of the MBT and the area of the part draining the Siwaliks (Fig. 9).

Assuming that the Siwaliks sediments are deformed and exhumed in the piedmont via a simple kink-band fault-bend fold (Fig. 11), the ^{10}Be concentrations of the reworked Siwaliks sediments that are eroded at any point x along the structure can be estimated as:

$$N_{Siw}(x) = (N_{MBT_p} + N_{FP}(x + tR_{fm}))e^{-\lambda t} + \sum_j \frac{\bar{P}_j}{j \varepsilon_{Siw} \rho_r \frac{A_j}{A_j}} \quad (\text{S2})$$

where N_{MBT_p} is the ^{10}Be palaeoconcentration of sediments shed from the palaeo-drainage basin located upstream of the MBT at the time of Siwaliks deposition (Fig. 9). N_{FP} was estimated with the model presented in the main text. R_{fm} is the facies migration rate. t is the time since fold initiation t_{fi} during which the reworked sediments were deposited, which can be estimated as:

$$t = t_{fi} + \frac{t_{fi} R_s \sin \theta}{A} \quad (\text{S3})$$

where θ is the dip angle of the thrust fault, R_s (mm yr^{-1}) the slip rate across the frontal fault, and A the sediment accumulation rate in the Siwaliks basin. Over enough time, the cumulative slip across the fold may be greater than the distance along the bedding $l(x)$ between the point at the surface and the hinge of the fold. In that case, $t = t_{fi} + \frac{l(x)}{A}$. The mean ^{10}Be concentration N_{Siw} shed from the Siwalik hills can then be estimated by averaging all individual concentrations $n_{Siw}(x)$ eroded at all locations x along the fold. Hurtrez et al. (1999) applied mass balance across the Siwalik structures and found that the average elevation represents only 10% of surface uplift, suggesting that the landscape of the Siwalik Hills has rapidly reached a dynamic equilibrium and that tectonic uplift is balanced by erosion. In our simple fault-bend fold model, the erosion rate of the Siwaliks (ε_{Siw}) is therefore equal to $0.9 R_s \sin \theta$.

Consistent with modern ^{10}Be concentrations measured in the Rapti basin upstream of the Siwaliks at the MBT, we assumed a steady denudation rates of $\sim 0.3 \text{ mm/a}$ and hence that the upstream sediments shed from the Rapti basin during Siwaliks reworking (N_{MBT_r}) have a steady ^{10}Be concentration of $(\sim 20 \pm 2) \times 10^3$ at g^{-1} . The mean ^{10}Be concentration of the reworked Siwalik sediments (N_{MBT_p}) can be inferred from the concentration measured in 7–3 Ma sediments in the Surai section, corrected for radioactive decay and transport in the floodplain $(\sim 17 \pm 6) \times 10^3$ at g^{-1} . The slip rate across the frontal structure and the facies migration rate are assumed to be $21 \pm 2 \text{ mm a}^{-1}$ (Lavé and Avouac, 2000) and $15 \pm 5 \text{ mm a}^{-1}$ (Lyon-Caen and Molnar, 1985), respectively. We assumed a classic fault dip angle of $30 \pm 10^\circ$. The ratio between the areas of the two parts of the basin is assumed equal to 11.3, consistent with the modern setting.

Supplementary figures and tables

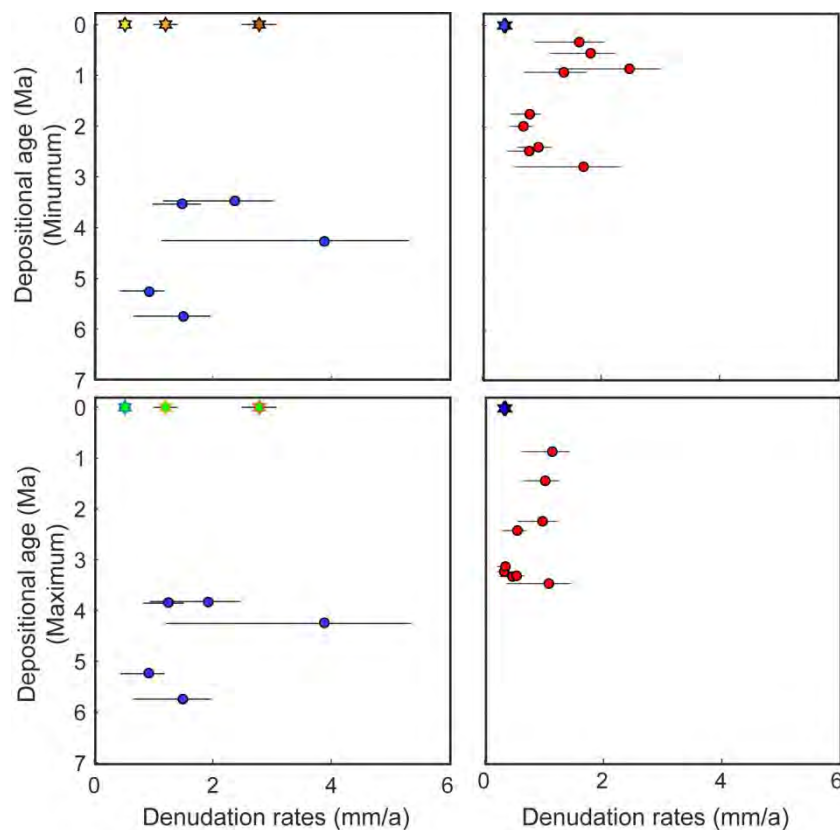


Fig. B: Palaeodenudation rates in the palaeo-Karnali (left) and palaeo-Rapti basins (right) calculated using either the minimum (top) or maximum ages (bottom) derived from the 10,000 magnetostratigraphic correlations.

Table A – parameters used in the paleo-denudation rates calculation with their uncertainties and associated references. These uncertainties were used in the Monte-Carlo simulation to estimate the uncertainties on the final paleo-denudation rates.

Parameter and unit	Symbol	Value	1 σ	References / comments
Sea Level High Latitude ^{10}Be production rate ($\text{at.g}^{-1}\text{.yr}^{-1}$) used in Basinga (Charreau et al., 2019)				
Neutrons	-	4.13	0.198	Martin et al. (2017)
Slow muons	-	0.01	0.002	(Braucher et al., 2011), corrected from (Braucher et al., 2003)
Fast muons	-	0.04	0.007	(Braucher et al., 2011), corrected from (Braucher et al., 2003)
Cosmogenic production rates of the Rapti basin ($\text{at.g}^{-1}\text{.yr}^{-1}$)				
Neutrons	P_n	10.96	0.526	Calculated using Basinga (Charreau et al. (2019)
Slow muons	$P_{\mu s}$	0.02	0.004	Calculated using Basinga (Charreau et al. (2019)
Fast muons	$P_{\mu f}$	0.05	0.010	Calculated using Basinga (Charreau et al. (2019)
Cosmogenic production rates of the Karnali basin ($\text{at.g}^{-1}\text{.yr}^{-1}$)				
Neutrons	P_n	35.18	1.689	Calculated using Basinga (Charreau et al. (2019)
Slow muons	$P_{\mu s}$	0.039	0.008	Calculated using Basinga (Charreau et al. (2019)
Fast muons	$P_{\mu f}$	0.064	0.013	Calculated using Basinga (Charreau et al. (2019)
Attenuation length (g. cm^{-2})				
Neutrons	Λ_n	160	10	(Lal, 1991)

Fast muons	Λ_{fmuons}	4320	950	(Braucher <i>et al.</i> , 2003; Braucher <i>et al.</i> , 2011; Heisinger <i>et al.</i> , 2002b)
Slow muons	Λ_{smuons}	1510	100	(Braucher <i>et al.</i> , 2003; Braucher <i>et al.</i> , 2011; Heisinger <i>et al.</i> , 2002a)
Others parameters				
^{10}Be decay constant (yr^{-1})	λ	4.997×10^{-7}	0.043×10^{-7}	(Chmeleff <i>et al.</i> , 2010; Korschinek <i>et al.</i> , 2010)
depositional age	t (Ma)	Magentostratigray	0.5	This study
denisty of denuded rocks	ρ_r	2.65	0.5	
Concentration accumulated during transport	N_{fp}	See Table C	See table C	This study

Table B: Parameters for the flood plain transfer model.

Parameters	Karnali River	Rapti River	References*
	min/max	min/max	
Sediment density	1.9/1.9	1.9/1.9	
Floodplain width (km)	50/90	15/30	3
Bankfull channel depth (m)	5/8	4/6	5
Fraction of sediment load (200–800 μm fraction) in the floodplain	0.3/0.4	0.3/0.5	6
Fraction of sediment load (200–800 μm fraction) in the channel	0.15/0.25	0.15/0.25	7
Total sediment flux at the range outlet (Mt a^{-1})	100/200	20/30	1, 2
Channel lateral migration rate (m a^{-1})	50/100	50/250	3
Sediment aggradation rate in the floodplain (mm a^{-1})	0.4/0.8	0.4/0.8	4
River sinuosity	1.3/1.7	1.5/2	3

*1, Lupker *et al.* (2012); 2, Sinha *et al.* (2005); 3, this study (sinuosity includes the average obliquity of the river relative to the radial direction); 4, Gautam and Rossler (1999); 5, Jain and Sinha (1987); 6, Dubille and Lavé (2015); 7, Morin *et al.* (2018).

Table C: ^{10}Be contributions in the floodplain calculated using the floodplain transfer model.

Samples	Age (Ma)	Karnali	Rapti River
		River	River
		$\times 10^3 \text{ at g}^{-1}$	$\times 10^3 \text{ at g}^{-1}$
Cos1	5.7	1.6 \pm 0.3	2.4 \pm 0.7
Cos2	5.2	1.6 \pm 0.3	2.3 \pm 0.7
Cos4	4.3	1.5 \pm 0.3	2.1 \pm 0.5
Cos8	3.6	1.5 \pm 0.3	1.9 \pm 0.5
Cos10	3.6	1.5 \pm 0.3	1.9 \pm 0.5
Cos13	2.9	1.4 \pm 0.3	1.8 \pm 0.4

Cos14	2.5	1.4±0.3	1.7±0.4
Cos16	2.5	1.4±0.3	1.7±0.4
Cos19	2.2	1.4±0.2	1.6±0.3
Cos21	2.1	1.4±0.2	1.6±0.3
Cos26	1.7	1.3±0.2	1.5±0.3
Cos27	1.5	1.3±0.2	1.5±0.3
Cos29	1	1.3±0.2	1.4±0.3
Cos32	0.6	1.2±0.2	1.3±0.2

Table D: Geochemical data. Please see the excel sheet available online.

Table E1: Raw in situ cosmogenic ^{10}Be and ^{26}Al data of the samples.

Sample	Total counts ^{10}Be	$^{10}\text{Be}/^9\text{Be}$ (10^{-15})	Mass of quartz (g)	Added ^9Be ($\times 10^{19}\text{at}$)	^{10}Be ($\times 10^3 \text{ at/g}$)	Total counts ^{26}Al	$^{26}\text{Al}/^{27}\text{Al}$ ($\times 10^{-15}$)	Mass of quartz (g)	Total ^{27}Al (Carrier and natural) ($\times 10^{18}\text{at/g}$)	^{26}Al ($\times 10^4\text{at/g}$)
<u>Sandstone</u>										
Cos1	16	8.7±2.4	272.4	4.1	1.1±0.4					
Cos2	13	60±16.7	528.7	2.0	2.3±0.6	0				
Cos4	5	14.9±6.7	284.7	2.1	1±0.5					
Cos8	61	86.9±11.2	533.9	2.1	3.3±0.4	2	1.4±1	533.9	4.40	0.2±1.1
Cos10	17	25.2±6.1	214.2	2.1	2.3±0.6					
Cos13	7	19.4±7.3	235.1	2.1	1.6±0.6					
Cos14	24	20±4.1	112.8	2.1	3.4±0.7					
Cos16	47	70.2±10.3	473.9	2.1	3±0.4	0				
Cos19	62	30.4±3.9	125.4	2.0	4.8±0.6	6	4.8±2	125.4	3.70	1.6±1.1
Cos21	33	77.3±13.5	322.9	2.1	4.8±0.9	9	4.7±1.6	322.9	3.90	1.6±1.1
Cos26	27	53.6±11.1	229.3	2.1	4.6±1	11	6.4±2.2	229.3	4.10	2.4±1.3
Cos27	36	19.4±3.3	122.6	2.1	3.1±0.6					
Cos29	65	26.4±3.3	121.8	2.1	4.3±0.6					
Cos32	46	23.7±4.2	88.9	2.1	5.2±1					
<u>Quartzite pebbles</u>										
Cos18	150	90.7±7.5	201.6191	2.1	9±0.8	8	5.7±2	201.6	4.60	2.2±1.4
Cos20	35	59.8±10.1	300.7331	2.1	3.9±0.7	19	10.9±2.5	300.7	2.00	2.1±0.7
Cos25	19	73.7±16.9	433.9689	2.1	3.4±0.8	3	1.7±1	434.0	2.80	0.3±0.7
<u>River bed</u>		0±0								
RAP-COS 1	217	76.2±5.2	75.8601	2.1	20.2±1.5	26	26.7±6.9	75.9	2.70	6.9±1.9
RAP-COS 2	194	102.8±7.5	95.7462	2.1	21.9±1.6	42	25.4±3.9	95.7	2.60	6.3±1.2

Table E2: Blank values for cosmogenic analyses.

Serie	Total counts ^{10}Be	$^{10}\text{Be}/^9\text{Be}$ ($\times 10^{-15}$)	Samples
1	8	2.4±0.8	8,18,Rap1,Rap2
2	4	2.1±1.1	20,25 et 26
3	7	1.9±0.7	21
4	5	0.9±0.4	2,16,19,25
5	13	1.1±0.3	1,4,10,13,14, 27,29,32

Serie	Total counts ^{26}Al	$^{26}\text{Al}/^{27}\text{Al}$ ($\times 10^{-15}$)	Samples
1	1	0.5±0.5	2,16,19,20,21,25,26
2	2	1±0.7	Rap1,Rap2,8,18

Table F – Depth of the polarity intervals of the Surai magnetostratigraphic column

Depth (m)	Polarity interval
372	R1
662	N2
701	R2
818	N3
869	R3
1204	N4
1452	R4
1855	N5
1959	R6
1998	N7
2056	R7
2162	N8
2179	R8
2216	N9
2275	R9
2567	N10
2706	R10
2762	N11
2850	R11
3000	N12
3021	R12
3037	N13
3063	R13
3125	N14
3404	R14
3554	N15
3750	R15
3791	N16
3830	R16

3866	N17
3893	R17
3975	N18
4537	R18
4545	N19
4559	R19
4712	N20
4730	R20
4851	N21
4896	R21
4922	N22
4965	R22
4994	N23
5039	R23
5124	N24

Bibliography

- Appel, E., Rosler, W., Corvinus, G., Munchen, O., 1991. Magnetostratigraphy of the Miocene-Pleistocene Surai Khola Siwaliks in West Nepal 191–198.
- Bernet, M., van der Beek, P., Pik, R., Huyghe, P., Mugnier, J.L., Labrin, E., Szulc, A., 2006. Miocene to Recent exhumation of the central Himalaya determined from combined detrital zircon fission-track and U/Pb analysis of Siwalik sediments, western Nepal. *Basin Res.* 18, 393–412. <https://doi.org/10.1111/j.1365-2117.2006.00303.x>
- Braucher, R., Merchel, S., Borgomano, J., Bourlès, D.L., 2011. Production of cosmogenic radionuclides at great depth : A multi element approach. *Earth Planet. Sci. Lett.* <https://doi.org/10.1016/j.epsl.2011.06.036>
- Brown, E.T., Edmond, J.M., Raisbeck, G.M., Yiou, F., Kurz, M.D., Brook, E.J., 1991. Examination of surface exposure ages of Antarctic moraines using in situ produced ¹⁰Be And ²⁶Al. *Geochim. Cosmochim. Acta* 55, 2269–2283.
- Carignan, J., Hild, P., Mevelle, G., Morel, J., Yeghicheyan, D., 2001. Routine Analyses of Trace Elements in Geological Samples using Flow Injection and Low Pressure On-Line Liquid Chromatography Coupled to ICP-MS: A Study of Geochemical Reference Materials BR, DR-N, UB-N, AN-G and GH. *Geostand. Geoanalytical Res.* 25, 187–198. <https://doi.org/10.1111/j.1751-908x.2001.tb00595.x>
- Charreau, J., Blard, P.-H., Zumaque, J., Martin, L.C.P., Delobel, T., Szafran, L., 2019. Basinga: A cell-by-cell GIS toolbox for computing basin average scaling factors, cosmogenic production rates and denudation rates. *Earth Surf. Process. Landforms* 44, 2349–2365.
- Dubille, M., Lavé, J., 2015. Rapid grain size coarsening at sandstone/conglomerate transition: Similar expression in Himalayan modern rivers and Pliocene molasse deposits. *Basin Res.* 27, 26–42. <https://doi.org/10.1111/bre.12071>
- Galy, A., France-Lanord, C., Derry, L.A., 1999. The strontium isotopic budget of Himalayan rivers in Nepal and Bangladesh. *Geochim. Cosmochim. Acta* 63, 1905–1925. [https://doi.org/10.1016/S0016-7037\(99\)00081-2](https://doi.org/10.1016/S0016-7037(99)00081-2)
- Gautam, P., Rosler, W., 1999. Depositional chronology and fabric of Siwalik group sediments in Central Nepal from magnetostratigraphy and magnetic anisotropy. *J. As* 17, 659–682.

- Hurtrez, J.-E., Lucazeau, F., Lavé, J., Avouac, J.-P., 1999. Investigation of the relationships between basin morphology, tectonic uplift, and denudation from the study of an active fold belt in the Siwalik Hills, central Nepal. *J. Geophys. Res.* 104, 12779. <https://doi.org/10.1029/1998JB900098>
- Huyghe, P., Galy, A., Mugnier, J.M., France-Lanord, C., 2001. Propagation of the thrust system and erosion in the Lesser Himalaya : Geochemical and sedimentological evidence. *Geology* 1007–1010.
- Jain, V., Sinha, R., 1987. River systems in the Gangetic plains and their comparison with the Siwaliks : A review. *Curr. Sci.* 84, 27–30.
- Lallier, F., Antoine, C., Charreau, J., Caumon, G., Ruiu, J., 2013. Management of ambiguities in magnetostratigraphic correlation. *Earth Planet. Sci. Lett.* 371–372, 26–36. <https://doi.org/10.1016/j.epsl.2013.04.019>
- Lauer, J.W., Willenbring, J., 2010. Steady state reach - scale theory for radioactive tracer concentration in a simple channel / floodplain system 115, 1–21. <https://doi.org/10.1029/2009JF001480>
- Lavé, J., Avouac, J.P., 2000. Active folding of fluvial terraces across the Siwaliks Hills, Himalayas of central Nepal. *J. Geophys. Res.* 105, 5735. <https://doi.org/10.1029/1999JB900292>
- Lupker, M., Blard, P.-H., Lavé, J., France-Lanord, C., Leanni, L., Puchol, N., Charreau, J., Bourlès, D., 2012. ¹⁰Be-derived Himalayan denudation rates and sediment budgets in the Ganga basin. *Earth Planet. Sci. Lett.* 333–334, 146–156. <https://doi.org/10.1016/j.epsl.2012.04.020>
- Lyon-Caen, H., Molnar, P., 1985. Gravity anomalies, flexure of the Indian plate and the structure, support and evolution of the Himalaya and Ganga basin. *Tectonics* 4, 513–538.
- Martin, L.C.P., Blard, P.H., Balco, G., Lavé, J., Delunel, R., Lifton, N., Laurent, V., 2017. The CREp program and the ICE-D production rate calibration database : A fully parameterizable and updated online tool to compute cosmic- ray exposure ages. *Quat. Geochronol.* 38, 25–49. <https://doi.org/10.1016/j.quageo.2016.11.006>
- Morin, G.P., Lavé, J., France-Lanord, C., Rigaudier, T., Gajurel, A.P., Sinha, R., 2018. Annual Sediment Transport Dynamics in the Narayani Basin, Central Nepal: Assessing the Impacts of Erosion Processes in the Annual Sediment Budget. *J. Geophys. Res. Earth Surf.* 123, 2341–2376. <https://doi.org/10.1029/2017JF004460>
- Ogg, J.G., 2012. Geomagnetic Polarity Time Scale, in: Gradstein, F.M. (Ed.), *The Geological Time Scale*.
- Pierson-Wickmann, A.-C., Reisberg, L., France-Lanord, C., Kudrass, H.R., 2001. Os-Sr-Nd results from sediments in the Bay of Bengal: Implications for sediment transport and the marine Os record. *Paleoceanography* 16, 435–444.
- Raup, B., Racoviteanu, A., Khalsa, S.J.S., Helm, C., Armstrong, R., Arnaud, Y., 2007. The GLIMS geospatial glacier database: a new tool for studying glacier change. *Glob. Planet. Change* 56, 101–110.
- Robinson, D.M., Decelles, P.G., Patchett, P.J., Garzzone, C.N., 2001. The kinematic evolution of the Nepalese Himalaya interpreted from Nd isotopes. *Earth Planet. Sci. Lett.* 192, 507–521.
- Rosler, W., Metzler, W., Appel, E., 1997. Neogene magnetic polarity stratigraphy of some fluvial Siwalik sections, Nepal 89–111.
- Scherler, D., Bookhagen, B., Strecker, M.R., 2014. Tectonic control on ¹⁰Be-derived erosion rates in the Garhwal Himalaya, India. *J. Geophys. Res. Earth Surf.* 119, 83–105. <https://doi.org/10.1002/2013JF002955>

- Sinha, R., Jain, V., Babu, G.P., Ghosh, S., 2005. Geomorphic characterization and diversity of the fluvial systems of the Gangetic Plains. *Geomorphology* 70, 207–225.
<https://doi.org/10.1016/j.geomorph.2005.02.006>
- Szulc, A.G., Najman, Y., Sinclair, H.D., Pringle, M., Bickle, M., Chapman, H., 2006. Tectonic evolution of the Himalaya constrained by detrital $^{40}\text{Ar}/^{39}\text{Ar}$, Sm, Nd and petrographic data from the Siwalik foreland basin succession, SW Nepal. *Basin Res.* 18, 375–391. <https://doi.org/10.1111/j.1365-2117.2006.00307.x>
- van der Beek, P., Robert, X., Mugnier, J., Bernet, M., Huyghe, P., Labrin, E., 2006. Late Miocene–Recent exhumation of the central Himalaya and recycling in the foreland basin assessed by apatite fission-track thermochronology of Siwalik sediments, Nepal. *Basin Res.* 18, 413–434. <https://doi.org/10.1111/j.1365-2117.2006.00305.x>

Table C: geochemical results. Ages were calculated following the minimum cost correlation

Sample	River	Thickness m	Coordinates		Age Ma	SiO ₂
			Lat. (°)	Lon. (°)		
<u>Present river sand</u>						
RapCos1	Rapti (MBT)		27.8386	82.7628		70.9
Nag 9	Rapti (MFT)		27.995	82.8218		74.2
NAG 18	Rapti		27.906379	82.832222		74.7
R 94-06	Joug		Unknown	Unknown		78.9
NAG 16	Sharda		28.297188	82.255254		80.3
MO 326	Surai		Unknown	Unknown		60.3
MO 322	Kwali		Unknown	Unknown		64.2
CA 10012	Rapti		27.581117	84.480417		63.5
CA 10013	Rapti		27.581117	84.480417		87.7
CA 11142	Rapti chitwan		27.563714	84.210601		68.2
CA 11145	Riu		27.541381	84.195694		86.8
MO 318	Tinau		Unknown	Unknown		66.8
MO 318 2-50	Tinau		Unknown	Unknown		67.8
PB 72	Karnala Nadi		27.074378	85.584037		58.9
PB 73	Karnala Nadi		27.074378	85.584037		81.6
PB 74	Karnala Nadi		27.074378	85.584037		80.8
NAG 13	Bheri		28.517280	81.663289		72.5
Bheri Monsoon	Bheri		28.517280	81.663289		72.1
PB 79	Karnali		28.641320	81.283239		59.0
PB 79	Karnali		28.641320	81.283239		0.0
PB 80	Karnali		28.641320	81.283239		77.8
NAG 12	Karnali		28.366639	81.201545		75.8
LO 743	Karnali		28.367250	81.195310		73.8
LO 751	Karnali		28.368930	81.203470		58.5
LO 750	Karnali		28.368930	81.203470		57.7
LO 748	Karnali		28.366957	81.201024		63.3
LO 749	Karnali		28.366957	81.201024		66.5
MO 217	Narayani		27.550000	84.055000		68.5
MO 331	Narayani		27.700417	84.418484		60.9
LO 309	Narayani		27.700417	84.418484		64.1
NAG 48	Narayani		27.700417	84.418484		67.2
PB 60	Narayani		27.700350	84.427353		52.0
PB 58	Narayani		27.700350	84.427353		52.0
PB 57	Narayani		27.700350	84.427353		56.4
PB 56	Narayani		27.700350	84.427353		58.6
PB 55	Narayani		27.700350	84.427353		60.6
PB 54	Narayani		27.700350	84.427353		62.7
LO 741	Nayayani		27.704515	84.427292		64.9
LO 757	Nayayani		27.702971	84.426606		53.3
LO 756	Nayayani		27.702971	84.426606		56.8
LO 754	Nayayani		27.702971	84.426606		59.5
LO 755	Nayayani		27.702971	84.426606		57.8
LO 758 A	Nayayani		27.702971	84.426606		52.3
LO 758 B	Nayayani		27.702971	84.426606		54.7
LO 758 C	Nayayani		27.702971	84.426606		69.4
LO 1001	Narayani		27.724883	84.427787		69.9
LO 1002	Narayani		27.699476	84.418964		53.7

CA 10008	Narayani	27.724883	84.427787	61.7
CA 10009	Narayani	27.724883	84.427787	65.3
CA 10010	Narayani	27.724883	84.427787	65.8
LO 741	Nayayani	27.704515	84.427292	64.9
CA 10010	Narayani	27.724883	84.427787	65.8
LO 1001	Narayani	27.724883	84.427787	69.9
CA 13 248 1	Narayani	Unknown	Unknown	69.0
CA 13 248 2	Narayani	Unknown	Unknown	69.3
SNG4	Narayani	27.699476	84.418964	50.2
SNG8	Narayani	27.699476	84.418964	49.0
SNG13	Narayani	27.699476	84.418964	57.8
SNG17	Narayani	27.699476	84.418964	58.6
SNG20	Narayani	27.699476	84.418964	54.0
SNG25	Narayani	27.699476	84.418964	58.9
SNG26	Narayani	27.699476	84.418964	63.5
SNG31	Narayani	27.699476	84.418964	55.4
SNG36	Narayani	27.699476	84.418964	49.9
SNG38	Narayani	27.699476	84.418964	51.0
SNG41	Narayani	27.699476	84.418964	56.7
SNG45	Narayani	27.699476	84.418964	51.9
SNG48	Narayani	27.699476	84.418964	60.3
SNG51	Narayani	27.699476	84.418964	59.0
SNG54	Narayani	27.699476	84.418964	64.4
SNG57	Narayani	27.699476	84.418964	57.0
SNG60	Narayani	27.699476	84.418964	56.4
SNG63	Narayani	27.699476	84.418964	53.7
SNG68	Narayani	27.699476	84.418964	55.0
SNG73	Narayani	27.699476	84.418964	56.7
SNG76	Narayani	27.699476	84.418964	59.9
SNG77	Narayani	27.699476	84.418964	58.8
SNG79	Narayani	27.699476	84.418964	59.9
SNG82	Narayani	27.699476	84.418964	57.4
SNG86	Narayani	27.699476	84.418964	56.9
SNG90	Narayani	27.699476	84.418964	59.8
SNG93	Narayani	27.699476	84.418964	58.6
SNG96	Narayani	27.699476	84.418964	60.5
SNG100	Narayani	27.699476	84.418964	59.3
SNG104	Narayani	27.699476	84.418964	58.2
SNG107	Narayani	27.699476	84.418964	58.6
SNG111	Narayani	27.699476	84.418964	60.0
SNG115	Narayani	27.699476	84.418964	57.2
SNG119	Narayani	27.699476	84.418964	60.6
SNG123	Narayani	27.699476	84.418964	61.0
SNG 9-34	Narayani	27.699476	84.418964	58.0
SNG 9-34	Narayani	27.699476	84.418964	58.0
SNG 35-64	Narayani	27.699476	84.418964	57.5
SNG 35-64	Narayani	27.699476	84.418964	57.5
SNG65-95	Narayani	27.699476	84.418964	59.0
SNG65-95	Narayani	27.699476	84.418964	59.0
SNG96-125	Narayani	27.699476	84.418964	60.0
SNG96-125	Narayani	27.699476	84.418964	60.0
CA 11117	Narayani	27.701733	84.423517	54.2

CA 11118	Narayani	27.701483	84.423417	59.1
CA 11116	Narayani	27.701733	84.423517	59.2
CA 11119	Narayani	27.701483	84.423317	60.8
CA 11123	Narayani	27.702383	84.424783	54.5
CA 11124	Narayani	27.702383	84.424783	59.2
CA 11122	Narayani	27.702983	84.425583	61.8
CA 11121	Narayani	27.702450	84.424700	65.8
CA 11127	Narayani	27.701467	84.423550	53.9
CA 11126	Narayani	27.701467	84.423550	57.3
CA 11125	Narayani	27.701617	84.423833	58.9
CA 11128	Narayani	27.701967	84.423967	60.6
CA 11130	Narayani	27.702383	84.423567	56.5
CA 11131	Narayani	27.702083	84.423150	56.9
CA 11129	Narayani	27.702467	84.423450	59.0
CA 13129	Narayani	27.696499	84.418039	68.7
CA 14067	Narayani	27.699476	84.418964	69.8
CA 11140	Narayani	27.455800	83.936083	67.9
CA 10001	Bheri	28.435195	81.865191	72.0
CA 10002	Bheri	28.435195	81.865191	66.0
CA 10003	Bheri	28.435195	81.865191	60.9
CA 10004	Karnali	28.783810	81.573809	69.1
CA 10005	Karnali	28.783810	81.573809	74.6
CA 10006	Karnali	28.783810	81.573809	64.0
CA 10007	Karnali	28.783810	81.573809	65.3
PB 65	Kosi	26.847022	87.151414	63.8
PB 66	Kosi	26.847022	87.151414	63.3
PB 67	Kosi	26.847022	87.151414	61.1
PB 68	Kosi	26.847022	87.151414	61.3
PB 69	Kosi	26.847022	87.151414	57.4
PB 70	Kosi	26.847022	87.151414	79.1

Surai section

SU-PM38	0	0.6	68.6
94-60	118	0.8	55.2
SU-PM37	186	0.9	82.3
SU-PM35	212	1.0	66.8
94-59A	257	1.0	81.2
94-59C	257	1.0	58.0
SU-PM33	267	1.1	70.6
94-57	381	1.3	67.9
SK98	420	1.342	
SK72	420	1.342	
SU-PM29	440	1.4	73.5
SU-PM27	535	1.6	64.1
SU-PM24	574	1.6	71.0
94-54	702	1.9	68.6
SK110	720	1.975	
SU-PM17	725	2.0	86.4
SU-PM16	731	2.0	66.9
SU-PM13	769	2.1	70.5
SU-PM9	824	2.1	74.8
SU-PM6	889	2.2	74.2

94-53	962	2.3	72.9
SU-PM2	1038	2.4	60.9
SU-PM4	1042	2.4	69.8
94-50	1362	3.0	91.9
94-48	1375	3.0	86.3
94-47	1396	3.1	93.7
94-42	1482	3.3	57.6
SK114	1520	3.372	
94-44	1609	3.6	70.7
94-41	1638	3.7	69.3
94-46	1717	3.9	89.1
94-45	1781	4.0	62.3
94-39	2091	4.7	54.1
94-38	2185	4.9	72.4
94-37	2280	5.2	64.6
94-34	2432	5.7	57.1
SK95	2520	5.905	
94-33D	2526	5.9	49.8
94-33U	2526	5.9	65.6
94-32	2586	6.1	59.0
94-31	2649	6.2	66.9
94-30	2650	6.2	33.0
94-29	2790	6.5	34.5
94-27	2869	6.8	65.0
94-26	2925	6.9	59.4
94-25	3025	7.2	63.0
94-20	3391	8.1	55.9
SK91	3420	8.179	
94-17	3564	8.8	36.1
94-16	3655	8.9	84.1
94-11	4059	10.1	82.5
94-08	4353	10.7	58.6
94-07	4376	10.7	49.3
SK79	4420	10.833	
94-04	4610	11.3	63.7
SK87	4670	11.481	

Al ₂ O ₃	Fe ₂ O ₃	MnO	MgO	CaO	Na ₂ O	K ₂ O
%						
7.9	3.7	0.1	1.7	5.9	1.3	1.8
8.2	3.5	0.1	1.2	4.1	1.5	1.8
4.9	6.4	0.2	1.1	5.1	0.7	0.9
7.6	4.5	0.2	0.8	2.4	0.7	1.5
8.4	4.5	0.1	1.0	0.3	0.5	1.9
14.3	5.3	0.1	2.3	4.8	0.7	3.2
12.6	5.3	0.1	2.0	4.2	0.5	3.1
12.6	5.3	0.1	1.9	4.2	0.6	3.1
5.1	2.2	0.1	1.0	1.3	0.5	1.7
11.6	4.6	0.1	1.9	2.2	1.0	3.1
6.3	2.4	0.1	0.5	0.5	0.5	1.3
11.3	5.1	0.1	2.2	3.9	0.4	2.6
11.6	4.7	0.1	2.5	2.4	0.5	2.9
17.2	6.3	0.1	2.5	1.8	0.6	3.8
7.0	3.3	0.1	1.0	1.1	0.6	1.7
7.2	2.8	0.0	1.1	1.1	0.6	1.9
6.9	3.1	0.0	2.2	5.6	0.8	1.7
6.1	4.1	0.1	2.3	5.7	0.7	1.5
10.6	3.9	0.1	3.5	8.7	1.1	2.7
0.0	0.0	0.0	0.0	0.0	0.0	0.0
6.5	2.6	0.1	1.4	4.6	0.9	1.6
6.8	3.5	0.1	1.8	4.5	1.0	1.5
7.7	2.7	0.0	1.5	4.7	1.2	1.8
11.7	4.4	0.1	3.5	6.8	1.0	3.2
11.8	4.3	0.1	3.3	6.8	1.0	3.1
10.4	3.8	0.1	3.0	6.1	1.1	2.8
9.8	3.4	0.1	2.5	5.4	1.1	2.6
8.4	3.3	0.1	1.8	7.8	1.5	1.9
12.3	4.6	0.1	2.2	7.3	1.6	3.0
9.4	3.5	0.0	2.1	8.2	1.4	2.2
8.8	3.4	0.1	2.1	7.6	1.3	2.1
11.9	4.4	0.1	3.1	11.7	1.4	3.2
11.9	4.4	0.1	3.1	11.6	1.4	3.2
11.0	4.0	0.1	2.7	10.8	1.5	2.9
10.7	3.7	0.1	2.5	10.1	1.5	2.8
10.6	3.6	0.1	2.4	9.4	1.5	2.7
10.2	3.6	0.1	2.3	8.8	1.5	2.6
8.5	3.5	0.1	2.0	9.1	1.4	2.0
11.2	3.8	0.1	2.2	11.9	1.4	2.8
11.3	3.8	0.1	2.1	10.9	1.4	2.8
11.0	3.6	0.1	2.0	9.4	1.5	2.7
11.2	3.7	0.1	2.1	9.7	1.4	2.8
11.1	3.9	0.1	2.3	13.0	1.2	2.7
10.8	3.7	0.1	2.2	11.4	1.3	2.7
8.4	2.5	0.0	2.5	5.9	1.4	2.0
10.2	3.5	0.1	1.9	5.3	1.6	2.3
12.2	4.6	0.1	2.5	12.4	1.3	3.2

11.4	4.5	0.1	2.6	6.0	1.3	2.9
12.4	4.2	0.0	2.5	4.4	1.6	3.4
11.1	4.0	0.1	2.3	5.4	1.6	2.9
8.5	3.5	0.1	2.0	9.1	1.4	2.0
11.1	4.0	0.1	2.3	5.4	1.6	2.9
10.2	3.5	0.1	1.9	5.3	1.6	2.3
9.0	2.9	0.0	2.1	5.9	1.5	2.1
9.1	2.8	0.0	2.1	5.7	1.5	2.1
13.9	5.1	0.1	2.6	10.5	1.1	3.4
13.9	5.1	0.1	2.3	12.0	1.3	3.4
16.2	6.1	0.1	3.1	4.1	0.8	4.6
12.7	4.5	0.1	2.4	8.0	1.5	3.1
13.1	4.9	0.1	2.4	9.9	1.3	3.2
12.2	4.8	0.1	2.8	7.5	1.3	3.0
12.2	4.3	0.1	2.2	5.9	1.5	2.9
11.7	4.2	0.1	2.4	10.6	1.4	2.9
12.2	4.5	0.1	2.3	13.1	1.3	2.9
13.3	4.9	0.1	2.6	10.4	1.2	3.4
11.3	4.2	0.1	2.6	9.8	1.3	2.8
11.5	4.2	0.1	2.4	12.0	1.2	2.8
12.2	4.3	0.1	2.4	8.0	1.4	2.9
10.9	4.0	0.1	2.3	9.4	1.4	2.6
12.8	4.5	0.1	2.2	4.8	1.4	3.1
12.6	4.6	0.1	2.4	8.8	1.3	2.9
13.5	4.8	0.1	2.2	8.6	1.2	3.1
12.1	4.5	0.1	2.6	11.2	1.3	3.0
11.9	4.3	0.1	2.2	10.9	1.4	2.9
12.0	4.5	0.1	2.6	9.2	1.3	3.1
10.3	3.7	0.1	2.3	9.6	1.4	2.5
11.3	4.2	0.1	2.5	8.9	1.4	2.8
10.9	3.9	0.1	2.4	9.0	1.4	2.8
12.5	4.6	0.1	2.4	7.8	1.3	3.0
11.5	4.3	0.1	2.4	10.1	1.2	2.8
12.0	4.3	0.1	2.6	8.2	1.4	3.0
12.8	5.4	0.1	3.1	6.6	1.4	3.0
14.8	5.2	0.1	2.6	4.2	1.3	3.7
12.8	4.7	0.1	2.8	6.9	1.4	3.2
11.8	4.4	0.1	2.8	7.9	1.4	2.9
10.8	4.1	0.1	2.6	8.5	1.3	2.6
10.8	4.0	0.1	2.6	8.2	1.4	2.7
12.0	4.6	0.1	2.7	8.4	1.3	3.0
11.3	4.3	0.1	2.6	7.2	1.5	2.8
10.7	4.1	0.1	2.5	8.0	1.3	2.6
13.1	4.9	0.1	2.5	7.1	1.3	3.2
13.1	4.9	0.1	2.5	7.1	1.3	3.2
12.1	4.4	0.1	2.4	8.9	1.3	3.0
12.1	4.4	0.1	2.4	8.9	1.3	3.0
11.7	4.3	0.1	2.4	8.8	1.3	2.9
11.7	4.3	0.1	2.4	8.8	1.3	2.9
13.2	4.8	0.1	2.6	5.9	1.3	3.3
13.2	4.8	0.1	2.6	5.9	1.3	3.3
13.5	5.1	0.1	2.9	8.3	1.3	3.4

12.2	4.6	0.1	2.6	7.5	1.4	3.0
12.2	4.7	0.1	2.6	7.6	1.4	3.0
12.0	4.4	0.1	2.4	7.2	1.4	2.9
12.3	4.6	0.1	2.6	9.4	1.3	3.1
11.3	4.3	0.1	2.5	8.6	1.4	2.7
10.9	4.1	0.1	2.4	7.7	1.4	2.7
10.6	3.7	0.1	2.1	6.1	1.5	2.6
12.0	4.7	0.1	2.8	9.4	1.2	3.0
11.8	4.4	0.1	2.4	8.9	1.3	3.0
11.4	4.3	0.1	2.4	8.6	1.3	2.9
11.0	4.1	0.1	2.3	7.7	1.4	2.7
12.3	4.5	0.1	2.5	9.2	1.4	3.2
11.2	4.4	0.1	2.6	8.9	1.3	2.8
11.5	4.5	0.1	2.6	8.8	1.3	2.9
8.2	3.0	0.0	1.7	8.1	1.4	1.9
9.4	3.3	0.1	2.0	5.4	1.5	2.3
8.9	4.6	0.2	2.0	6.7	1.2	1.6
6.9	3.9	0.1	2.6	5.3	0.9	1.7
8.5	3.8	0.1	3.6	5.8	1.1	2.2
9.6	4.4	0.1	4.4	6.3	1.1	2.6
10.0	3.2	0.0	1.7	5.7	1.6	2.4
8.7	3.1	0.1	1.6	4.6	1.5	2.0
12.2	4.5	0.1	2.5	4.6	1.4	3.1
12.0	4.3	0.1	2.3	4.5	1.5	3.0
16.0	5.7	0.1	2.6	2.0	1.7	3.9
16.3	5.8	0.1	2.7	1.8	1.6	4.0
17.1	6.2	0.1	2.9	1.8	1.6	4.3
16.8	6.0	0.1	3.0	2.0	1.6	4.2
17.5	6.0	0.1	3.8	2.2	1.6	4.5
9.1	3.0	0.1	1.3	1.8	1.6	1.9
13.1	6.4	0.1	1.4	0.6	0.2	3.0
4.2	2.0	0.1	0.6	19.3	0.1	1.1
7.7	3.2	0.1	0.7	0.2	0.2	1.8
12.2	3.9	0.1	1.3	3.8	0.3	3.0
3.0	1.1	0.0	0.6	6.2	0.0	2.2
2.2	1.2	0.0	0.9	20.0	0.0	0.7
8.9	4.0	0.0	1.0	5.5	0.3	2.3
9.0	3.8	0.0	1.3	6.1	0.5	2.3
10.1	3.4	0.0	1.1	2.6	0.4	2.5
12.1	5.0	0.1	1.6	5.1	0.5	3.0
11.3	4.2	0.0	1.4	2.9	0.3	2.9
3.3	2.2	0.0	0.5	12.4	0.0	0.9
6.2	2.4	0.0	0.8	0.4	0.1	1.6
11.8	4.2	0.1	1.9	4.1	0.4	2.8
9.6	3.5	0.0	1.4	3.7	0.5	2.5
11.3	3.6	0.0	1.1	0.4	0.1	2.4
10.8	5.3	0.1	1.0	0.4	0.1	2.2

11.1	5.2	0.0	1.6	0.3	0.1	2.1
12.5	4.4	0.1	2.8	5.8	0.1	3.2
9.1	3.7	0.1	1.5	4.5	0.1	2.2
2.7	1.7	0.0	0.2	0.1	0.1	0.6
2.6	1.3	0.0	0.3	4.3	0.1	0.7
2.5	1.5	0.0	0.2	0.2	0.1	0.6
6.0	2.5	0.2	1.7	15.2	0.4	1.4
9.7	3.8	0.0	1.8	3.8	1.2	2.4
13.4	5.2	0.0	2.1	0.7	0.6	2.6
4.0	2.4	0.0	0.4	0.3	0.4	1.0
15.2	5.1	0.0	2.9	1.4	0.9	4.0
5.6	2.2	0.1	1.4	17.8	0.3	1.3
8.0	2.8	0.0	1.5	4.9	0.8	2.0
6.4	2.2	0.1	2.1	10.8	0.4	1.8
11.6	3.8	0.0	1.9	9.5	0.8	3.1
3.9	2.2	0.2	0.6	23.0	0.4	0.9
5.5	2.2	0.2	0.8	12.3	0.6	1.4
9.0	3.6	0.0	1.8	11.0	0.7	2.4
6.1	2.3	0.1	1.7	9.6	0.5	1.7
6.9	2.2	0.1	1.3	29.0	0.3	2.4
9.9	3.1	0.1	2.2	23.4	0.5	3.5
5.3	1.6	0.0	1.5	12.6	0.7	1.5
4.8	2.6	0.3	0.7	16.2	0.6	1.2
12.6	4.0	0.0	1.6	5.6	1.1	3.3
11.8	8.1	0.1	2.1	6.7	0.9	3.0
4.0	2.6	0.1	0.7	29.0	0.3	0.9
6.9	3.1	0.0	0.7	0.1	0.2	1.5
6.5	2.1	0.0	0.9	1.7	0.4	1.7
4.0	1.7	0.1	1.4	17.1	0.3	1.2
7.6	4.1	0.1	0.9	17.6	0.2	2.1
13.6	4.7	0.1	1.2	4.2	0.3	3.4

TiO ₂	P ₂ O ₅	Pf	Total	Na/Si	Al/Si	K/Si
0.4	< L.D.	6.0	99.7	0.0373	0.1325	0.0324
0.8	0.2	4.3	99.7	0.0387	0.1317	0.0305
1.1	0.2	4.4	99.7	0.0184	0.0769	0.0160
0.4	0.1	2.8	99.8	0.0165	0.1131	0.0241
0.5	0.1	2.3	99.7	0.0125	0.1225	0.0294
0.6	0.2	8.4	100.0	0.0219	0.2786	0.0677
0.7	0.2	7.2	100.0	0.0154	0.2311	0.0613
0.5	0.2	10.3	102.2	0.0168	0.2334	0.0617
0.3	0.1	2.1	102.0	0.0119	0.0679	0.0245
0.6	0.1	6.0	99.4	0.0281	0.1997	0.0588
0.3	0.1	0.8	99.3	0.0102	0.0849	0.0190
0.7	0.2	6.7	99.9	0.0116	0.1998	0.0497
0.8	0.1	6.3	99.7	0.0143	0.2008	0.0544
0.7	0.1	8.2	100.4	0.0203	0.3448	0.0816
0.4	0.1	2.6	99.5	0.0135	0.1014	0.0271
0.5	0.1	2.8	98.8	0.0144	0.1054	0.0296
0.4	0.1	6.4	99.8	0.0225	0.1113	0.0304
0.5	0.1	6.6	99.7	0.0188	0.0997	0.0266
0.5	0.1	10.5	100.8	0.0377	0.2111	0.0594
0.0	0.0	0.0	0.0	0.0000	0.0000	0.0000
0.5	0.1	4.6	100.5	0.0229	0.0985	0.0255
0.5	0.1	4.3	99.8	0.0261	0.1052	0.0249
0.5	0.1	4.8	98.9	0.0325	0.1238	0.0318
0.5	0.1	10.0	99.7	0.0331	0.2356	0.0698
0.5	0.1	9.9	98.7	0.0321	0.2408	0.0695
0.5	0.1	8.3	99.5	0.0335	0.1937	0.0571
0.4	0.1	7.2	99.1	0.0329	0.1728	0.0490
0.5	0.2	6.0	99.8	0.0419	0.1452	0.0352
0.6	0.2	7.1	100.0	0.0513	0.2377	0.0633
0.4	0.1	8.5	99.8	0.0424	0.1722	0.0444
0.5	0.1	6.1	99.4	0.0386	0.1548	0.0399
0.5	0.1	12.0	100.4	0.0508	0.2701	0.0786
0.5	0.1	11.9	100.2	0.0510	0.2706	0.0774
0.5	0.1	10.3	100.2	0.0501	0.2300	0.0650
0.5	0.1	9.4	99.9	0.0486	0.2151	0.0605
0.5	0.1	8.8	100.3	0.0476	0.2054	0.0576
0.5	0.1	8.2	100.6	0.0450	0.1917	0.0530
0.5	0.2	7.5	99.5	0.0415	0.1545	0.0384
0.5	0.1	11.6	98.7	0.0495	0.2469	0.0664
0.5	0.1	10.1	99.9	0.0470	0.2353	0.0639
0.5	0.1	8.9	99.2	0.0478	0.2173	0.0583
0.5	0.1	9.4	98.6	0.0485	0.2279	0.0615
0.5	0.1	12.9	100.0	0.0444	0.2497	0.0668
0.5	0.1	11.2	98.6	0.0477	0.2317	0.0621
0.3	0.1	6.4	98.9	0.0381	0.1433	0.0363
0.4	0.1	4.5	99.7	0.0452	0.1725	0.0414
0.6	0.1	< L.D.	88.2	0.0483	0.2681	0.0758

0.6	0.2	8.3	99.5	0.0405	0.2178	0.0606
0.6	0.1	4.9	99.3	0.0469	0.2236	0.0659
0.6	0.1	5.3	99.2	0.0481	0.1995	0.0555
0.5	0.2	7.5	99.5	0.0415	0.1545	0.0384
0.6	0.1	5.3	99.2	0.0481	0.1995	0.0555
0.4	0.1	4.5	99.7	0.0452	0.1725	0.0414
0.4	0.1	0.0	0.0	0.0407	0.1537	0.0392
0.4	0.1	0.0	0.0	0.0411	0.1539	0.0394
0.6	0.1	13.4	101.1	0.0443	0.3257	0.0861
0.7	0.1	13.6	101.5	0.0522	0.3329	0.0895
0.7	0.2	8.9	102.4	0.0268	0.3309	0.1007
0.6	0.1	9.0	100.5	0.0489	0.2544	0.0681
0.6	0.1	11.7	101.1	0.0464	0.2853	0.0745
0.6	0.1	9.9	101.2	0.0418	0.2446	0.0650
0.6	0.1	7.8	101.1	0.0464	0.2273	0.0587
0.5	0.1	11.4	100.6	0.0473	0.2493	0.0659
0.6	0.1	13.9	100.8	0.0497	0.2891	0.0744
0.6	0.1	12.3	99.8	0.0456	0.3074	0.0851
0.5	0.1	10.6	100.0	0.0458	0.2338	0.0635
0.5	0.1	13.4	100.1	0.0437	0.2620	0.0698
0.5	0.1	8.4	100.7	0.0465	0.2386	0.0613
0.5	0.1	10.5	100.7	0.0444	0.2177	0.0571
0.5	0.1	6.9	100.7	0.0410	0.2334	0.0605
0.5	0.1	10.7	100.9	0.0447	0.2597	0.0648
0.6	0.1	10.2	100.8	0.0425	0.2811	0.0693
0.5	0.1	11.8	100.9	0.0481	0.2649	0.0704
0.6	0.1	11.6	100.9	0.0476	0.2557	0.0663
0.6	0.1	10.7	100.9	0.0444	0.2493	0.0686
0.5	0.1	10.1	100.5	0.0450	0.2021	0.0539
0.5	0.1	9.9	100.3	0.0468	0.2255	0.0612
0.5	0.1	9.5	100.3	0.0450	0.2141	0.0586
0.6	0.1	9.9	99.5	0.0436	0.2566	0.0663
0.5	0.1	10.4	100.3	0.0424	0.2377	0.0636
0.5	0.1	8.8	100.8	0.0444	0.2372	0.0640
0.6	0.1	8.7	100.2	0.0450	0.2566	0.0660
0.6	0.1	6.7	99.8	0.0426	0.2883	0.0780
0.5	0.1	8.1	100.0	0.0465	0.2552	0.0691
0.5	0.1	9.4	99.4	0.0477	0.2382	0.0640
0.5	0.1	10.1	99.4	0.0439	0.2177	0.0577
0.5	0.1	9.4	99.7	0.0440	0.2117	0.0566
0.6	0.1	< L.D.	89.9	0.0438	0.2464	0.0663
0.6	0.1	8.4	99.5	0.0483	0.2202	0.0583
0.5	0.1	9.1	100.0	0.0429	0.2064	0.0543
0.6	0.1	< L.D.	90.9	0.0431	0.2663	0.0707
0.6	0.1	< L.D.	90.9	0.0431	0.2663	0.0707
0.5	0.1	< L.D.	90.4	0.0443	0.2482	0.0664
0.5	0.1	< L.D.	90.4	0.0443	0.2482	0.0664
0.5	0.1	< L.D.	91.0	0.0431	0.2337	0.0618
0.5	0.1	< L.D.	91.0	0.0431	0.2337	0.0618
0.6	0.1	< L.D.	91.9	0.0435	0.2593	0.0699
0.6	0.1	< L.D.	91.9	0.0435	0.2593	0.0699
0.6	0.2	10.4	99.9	0.0473	0.2927	0.0790

0.5	0.2	8.5	99.7	0.0456	0.2434	0.0647
0.6	0.2	8.5	100.0	0.0451	0.2437	0.0644
0.5	0.1	8.3	100.2	0.0454	0.2327	0.0618
0.5	0.1	10.9	99.5	0.0475	0.2660	0.0714
0.5	0.1	9.6	100.4	0.0454	0.2257	0.0592
0.5	0.1	8.1	99.7	0.0441	0.2079	0.0548
0.5	0.1	7.7	100.7	0.0431	0.1906	0.0496
0.6	0.1	11.0	98.8	0.0441	0.2627	0.0716
0.5	0.2	9.8	99.6	0.0436	0.2417	0.0662
0.5	0.2	9.5	100.1	0.0431	0.2285	0.0618
0.5	0.1	8.2	98.5	0.0442	0.2137	0.0561
0.6	0.2	10.0	100.4	0.0467	0.2572	0.0714
0.5	0.1	9.9	98.7	0.0437	0.2321	0.0629
0.5	0.1	9.5	100.7	0.0438	0.2290	0.0621
0.5	0.2	6.8	100.6	0.0405	0.1414	0.0350
0.4	0.1	5.4	99.5	0.0403	0.1592	0.0414
0.5	0.2	5.4	99.1	0.0345	0.1547	0.0294
0.5	0.1	6.3	100.3	0.0242	0.1132	0.0301
0.4	0.1	8.2	100.0	0.0332	0.1511	0.0429
0.5	0.1	10.1	100.1	0.0354	0.1860	0.0535
0.5	0.1	5.0	99.3	0.0454	0.1700	0.0448
0.4	0.1	4.0	100.5	0.0397	0.1368	0.0338
0.6	0.2	7.0	100.2	0.0434	0.2249	0.0623
0.6	0.2	6.3	100.0	0.0453	0.2171	0.0586
0.7	0.2	4.0	100.6	0.0503	0.2951	0.0787
0.7	0.2	4.2	100.8	0.0505	0.3043	0.0814
0.8	0.2	4.6	100.6	0.0509	0.3308	0.0894
0.7	0.2	4.6	100.4	0.0503	0.3239	0.0880
0.7	0.2	5.8	99.9	0.0537	0.3599	0.1005
0.3	0.1	1.7	100.0	0.0393	0.1360	0.0314
0.7	< L.D.	6.3	100.2	0.0046	0.2286	0.0569
0.3	0.1	16.4	99.2	0.0028	0.0898	0.0267
0.5	< L.D.	3.3	100.0	0.0047	0.1121	0.0287
0.6	< L.D.	7.8	99.8	0.0074	0.2184	0.0576
0.1	0.0	5.6	99.9	0.0005	0.0447	0.0350
0.1	0.0	16.7	99.9	0.0000	0.0445	0.0160
0.5	0.1	7.5	100.9	0.0084	0.1513	0.0422
0.5	0.1	8.5	100.0	0.0133	0.1585	0.0446
0.5	< L.D.	6.3	100.4	0.0102	0.1634	0.0441
0.6	0.1	8.3	100.5	0.0138	0.2249	0.0611
0.6	0.1	6.2	101.0	0.0096	0.1907	0.0523
0.3	0.1	11.6	99.8	0.0006	0.0578	0.0171
0.4	< L.D.	2.5	100.8	0.0020	0.0857	0.0233
0.6	0.1	7.9	100.6	0.0104	0.2105	0.0543
0.6	0.1	6.5	98.9	0.0142	0.1624	0.0451
0.6	< L.D.	5.0	99.3	0.0023	0.1810	0.0418
0.6	< L.D.	4.8	99.3	0.0019	0.1737	0.0376

0.6	0.1	5.9	99.8	0.0016	0.1819	0.0365
0.7	0.1	9.9	100.3	0.0033	0.2452	0.0678
0.6	< L.D.	7.4	98.9	0.0021	0.1556	0.0406
0.3	0.0	1.7	99.3	0.0013	0.0347	0.0083
0.2	0.1	4.2	100.0	0.0020	0.0353	0.0100
0.3	0.0	0.7	99.8	0.0021	0.0314	0.0088
0.3	0.2	14.4	99.8	0.0123	0.1241	0.0314
0.5	0.1	5.7	99.8	0.0336	0.1631	0.0444
0.7	0.0	5.4	100.0	0.0181	0.2301	0.0493
0.3	0.1	1.9	99.8	0.0086	0.0531	0.0149
0.7	0.1	7.3	99.7	0.0278	0.2912	0.0825
0.3	0.1	16.6	99.8	0.0102	0.1235	0.0318
0.4	0.1	6.1	99.1	0.0220	0.1324	0.0357
0.3	0.1	11.2	99.8	0.0134	0.1176	0.0354
0.6	0.1	11.2	99.8	0.0272	0.2423	0.0711
0.4	0.1	18.4	99.8	0.02	0.09	0.02
0.3	0.1	10.9	99.8	0.02	0.10	0.03
0.5	0.1	11.7	99.8	0.02	0.18	0.05
0.3	0.1	10.7	99.8	0.01	0.11	0.03
0.3	0.1	24.1	99.8	0.02	0.25	0.09
0.5	0.1	21.9	99.7	0.03	0.34	0.13
0.2	0.1	11.6	100.0	0.02	0.10	0.03
0.3	0.1	13.7	99.8	0.02	0.10	0.03
0.6	0.1	7.8	99.8	0.03	0.24	0.07
0.6	0.2	10.4	99.8	0.03	0.25	0.07
0.2	0.1	25.7	99.9	0.02	0.13	0.03
0.5	0.0	2.2	99.2	0.01	0.10	0.02
0.3	0.0	3.1	99.2	0.01	0.09	0.03
0.4	0.1	15.0	99.8	0.009717034	0.08106069	0.026684672
0.4	0.1	17.7	100.0	0.006373126	0.183039931	0.054005817
0.7	0.1	7.8	99.7	0.009250586	0.254342748	0.069611806

		Lupker et al. (2012)
0.795917	-17.2	This study
		This study
0.73178	-15.7	Lupker et al. (2012)/Huygue et al. (2001)
0.75197	-17.9	Lupker et al. (2012)/Huygue et al. (2001)
0.75181	-17.8	Lupker et al. (2012)/Huygue et al. (2001)
		Lupker et al. (2012)
	-15.5	Robinson et al. (2001)
0.726907	-17.2	Lupker et al. (2012)
		Lupker et al. (2012)
		Lupker et al. (2012)
0.77013	-19.2	Lupker et al. (2012)/Huygue et al. (2001)
		Lupker et al. (2012)
0.755601	-17.5	Lupker et al. (2012)
		Lupker et al. (2012)
		Lupker et al. (2012)
	-16.4	Robinson et al. (2001)
		Lupker et al. (2012)
0.72981	-16.4	Lupker et al. (2012)/Huygue et al. (2001)
0.73254	-16.4	Lupker et al. (2012)/Huygue et al. (2001)
		Lupker et al. (2012)
0.762851	-15.9	Lupker et al. (2012)
		Lupker et al. (2012)
	-17.7	Robinson et al. (2001)
		Lupker et al. (2012)
0.747974	-16.2	Lupker et al. (2012)/Huygue et al. (2001)
		Lupker et al. (2012)
		Lupker et al. (2012)
		Lupker et al. (2012)
	-15.5	Robinson et al. (2001)
0.73887	-14.7	Lupker et al. (2012)/Huygue et al. (2001)
	-16.4	Robinson et al. (2001)
